Real-Time Surface Shape Sensing For Monitoring Flexible Structures Using Fiber Bragg Grating

By

Lun Tian Le Tim

B.Eng. (ME) H.K.U.

A thesis submitted in fulfilment of the requirements for

the Degree of Master of Philosophy

at The University of Hong Kong.

December 2018

Abstract of thesis entitled

"Real-time surface shape sensing for monitoring flexible structures using fiber Bragg grating"

Submitted by

Lun Tian Le Tim

for the degree of Master of Philosophy in Mechanical Engineering at The University of Hong Kong in December 2018

An optical shape sensing system determines the position and orientation of an optical fiber along its entire length. An optical fiber is minimally intrusive, light-weight and can be used to monitor the dynamic 3D shape of a structure to which it conforms. Due to its unique advantages over conventional electric sensors, for example, its immunity to electromagnetic inference, fiber optic sensing has raised great research interest to the community. Some researchers demonstrated the ability of temperature and humidity sensing, 1D bending curvature tracking, and vibration sensing, etc. However, currently there are no fiber optic sensors developed for shape sensing on a 3D deformed surface with the consideration of in-plane stretching, which is especially useful for measuring the morphological changes in the field of soft robotics.

In this research, fiber Bragg gratings (FBGs) are embedded off-center in a soft and flexible sheet for sensing shape changes in 3D deformed surfaces. With FBGs offset from the neutral plane of the silicone film, both extensions and bending curvatures can be captured by the changes in strain (the shifts in wavelength) of bent fiber. With a proper fiber routing design, surface shapes in 3D could be reconstructed.

Finite Element Analysis (FEA) is implemented to predict sensor performances by a series of parametric studies. Strain vectors are extracted at selected deformation mode shapes. Strain patterns are visualized with clustered strain vector groups. Leveraging the sensitivity, the capability of discriminating deformation patterns and the ease of fabrication, a circular fiber configuration (Ø35 mm) is selected. The effect of fiber offset distance h, sensor thickness t, and fiber rigidity E are briefly discussed based on the selected fiber configuration. Taking in-plane stretching into consideration, the final design of the sensor (45mm $\times$ 45mm $\times$ 5mm) is in a dual-layer and circular fiber configuration. The sensor is modeled by an artificial neural network (ANN). By evaluating the trained network, uniqueness of strain-wavelength relation is validated. High regression index R = 0.99 is obtained with a root mean square error of 0.9234 mm and a maximum error of 4.81 mm. Accuracy could be improved by denser gratings. By repeating the sensor unit or changing the fiber configuration, the sensor can be customized for different applications. A brief discussion on fiber routing configurations is given to improve overall sensor stretchability.

The goal of this research to develop a standard workflow of soft sensor design and a real-time surface shape sensor for soft robotics applications. Future studies include optimization of grating parameters and fiber routing.

Word counts: 414

Declaration

I declare that this thesis represents my own work, except where due acknowledgement is made, and that it has not been previously included in a thesis, dissertation or report submitted to this University or to any other institution for a degree, diploma or other qualifications.

Signed . . . .

Acknowledgement

Firstly, I would like to express my sincere gratitude to my advisor Prof. Ka-Wai Kwok for the continuous support of my MPhil study and related research, for his patience, motivation, and immense knowledge. His guidance helped me in all the time of research and writing of this thesis. I could not have imagined having a better advisor and mentor for my MPhil study.

Besides my advisor, I would like to thank the experts who were involved in this work: Prof. K.Y. Sze, Prof. James Lam, and Prof. Kenneth Wong, for their insightful comments and encouragement, but also for the hard question which incented me to widen my research from various perspectives.

I would like to thank my fellow labmates in for the stimulating discussions, for the sleepless nights we were working together before deadlines, and for all the fun we have had in the last years. In particular, I am grateful to Ziyan, Chimlee, Justin and Marco, who have been unwavering in their personal and professional support during the time I spent at the University. Also I would like to thank all my friends in the journey of my study.

Last but not the least, I would like to thank my family and my love for supporting me spiritually throughout writing this thesis and my life in general.

Thanks for all your encouragement!

Tim Lun

Table of Contents

List of Figures

Figure 4.3.1 Simulated fiber strains under different deformations. The first column shows the deformed shape sensor under different loading combinations. The second column shows the colormap of the deformed fiber in elastic strain component E11. Warmer color indicates a higher strain induced on the fiber. The third column shows the simulated fiber strain patterns which are

List of Tables

Abbreviations and Symbols

ANN	Artificial Neural Network
CTPE	Conductive Thermoplastic Elastomer
DTG	Draw Tower Gratings
EM	Electromagnetic
FBG	Fiber Bragg Grating
FE	Finite Element
FEA	Finite Element Analysis
FMA	Flexible Microactuator
FWHM	Full Width at Half Maximum
IR	Infrared Radiation
MEMS	Microelectromechanical Systems
NURBS	Non-Uniform Rational Basis Spline
OFDR	Optical Frequency Domain Reflectometry
PDMS	Polydimethylsiloxane
PLED	Polymer-OLEDs
RMSE	Root Mean Square Error
SM	Single Mode
SMA	Shape-Memory Alloy
SNR	Signal-to-Noise Ratio
UV	Ultraviolet
WDM	Wavelength-Division Multiplexing
Φ	Circular Pattern Angle
λ_B	Reflected Wavelength / Bragg Wavelength
n_e	Effective Refractive
Λ	Grating Period

ε_m	Mechanical-Induced Strain Component
ε_T	Temperature-Induced Strain
α_{sp}	Expansion Coefficient per K of the Specimen
α_δ	Change of Refraction Index
ΔT	Change in Temperature in K

1. Introduction

1.1. Motivation and Objectives

In recent years, soft robotics is under rapid developments due to the excellent flexibility and conformability that traditional robots do not provide. This has started a trend in soft robot designs and researchers focused on implementation issues. This kind of robotic structure is soft and deformable thus allowing safer interaction with an unstructured environment with ease. Soft robots are usually fabricated from elastic materials such as elastomers, generating motions from the deformation of the soft bodies. For example, soft tentacle actuators and soft grippers have demonstrated reliable gripping capability towards objects with a large variation in shape.

However, due to the intrinsic properties of soft robots, i.e. deformable bodies and generally infinite degrees of freedom, the deformation patterns and configurations are difficult to capture thus feedbacks are rarely available for control. Many soft robots operated only with open loop controls, limiting the applications in well-structured environments. Embedment of traditional sensors into soft robotic systems are available but usually, the stiffness does not match with the soft bodies thus constraining the bodies' motions. Other limitations of existing sensors including sensor durability, EM-immunity, accuracy, complex motions sensing, etc.

Studies on the sensor morphology design and sensor placement are also necessary for sensing deformation patterns. Once deformation data is available, interaction forces on the soft bodies can also be estimated as control feedbacks.

The purpose of this thesis is to address the sensing challenges in soft robotics which could enable the control of soft robotic systems. The main contributions of this work include:

1. A design framework for sensors with surface morphology sensing capability. An optical-based surface shape sensor is built according to the proposed framework;
2. Finite Element Analysis (FEA) to determine the design parameters of the sensor with fiber Bragg gratings embedded. The mapping between reconstructed displacements and Bragg wavelengths is proven to be unique with the proposed fiber routing;

3. Robust and reliable surface reconstruction, which has been demonstrated such that the surface shape sensing can be achieved without prior knowledge of FBGs' locations by machine learning approach.

1.2. Publications During the Study Period

The following listed the publications in international journals and conference proceedings during the study period:

1) <u>Lun, T. L. T</u>., Wang K., Ho, J. D. L., Tse, K. Y., Kwok, K. W. (2018). *Real-time surface shape sensing for soft and flexible structures using fiber Bragg grating*. **IEEE RA-L and ICRA 2019 Special Issue on Soft Haptic Interaction: Modeling, Design, and Application**. (**Reviewed and resubmitted**)

2) Tang, S. C., <u>Lun, T. L. T.</u>, Guo, Z., Kwok, K. W., & McDannold, N. J. (2017). *Intermediate range wireless power transfer with segmented coil transmitters for implantable heart pumps*. **IEEE Transactions on Power Electronics, 32(5), 3844-3857**. First Prize Paper Award out of 789 papers accepted in 2017.

3) Tang, S. C., <u>Lun, T. L. T.</u>, Guo, Z., Kwok, K. W., & McDannold, N. J. (2016, May). *Mid-range wireless power transfer with segmented coil transmitters for implantable heart pumps*. In Electromagnetics: Applications and Student Innovation Competition (iWEM), **2016 IEEE International Workshop on (pp. 1-3). IEEE**.

4) Guo, Z., <u>Lun, T. L. T.</u>, Chen, Y., Su, H., Chan, D. T. M., & Kwok, K. W. (2016). *Novel design of an MR-safe pneumatic stepper motor for MRI-guided robotic interventions*. **In Proceedings of The Hamlyn Symposium on Medical Robotics**.

2. Emerging Technologies for Soft Robotic Sensing

2.1. Introduction

The use of soft and deformable structures in robotic systems is expanding over the years. Since their discovery in the 80s [1] and early 90s [2], manipulators and actuators with high flexibility and conformability are developed for fragile items handling, body inspection, and microsurgery. Recently, researchers designed and modeled deformable structures to perform tasks in unstructured and dynamic environments, including locomotion in rough terrains, grasping and manipulation of unknown objects, and interaction with human bodies and cells. The investigation on soft robotics is now divided into three major areas:

1. Soft materials and fabrication
2. Modeling and simulation techniques
3. Sensing, actuation, and control

A number of researchers focused on soft robot design [3-5] and soft material properties [6, 7]. Recent designs on these soft and flexible structures have been widely applied in the areas of rehabilitation, rescue robots and even endoscopic devices. Thanks to the advancement in fabrication techniques, for example, multi-material embedded 3D printing [8], micro-molding [9] and soft lithography [10], fabricating new soft robots are becoming more and more convenient and promising. However, few studies addressed on how to achieve sensing and control in soft-bodied robots.

In this chapter, a comprehensive overview of recent soft robot development will be presented. The review also outlines the current challenges in soft robot developments. Flexible sensors, shape sensors and corresponding shape sensing methods related to soft robot sensing are also reviewed. It also includes the capabilities and advantages of fiber optics as a potential sensing element in a soft and flexible sensor. Furthermore, it presents several techniques in surface reconstruction and discusses how they can be applied in soft robotic sensing systems.

2.2.   Trends, Development of Soft Robotics and the State of the Art

Traditional rigid robots usually consist of rigid links and hard components that are difficult to change their physical appearances. They are designed to perform fast and precise tasks and to be stiff [11] in order to reduce the effect of external inferences. External inferences, e.g. vibrations, generally induce a loss in accuracy. However, as there are rigid hard links and joints, the interaction between rigid robots and human beings becomes unsafe. Thus, traditional robots are usually separated from human workspace to perform well-structured and programmed tasks. When rigid robots are slowly blending into human society, they are not able to adapt to the environment due to their intrinsic properties. In contrast to hard robots, soft robots which are made from intrinsically soft and flexible materials that provide compliance when interacting with external environments. The high adaptability and flexibility induced the rise of soft robotics [12].

Tracing back to the '90s [2], researchers started working on soft and flexible grippers and manipulators for soft interactions. Contrary to machine-like manipulators with low mechanical adaptability and high precision, soft manipulators can deform to a spectrum of morphologies and adapt to the shape of targets, relaxing precision and control requirements in tasks such as grasping and handling unknown objects.

A flexible microactuator (FMA) was developed in 1991 [2]. It was actuated by an electro-pneumatic or hydraulic system and has three degrees of freedom. Motions including pitch, yaw, and stretch are performed to mimic fingers, arms or legs. The structure of this microactuator is shown in **Figure 2.2.1**. Using fibers as a reinforcement layer, the rubber chamber, which has no conventional rigid links, expanded and deformed to the designed curvature. The FMAs can be linked up in serial to form a miniature robot manipulator. When linking up in parallel, multiple FMA fingers formed a robot hand. Bending moment equilibrium and non-slip holding condition are considered. Various holding modes are shown. The capability of FMAs is demonstrated with example applications such as bolt tightening.
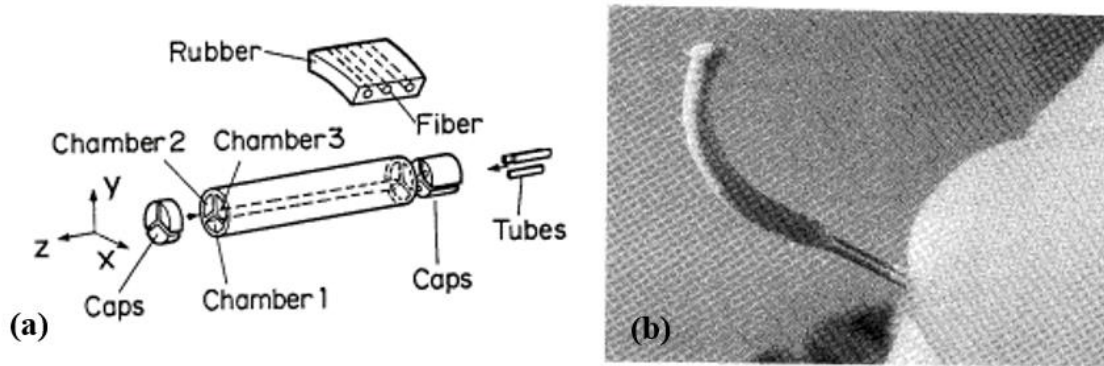
Figure 2.2.1 (a) FMA structure: rubber chambers, connection caps, tubes and the reinforcement layer integrated to form a FMA unit. **(b)** Φ 1mm FMA was held by fingers and bent due to chamber pressurization [2].

A typical example of soft robots in medical application is STIFF-FLOP. STIFF-FLOP project started in 2012 and ended in 2015 [13]. This soft robotic manipulator is designed to replace conventional rigid robot tools in complex surgical tasks. Unlike modern laparoscopic and robot-assisted surgical systems, the dexterity of STIFF-FLOP facilitates the access to Trocar ports, which is originally restricted by conventional systems. By controlling the stiffness of STIFF-FLOP at different locations of the body, it can manipulate objects in a confined space filled with organs [14], while safety is ensured during the interaction, as shown in **Figure 2.2.2**. The development of this soft robotic arm demonstrated the potential impacts to the society by utilizing the advantages of soft robots.
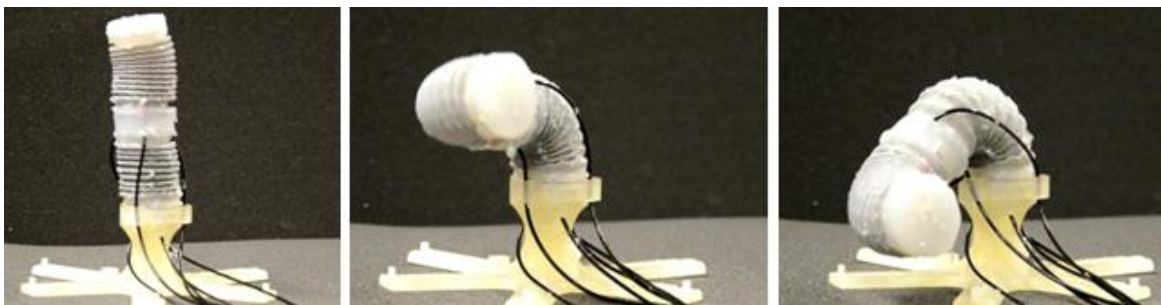
Figure 2.2.2 Bending motions of STIFF-FLOP (from Left to Right). Bending segments can be controlled by pressurizing the inner chambers. Its body can be stiffened by jamming granules in the chambers [13].

While STIFF-FLOP presented the possibilities in applying soft robotics to laparoscopy procedures, a microscale soft gripper is developed to handle delicate microscale objects in 2015 [15]. It is built from microscale pneumatic actuators which is easy to fabricate. A novel direct peeling-based technique is applied to build microtubes using flexible and highly deformable elastomers. The microtubes are then integrated to form a microscale robotic tentacle based on a user-defined shape. The final actuator is then programmed to perform multi-turn inward spiraling instead of pure bending since this restricted grabbing radius due to soft body collisions. The inward spiraling motion of this soft microgripper allowed a small grabbing radius as 185 μm and achieved a grabbing force of 0.78mN with high efficiency. Delicate handling of soft and fragile objects such as ants and fish eggs are shown in **Figure 2.2.3**. This demonstrated its reliability in micro-objects manipulation.
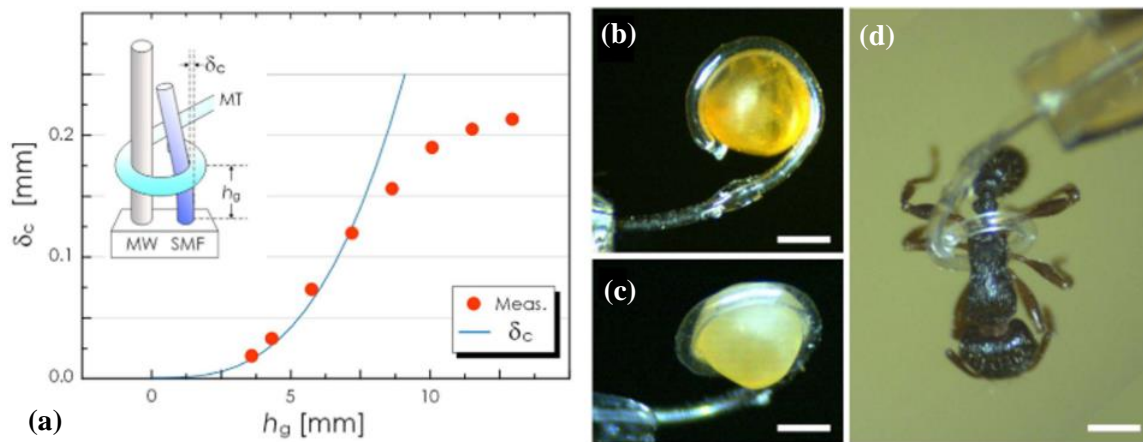
Figure 2.2.3 (a) PDMS micro-tentacle grabbing a cantilever. Deflections are measured by applying a theoretical point-loaded force at 0.78mN. **(b-d)** Different objects are grabbed and captured under an optical microscope [15].

Other than the tentacle-like microgripper reviewed above, many existing soft robots are bio-inspired and their structures are referenced from octopus [16, 17], elephant [18], fish [19] and even worms [20, 21], as shown in **Figure 2.2.4**. By replicating body structures of animals, researchers can find out better locomotion methods and manipulation schemes inspired by nature, further to provide insight into the development of new kind of actuators and medical devices.
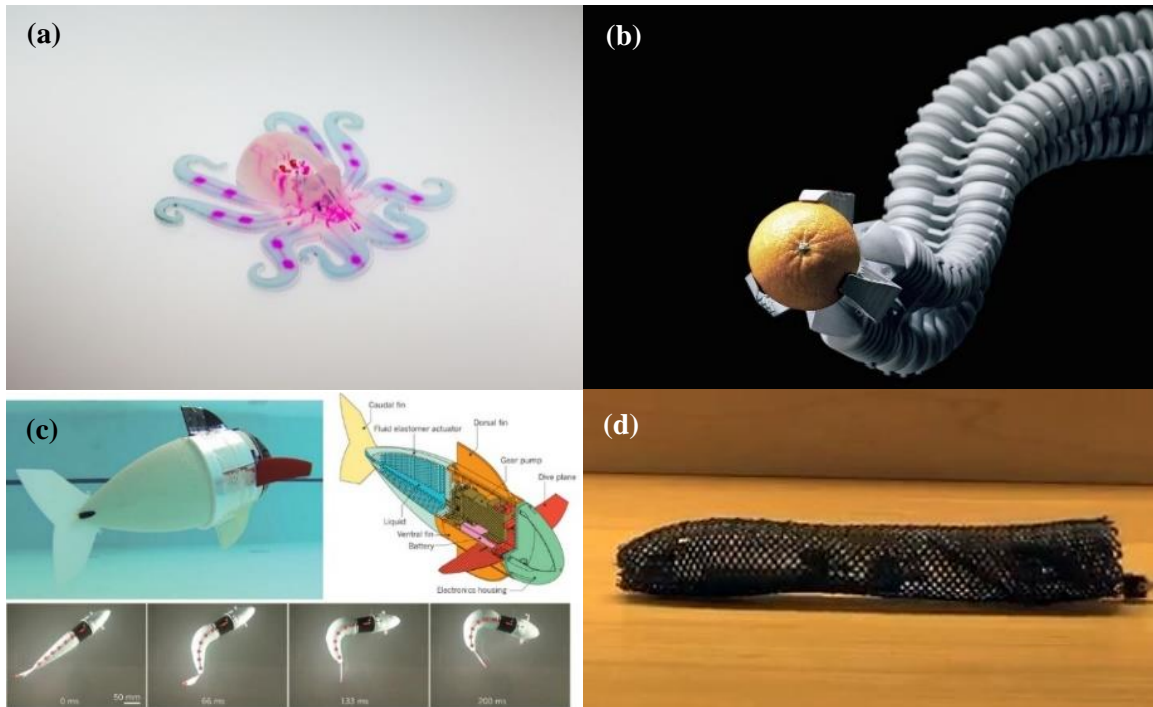
Figure 2.2.4 **(a)** First self-contained, completely soft octopus robot [17]. **(b)** Festo's bionic handling assistant [18]. **(c)** Soft robotic fish [19]. **(d)** Soft earthworm robot [21].

Besides mincing the nature, researchers attempted to build up soft robots and to optimize robot design for specific tasks with new approaches such as evolutionary methods [22]. This approach used encoding as an essential element, generating solutions to the specific problem domain. Tasks like robot gait and morphology evolution have been accomplished with satisfactory results from the evolved controllers. In **Figure 2.2.5**, generative encoding genotype representation was applied as an evolutionary method to generate new types and structures of soft robots. Three soft body virtual creatures evolved and generated efficient locomotion strategies in simulations. In traditional evolutionary methods, diversity of soft robot designs is limited due to the constraints predefined by users which aimed to optimize the objective function and converged towards local optima. In contrast, novelty search rewarded diversity instead of optimizing individuals. It mimicked the natural evolutionary processes thus gave rise to the design diversity and infinite solutions by investigating multiple environmental variables.

7
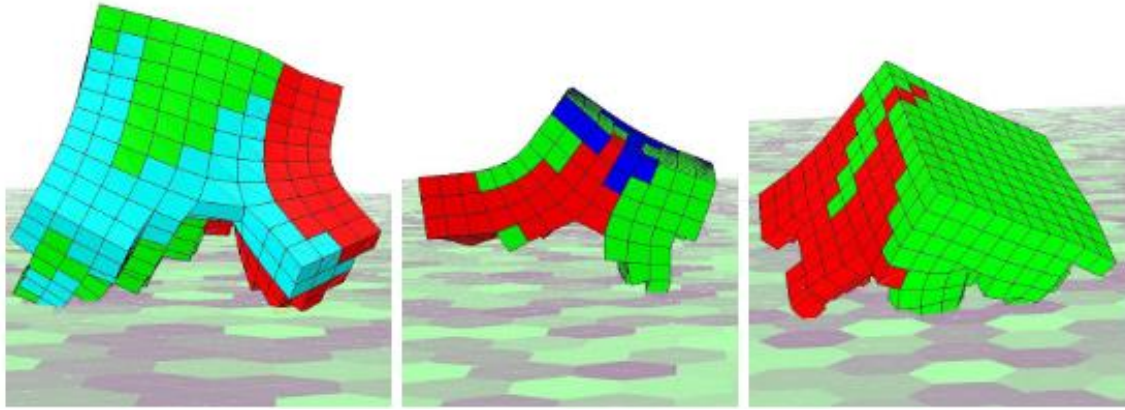
Figure 2.2.5 Evolution of three soft robots in different combinations of elements by novelty search. Mimicking natural evolution, this approach valued diversity instead of optimizing objectives. The soft robots are generated based on these elements: muscles (Red and green), tissues (Cyan) and bones (Blue) [22].

Other than bioinspired and evolutionary methods in the field of natural computation, researchers are investigating the potential of morphology computation techniques [23, 24] to design new soft robot bodies. The goal in soft robotics design is to provide high adaptability and simple control architectures, and to increase overall performance by fusing motion control into the physical system behavior. Yet, these studies have not concluded a complete design framework to generate desired robot behavior. Moreover, sensing systems are still missing for deformation measurement.

2.2.1. *Technical Challenges in Soft Robotics*

Traditional rigid-linked robots are not capable to perform motions such as squeezing, stretching and morphing [25]. The use of soft materials and soft motions performed by soft robots allows effective interactions with natural and unstructured environments.

However, soft robots are highly diverged from traditional robots in terms of materials, modeling, and control. Made of compliant materials like silicones, they are usually fabricated by molding and extruding, instead of conventional machining procedures like sculpting, grounding or forging [26]. One common fabrication approach is to design a soft body with pneumatic channels, which the

香港大學
圖書館
HKU
Libraries

channels are referenced from pneu-nets (PNs) structure. This structure consists of a series of chambers embedded in a layer of extensible elastomer and an inexpensive layer. By pressurizing the chambers with fluids, the structure deforms and actuates like inflating a balloon. Because of its simplicity in robot architecture [27], a large portion of newly developed soft robots made use of this kind of structure. Since this kind of fabrication method involves procedures that are not as accurate as machining, the quality is somehow a concern of reliability. For example, the elastic modulus of a soft, molded part could have a variation up to ± 15% which cannot be fine-tuned by manufacturing processes. Moreover, current molding and extruding techniques limited the design parameters and possibilities of soft robots. Complex structures cannot be fabricated by conventional methods. Thus, many soft robots can only perform simple motions such as bending, twisting or elongating. Fortunately, recent advances in fabrication techniques relaxed the constraint in soft robots' structural design. Techniques including micro-molding [9], soft lithography [10], multi-material embedded 3D printing [28] provided opportunity for soft robots to evolve, enabling further development of new types of soft robots with shape changing, morphing and other abilities [25].

The use of unusual materials also raised the problem in soft robotic control. With an inherent and complaint soft body and theoretically infinite degrees of freedom, modeling and control of the soft body becomes very challenging. Many studies focused on the modeling and control of continuum robots [29-31]. These continuum robots are usually tubular or catheter-like [32] which are actuated by tendons, smart memory alloys (SMA) and EAPs. Instead of deforming the material of thin robot bodies, this kind of robotic manipulator applies unbalance forces on circumference like muscles to create curvatures of the robot body. Control approaches of this particular kind of soft robots included configuration tracking [29], hyper-redundant manipulator kinematics modeling [33], geometrically exact Cosserat approach [34], however, these methods are limited to tubular continuum manipulators only. Learning-based modeling methods [30, 35] are suggested recently for other soft bodies with complex nonlinear behavior. In addition, real-time finite element model simulation [36] is another solution to soft robotic control.

One of the important components in soft robots is the sensory element as to provide feedback to the control system. It is unreasonable to have a soft robotic system performing tasks like search and rescuing, without any controllable actions and feedbacks, at the same time interacting with external environments. Due to the flexible and stretchable nature of soft robots, sensing systems in soft robots required unconventional approaches for deformation detection, in which conventional

9

position and force sensors are rigid or semi-rigid electronics that are not designed to work with intensive shape changes [37]. It is expected that an ideal soft robotic sensor system to be flexible and stretchable. A number of soft sensors are developed in recent years to detect stretching [28], contact force [38-40], displacement and force output [41], bending and twisting [42], object shape at contact tip [39], yet neither one of them can sense their own deformed morphology nor compact enough to embedded onto a soft robotic system.

2.3. Surface Shape Sensing for Robot Manipulation

Sensing is one of the current challenges in soft robotics [43, 44]. Controllability of soft robotic systems can be highly improved by the assistance of the soft sensors. Also, external information, such as environmental conditions, could be retrieved for data analysis that could be further used in path planning and 3D space reconstruction. Sensing of soft robots focuses on the deformation data for getting measurements like tactile and posture information. For example, tactile signals can be measured from small deformation data and robot postures can be estimated from massive, global deformation data. Another form of feedbacks, including external forces, can be predicted from deformations if accurate system parameters are given. However, soft robots are generally with infinite degrees of freedom (DoFs) which are not accurately controllable as traditional rigid-link robots do. This indicates that conventional approaches which assign one sensor to one DoF are not applicable and impractical in soft robotic systems unless the system is specially designed to reduce and limit its DoF. Thus, new methods must be developed for deformation sensing on soft robotics.

Other difficulties in designing new soft sensors are sensor flexibility and stretchability. An ideal soft sensor is flexible and embeddable on the soft robotic system with minimal effect on the robot motions and structural stiffness. Existing soft sensors integrated into flexible manipulators, wearable, and stretchable electronics are reviewed below. Strain and deformation sensing methods and their limitations are also addressed.

2.3.1. *Flexible and Stretchable Sensor*

Flexible manipulators, *in vitro* diagnostics, advanced therapies and future displays are seeking new sensors with higher flexibility and lower interferences to the original systems [45]. Since 2004, numerous flexible and stretchable sensors are developed for wearable electronics [46].

Researchers at the University of Tokyo are pushing boundaries in the field of flexible electronics by the invention of the latest bionic skins. In the past, artificial skins are unpopular due to their rigidity and excessive cost. Someya *et al.* developed new ultrathin sensors which are just one micrometer thick, stretchable up to 250% and still functional after crumpling [47]. The bionic skin composes of multiple sensor grids. The grids are first printed onto plastic films by ink-jet printing and later layered onto a pre-strained rubber substrate. The fabrication procedures are shown in **Figure 2.3.1**. It is then attached to a robotic arm for pressure sensing. Recently, this technique is further applied to implantable medical devices to measure heart electrical flow and brain pressure and even oxygen levels in the blood with PLED displays [48].
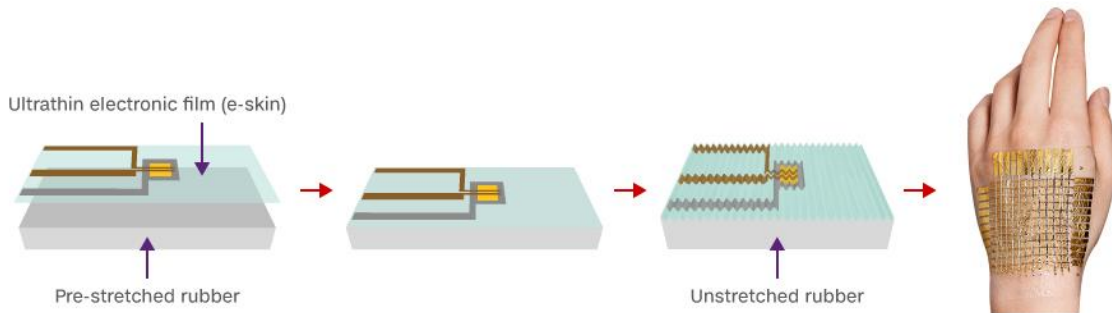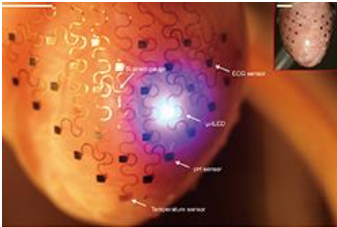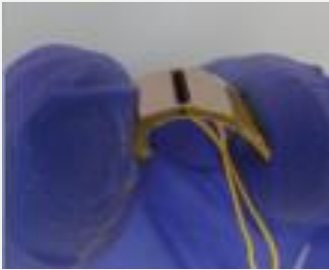
Figure 2.3.1 Ultrathin plastic film with electronic circuits attached and accurately positioned on a pre-strained rubber substrate. After fabrication, a network of out-of-plane wrinkles is formed to accommodate relaxed pre-strains [47]. The soft film can be attached to human skin without uncomfortable feelings.

Other types of flexible sensors are summarized in **Table 2.3.1**. Applications of these flexible sensors including rehabilitation [49], bio-signals measurement [50] and motion capture devices [51].

Table 2.3.1 Classification and description of mechanical and electrical flexible sensors [49]. The flexible sensors are summarized into 4 categories. The corresponding features and common sensor substrate materials are listed.

Category	Features	Sensor substrate
Electronic skins [51]	Flexible pressure sensors	PEN[1], rubber, PET[2], PDMS[3],PI[4], rubber, Parylen
Wearable devices [42]	Flexible strain-gauge sensor Motion detector Skin adhesive patch	PET, PDMS, PUA
Implantable devices [52]	Brain signals mapping Cardiac electrophysiology mapping	PI mesh, silk
Advanced sensors [53]	Transparent pressure sensor Self-powered sensor Self-healing sensor	PDMS, Ecoflex, Empol 1016, DETA[5], PET

[1]PEN – Polyethylene naphthalate

[2]PET – Polyethylene terephthalate

[3]PDMS – Polydimethylsiloxane

[4]PI – Polyimide

[5]DETA – Diethylenetriamine

Although these examples demonstrated the possibilities of flexible sensors in real life applications, many of them degrade rapidly and unable to fully integrate into soft actuators. Only a few of them implemented on physical systems with a considerable amount of success [54]. It is generally recognized that the ability to perform a significant degree of deformations while allowing accurate and precise measurements on locally deformed areas is one of the challenges to develop new soft sensors. However, some researcher purely focused on the sensor's materials and fabrication techniques without considering integration methods in real life physical systems. In [55], the implementation issues are summarized below:

- The connection or sensing materials (e.g. electrodes or wires) should not restrict the behavior (mechanic properties) of the soft system
- The sensor should be easy to fabricate and integrate into soft systems

Combining the factor of sensor sensitivity, these measures will be used to evaluate the performance of the soft sensor in coming chapters.

2.3.2.   *Soft Sensing Principles*

Robot performances can be improved with soft robotic sensors only if proper sensors are used. In soft robotics, one focused on deformation measurement i.e. either strain or deformation sensing [55]. Strain datum is being interested since it reflects the state of a mechanical structure directly at a local position. Different principles for strain measurement and their strength and weakness are reviewed below.

Resistive ionic sensors are highly flexible strain sensors. They are usually fabricated with flexible polymers like PDMS utilizing micro 3D printing techniques. Molds with microchannels are 3D-printed and conductive liquids are injected into the microchannels. When strain is applied to the sensor, the resistance in embedded ionic liquid metals changes. By measuring the variation in resistance, corresponding strain can be computed using experimental constitutive relations. In [56], a hybrid soft elastomer strain sensor is developed to measure strains up to 100%. Two conductive liquids with different resistivity, i.e. saline solution and eGaIn, are used to decouple signal and

sensing routing shown in **Figure 2.3.2**. This sensor configuration eliminated uninterested strain signals on the signal wires. Park *et al.* presented another highly stretchable sensor with three microchannel layers to identify the direction of the strains and able to measure strains up to 250% [57]. This sensor allows multiple modal sensing with a high degree of accuracy, including *x*-, *y*-axis strain measurement and *z*-axis strain measurement at the center of the sensor without additional sensors. However, high hysteresis is observed in *z*-axis strain sensing and improvement on repeatability is required. Also, the sensor morphology and microchannel structures must be carefully designed to measure desired deformations or modal shape.
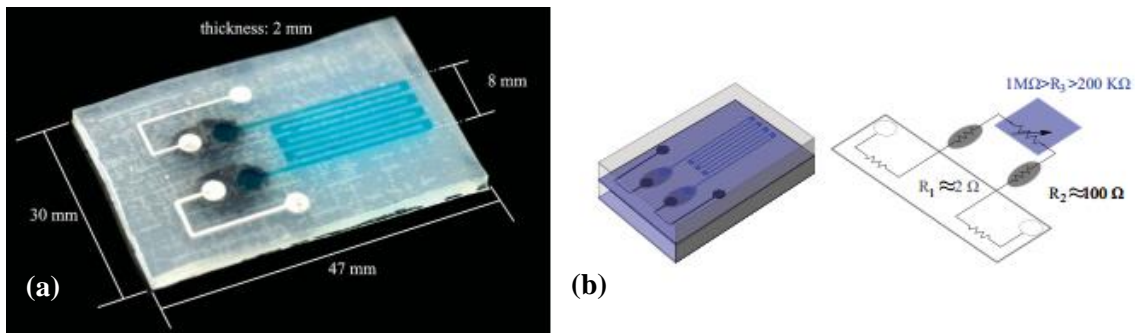
Figure 2.3.2 (a) Hybrid soft strain sensor prototype and **(b)** schematic diagram of the electrical circuit where R1, R2, and R3 are the eGaIn resistance, the silicon-doped interfaces resistance, the ionic solution resistance respectively [56].

A similar technique is applied to develop soft multi-axis force sensors [58], however, unique strain and pressure information cannot be identified in all these sensors. The difficulties in electrode attachment on the sensor also limit the development of resistive ionic sensors.

Flexible electronics are commonly used for pressure sensing instead of strain sensing due to extremely limited strain allowable. PDMS is usually used as a substrate in fabricating highly flexible organic films [59-61]. These polymer film transistors are sensitive to pressure which were proven advantageous in terms of high stability and sensitivity with low power consumption [62]. Carbon nanotubes [63, 64] are another type of elastic and transparent conductors for building flexible sensors. Lines of carbon nanotubes are prepared and formed into arrays of capacitive

sensors. However, nanotube films buckles at 40% strain thus limited the use of this sensor for real-life application such as robotics systems. In fact, most of the applications in flexible electronics are restricted to pressure sensing like health monitoring and diagnostic medicines.

Piezoelectric, piezoresistive, and piezocapacitive Strain Sensors were developed respectively from the principle of piezoelectric, piezoresistive, and piezocapacitive effects. Mechanical stresses applied will generate electric charges and changes in electrical resistance and capacitance. Recent piezoelectric fine wires developed [65, 66] and demonstrated extraordinarily high strain sensitivity and fast response time in both static and dynamic mechanical loading situation. It has been shown that fiber-based strain sensors can be embedded to textiles such as fabric but mostly focused on Micro-Electro-Mechanical Systems (MEMS) [67] since the range of strains sensible is small. Gullapalli *et al.* increased the allowable strain ranges by embedding crystalline piezoelectric material into ZnO-paper but still applicable to microscale measurement only [68].

Capacitive strain sensors based on capacitive sensing techniques. Sensor capacitors are typically configured in a push-pull state and the capacitors are supported with electrical isolators. [69] fabricated flexible capacitive strain gauges on a foil for wireless strain measurement in both static and dynamic environment. It is composed of four layers with polyimide and liquid crystal polymer substrates. The capacity-based sensing architecture enabled a lower power consumption when comparing to resistance-based sensors that have a low impedance in general. Experimental results indicated a high reliability of this sensor with accurate strain measurement without hysteresis. The capacitance sensor can be strained up to 700%, however, maximum strain measurable is 200% when sensor length = 100 mm. The measurable strain would further be reduced for longer sensor length. As the change in capacitance is captured by the decay time, both sensor refresh rate and measurable strain reduce when sensor length increases. This intrinsic behavior of capacitance type sensors largely constrained their potential applications. [70] built a highly stretchable and transparent capacitive strain sensor from carbon nanotubes. It is developed for human motion capturing and demonstrated excellent durability with high strain measurement up to 300%. A strain gauge is embedded into a glove to detect finger bending without constraining the motion of hands like fiber- and foil-based strain gauges.

In contrast to capacitive strain sensors like carbon nanotubes, conductive particles (e.g. carbon black) are used to incorporate into thermoplastics or elastomers for higher repeatability and

sensitivity. [71, 72] fabricated conductive sensing textiles with a mixture of carbon black with thermoplastics elastomer and further attached it on a silicone thin film. Maximum strain is recorded at 80% with small hysteresis and no aging is observed on the sensor material. It is then implemented into a catsuit for body posture recognition with a total mean error of 5.5%. The investigation of carbon-elastomer composites is continued by [73] and the piezoresistivity on different material combinations are studied. Luheng *et al*. developed a mathematical model for carbon-black-filled silicone rubber composite's piezoresistivity and identified the key factors of the piezoresistivity, i.e. the electrical resistance of single effective conductive paths and the number of effective paths available. This result allows researchers to develop sensors of desire piezoresistivity by controlling carbon black content in a conductive mixture.

Optical sensing utilizes camera or fiber to detect deformations and contacts. Winstone *et al*. developed a versatile tactile sensor, TACTIP, using an embedded camera on a soft artificial fingertip for contact, pressure, and shear force sensing [74]. The camera is located inside the fingertip and covered by a soft skin as shown in **Figure 2.3.3**. It is used to detect internal deformations of the TACTIP skin. When the fingertip contacts with other objects, the skin deforms and vibrates. Displacement shifts on the nodes at the inner side of the skin are being captured. The motion of the fingertip and the displacements are then analyzed to identify textured profiles along the moving path of the fingertip. This fingertip sensor presented an accurate and sensitive measurement of contact surface texture when the deformation is small. It also demonstrated the ease of implementation of existing soft and flexible manipulators' fingers. However, it is unsuitable for measuring large-scale deformations and a camera must be placed close enough to the position where deformation occurs. Kang *et al*. fabricated highly stretchable photodetectors and increased allowable strains up to 200% as an alternative for attachment on a flexible system [75]. Other methods including fiber optics for deformation detection [76, 77] and external visual tracking systems [78]. Park *et al*. embedded five Fiber Bragg Grating (FBG) sensors in a rapid-prototyping robotic finger in which four for strain measurements and one for temperature compensation. The configuration is shown in **Figure 2.3.4**. The strains obtained from FBGs are computed to dynamic forces at a resolution of 0.01N at 20 Hz. External vision tracking systems, such as Optitrack, are not discussed in this context since it is impractical to implement in unstructured environments.

(a)   **(b)**
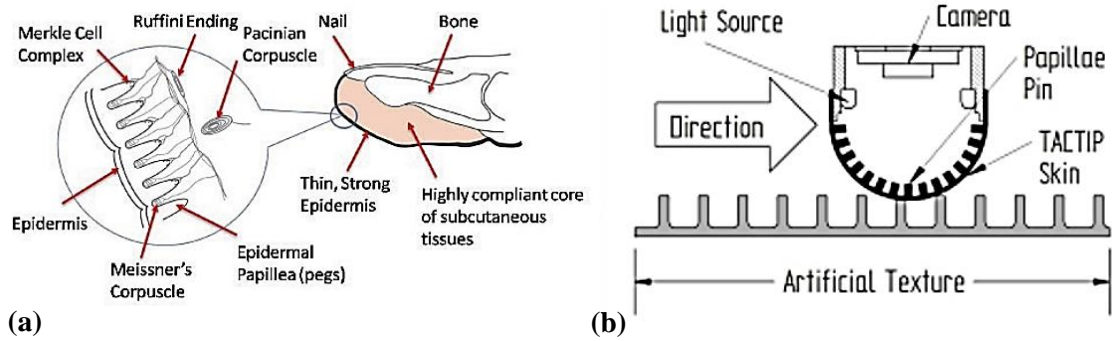
Figure 2.3.3 **(a)** Cross section of a human finger and **(b)** robot finger structure with a TACTIP skin. An embedded camera is used to capture the skin deformation. Tasks of pressure localization and gap identification can be accomplished [74].
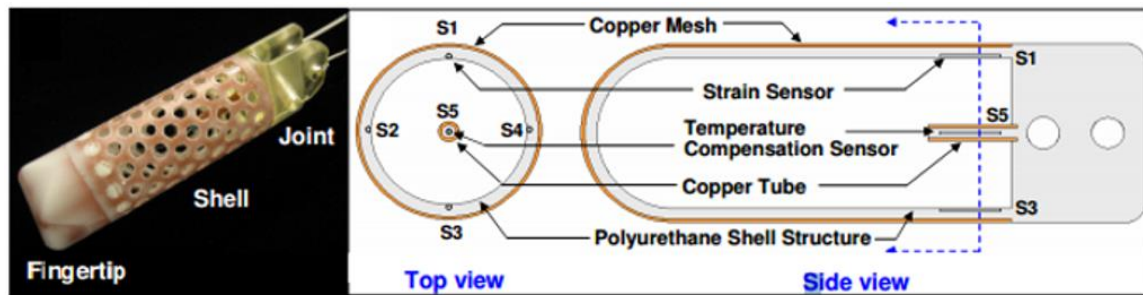
Figure 2.3.4 Five sensor fibers are embedded into a 3D printed fingertip prototype. The sensors (S1 – S4) measured external forces acting on the fingertip. The sensor at the center (S5) is used for temperature compensation.

The flexible strain sensors reviewed above mainly focused on the applications of wearable devices and textiles to measure body postures [79], deformations [80, 81] and gait [82]. Few flexible sensors are developed for robotic systems since past studies are in the field of rigid robotics and soft robotics are not yet considered in the past. The characteristics, advantages, and disadvantages of each sensing method above are summarized in **Table 2.3.2**.

17

Table 2.3.2 Summary on the advantages and disadvantages of flexible sensors. The advantages of using fiber optics in soft robots are highlighted in red.

	Gauge factor	Range of strain	Local measurement (uniqueness)	Ease of fabrication	Requirement of ext. infrastructure	Electromagnetic immunity
Resistive Ionic Sensors [28]	3.08	10 %	✗	✗	✗	✗
Piezoelectric [83], Piezoresistive [84], and Piezocapacitive Strain Sensors [85]	5.0 0.0001 0.005	0.056 % 0.15 % 150%	✗	✓	✗	✗
Capacitive Strain Sensors [86] [69]	-1.23	1 % 200%	✗	✓	✗	✗
Conductive Thermoplastic Resistive Strain Sensors [87]	1	50 %	✗	✗	✓	✗
Optical Sensing (image-based)	N/A	N/A	✓	N/A	✗	✗
Optical Sensing (strain/fiber-based) [88, 89]	0.795	1~5 %	✓	✓	✗	✓

2.3.3. 3D Curvature Sensing

3D shape sensing or 3D surface shape sensing is required for a soft robotic system to sense its configuration, to compensate and interact with external interferences. Currently, most of the researchers focused on sensing for fiber-like robots which required 3D shape sensing. However, few of them addressed on sensors for a general flexible robot which also requires global deformation measurement, i.e. a surface deformation. A surface shape soft sensor should be able to:

1. Measure surface deformation
2. Withstand bending, twisting or other deformation modes, while introducing the least resistance to soft body motions

These criteria indicate that the sensor should be flexible, compliant and soft relative to the soft robot design. The existing 3D shape (curvature) sensors are reviewed below and some 3D surface shape sensors are listed in the next section.

Recently, commercial cable-like flexible 3D curvature sensors have been developed for medical devices [90], structural [91-93] and robotic sensing [92]. TST innovation integrated helically coil foils with a cable to track changes in foil edges' distance and reconstruct the 3D cable shape with position and shape data in real time for cable assembly monitoring and rooters positioning [94]. Potential applications include packaged cable assemblies, cable delivery track and material monitoring.
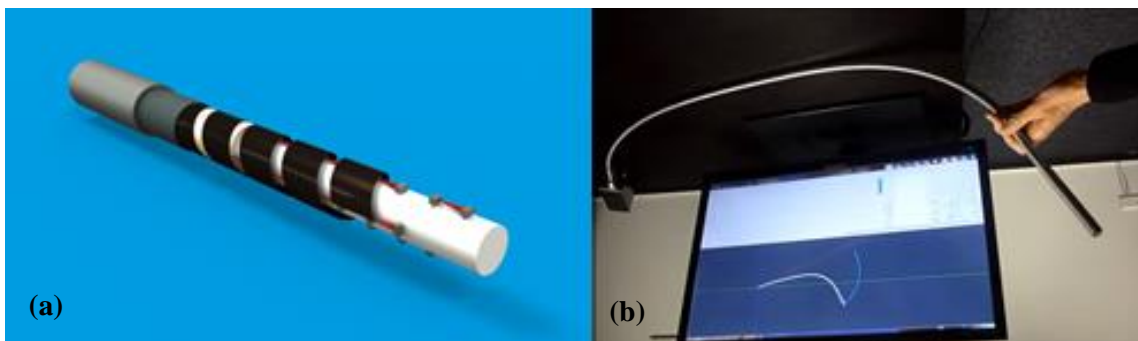
Figure 2.3.5 (a) 3D Model of TST's Innovative Cable-Like-Shape-Sensor [94]. Helically coiled foils are embedded into the cable-like structure. **(b)** Pitch distances among foil edges can be used to reconstruct a virtual cable model.

Shape-sensing optical fiber technology was developed by NASA in 1996 [95]. NASA researchers developed a demodulation method called Optical Frequency Domain Reflectometry (OFDR) to read over 10,000 FBG sensor signals in an optical fiber with a grating spacing less than 10 mm. OFDR uses a continuously tunable laser and light is reflected from the FBG sensors for interrogation. Thousands of FBGs can be detected and demodulated using this method. The FBG strain sensors are compact and lightweight and finally installed on the X-33 Launch Vehicle. Utilizing this technique, Luna Innovations developed a shape and position sensor to assist surgeons during surgery [96]. The sensor is used to measure the shape of surgical instruments in minimally invasive surgeries. The optical fiber consisted of multiple cores, each with linear and dense FBG arrays. The strain differences between the cores are used to compute and reconstruct fiber geometries on individual discrete elements as shown in **Figure 2.3.6**. With a high enough density of FBG sensors, general shapes of the fiber can be obtained. In recent years, this kind of shape sensing mechanism has also been applied to measure the shape of continuum robots [76, 97].
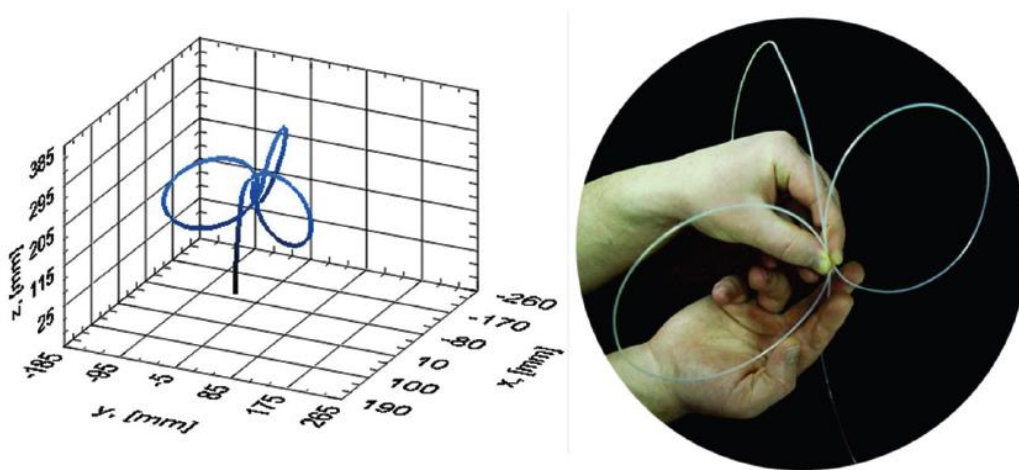
Figure 2.3.6 Accurate cable shape reconstruction by Luna Innovations' shape-sensing technology [95] . 3D bending curvatures at each point on the fiber are identified by the sensor.

These 3D fiber curvature sensors can be used to sense the shape of tubular or catheter-like soft robots. However, unable to sense a complete surface morphology or deformations for soft robots like [98], unless the relationship between curvatures and target surfaces are known. Moreover, multi-core fibers are generally expensive to be used in surface shape sensing. The work presented

20

in **Chapter 3 to 5** is to develop a sensing architecture to fill up the gap in soft robotic sensing systems.

2.3.4.   Surface Shape Sensor

Artificial skins are widely focused in wearable electronics field to mimic human skin as multi-functional sensors. In traditional robotics, artificial skins are fabricated to provide direct feedback during interaction between itself and the environment. However, the feedback will only become meaningful when the location and orientation of the sensors and surface morphology are known. Acquiring a proper knowledge of the robot configuration from 3D surface information, self-calibration and self-inspection can also be performed, which is desirable in many robotic systems.

In [99], a scalable, wireless and modular artificial skin sensor network is introduced to obtain 3D surface data for rigid robotic parts. A 3-axis accelerometer is embedded in each hexagonal shaped unit cell to capture its orientation information. Given the topological data of each sensor unit neighbors, a sensor network is formed. The corresponding position and orientation of the sensors can be calculated with respect to the local sensor unit coordinate system, thus regenerating the 3D surface of the robotic arm in 250 ms.

Figure 2.3.7 3D Reconstruction of a KUKA LWR arm [99]. The sensors are covered on the arm. The orientation of each sensor patch is transmitted to the micro-controller unit.

Morphosense ribbon [100] and MorphoShape [101] are large surface sensors for detection and monitoring of structural modifications with sensor arrays system. MorphoSense ribbon equipped with ribbon-like attitude sensors (**Figure 2.3.8**) to obtaining tangential data from spatial curve orientation along the ribbon. The surface is reconstructed and filled with the Coons-like method by estimating virtual missing curves with each reconstructed transversal ribbon. MorphoShape also used 3-axis micro accelerometers and micro magnetometers in its sensor network as Morphosense. A total of nine sensor nodes distributed on a square mesh evenly as shown in **Figure 2.3.9**. Curves are reconstructed individually similar to ribbon method [102] and surfaces in between are filled by orthogonal spline curves network which coincident on each sensors' location at a refresh rate of 15 Hz.
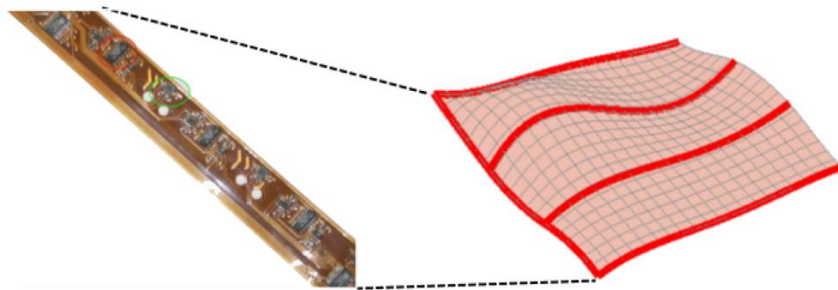
Figure 2.3.8 Global reconstruction of Morphosense surface [100]. Sensor ribbons (in red) are placed at the edges of a large flexible plate. Individual ribbon curves are reconstructed. Surfaces are formed by filling up the regions that are bounded by the ribbons.
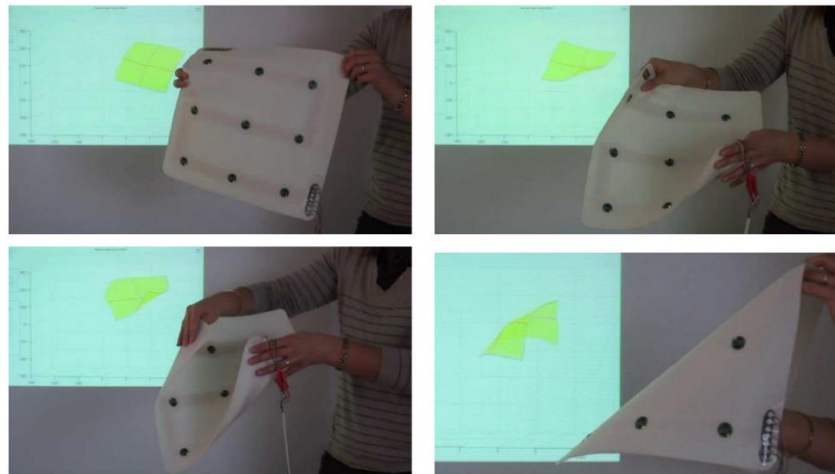
Figure 2.3.9 Visual results of MorphoShape shape reconstruction algorithm [101]. Nine sensors (shown as black nodes on the white film) are attached to the sensor ribbon. The reconstructed surface is plotted in Matlab in real time.

A well-known multinational technology company, Microsoft has also developed a flexible shape sensor as an input controller, named FlexSense [103]. Made from a thin-film, transparent surface, FlexSense contains 16 piezoelectric sensors at the outer ring to get bending information of itself. Sensors are designed to overlap each other to obtain additional knowledge on bending locations. Learning based algorithms are used as shape sensing algorithm and demonstrated with an average error of 0.015 m in real-time manipulation.
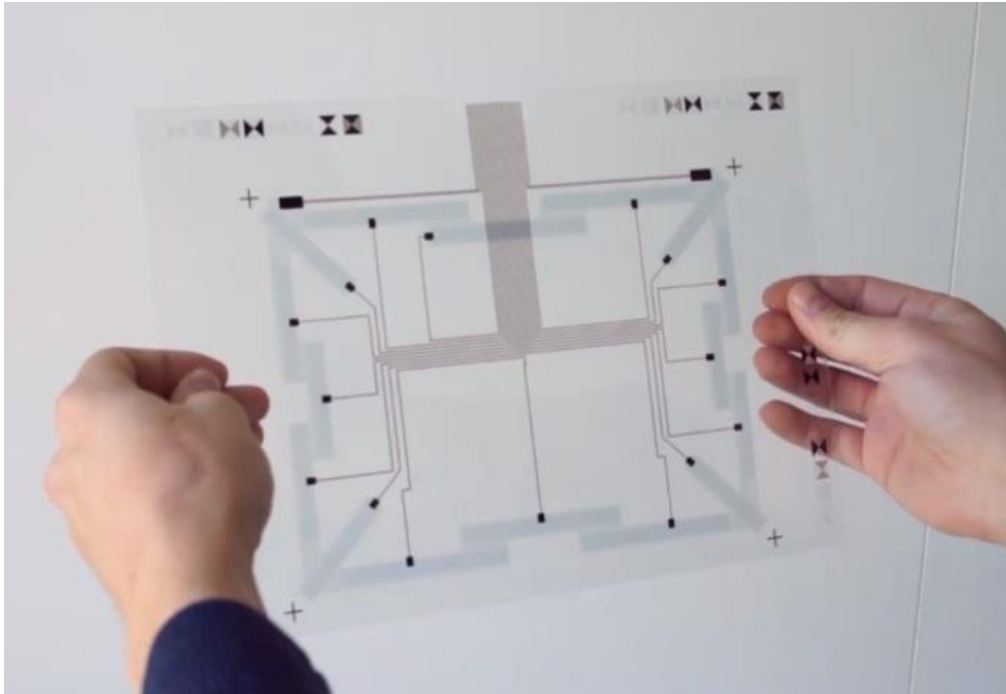
Figure 2.3.10 FlexSense's structure. Sixteen sparse printed piezoelectric sensors are distributed on a flexible, transparent film [103]. It can be used as an input device with real-time 3D shape reconstruction capability.

Recently, [104] presented a flexible surface sensing fabric. By using a high number of acceleration and magnetic sensor nodes and proposed global shape reconstruction algorithm, a reduction in the computation time to 0.72 ms is obtained, which is 40 times faster than local tangent method. The sensor is then applied to measure the shape of human splines for body posture analysis.
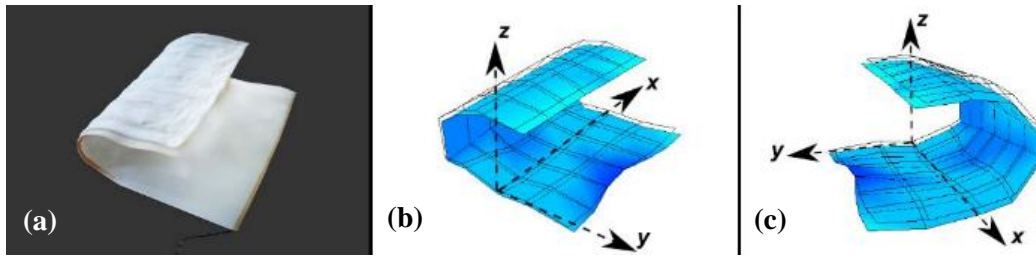
Figure 2.3.11 (a) Flexible surface sensing fabric (200 mm × 400 mm) in [104]. The sensor sheet is bent at 180°. **(b – c)** Virtual surfaces are reconstructed and sent to the smartphone via an Android application system at 10Hz.

Although external surface shape sensing devices are available in the market [78, 105-107], this work will focus on embedded shape sensor as soft robots are expected to work in an unstructured environment where external tracking devices are generally not applicable. The shape sensors introduced above demonstrate high reliability and accuracy. However, most of them are only applicable to tasks that exhibit tiny elastic deformation.

While soft robots usually actuate with elongation, compression, stretching and deformation patterns that rigid robots cannot perform [12], the existing sensors are not applicable to soft robots. Moreover, common sensors such as accelerometers and magnetometers are not immune to magnetic fields, where the soft robots are expected to have frequent contact with unknown environments, making these sensors not ideal to be used in soft robotics. Hence, we presented a fiber-optic based shape sensing system in this work.

2.4. Fiber Optics

2.4.1.   *Fiber Bragg Gratings (FBGs) Background*

Fiber Bragg gratings are first discovered by Hill *et al.* [108]. Strains can be measured from FBG signals like traditional metal foil strain gages by considering strain-wavelength relation of the fiber. Diverse types of transducers can be built by using FBGs to measure physical quantities such as acceleration and force. In this work, FBGs are applied for local strain measurements. Compare to

24

conventional sensors, FBGs have unique advantages including multiplexing, multifunctionality, long transmission distance with high signal integrity, electric isolation and electromagnetic immunity. The strengths and weaknesses of FBGs are summarized in **Table 2.4.1**. The high strain sensitivity and electromagnetic immunity make fiber optics favorable in developing soft robotic sensor.

FBGs are fabricated by exposing a short length of photosensitive fiber to periodic distribution of light intensity, using holographic interference or a phase mask [109]. This permanently changed the refractive index of that fiber segment which reflects a wavelength when a board-spectrum light is transmitted into the fiber, as shown in **Figure 2.4.1**. When strain is induced in the fiber, no matter mechanical or thermal strain, a change in the gratings separation will be introduced, thus causing a change in refractive index simultaneously. This will lead to a peak shift in the reflected spectrum. When the applied strain releases, the gratings separation springs back to normal condition and the shift in Bragg wavelength reduces to zero. This allows one to measure and monitor physical parameters [110] such as strains [111-113] and vibrations [114].
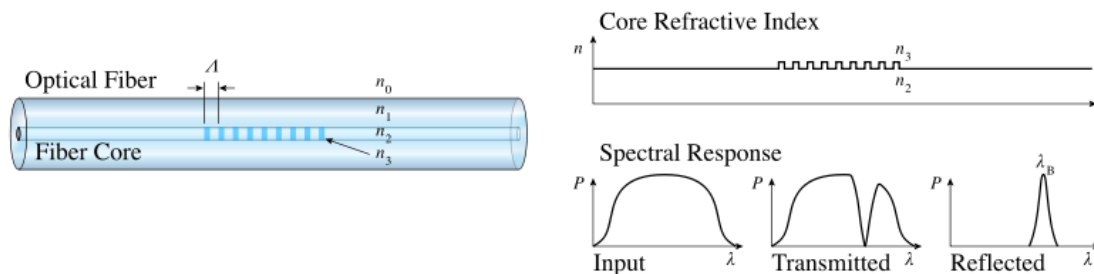
Figure 2.4.1 Working principle of fiber Bragg gratings [115]. Total internal reflection occurs when the broadband light spectrum travels to the end of the fiber. FBGs, which act as optical mirrors, only reflect particular wavelengths and transmit those not reflected. .

2.4.2. *Bragg Wavelength Detection*

Strain sensitivity

Fiber Bragg Gratings are a type of intrinsic optical sensors which respond to environmental parameters. In each grating, the refractive index of the fiber core is permanently increased by

exposing the fiber laterally to an intense ultraviolet beam with a periodic pattern. The refractive modulation index is fixed and determined by the pattern of UV exposure.

A small amount of light (typically around 10%) is reflected at each grating. When the incident light is approximately double the grating period, the reflected light signals are transmitted back in form of a reflected spectrum due to the multiplexing property of FBGs. The wavelength at which this reflection occurs is called the Bragg wavelength and the condition is well known as the Bragg condition:

$$\lambda_B = 2n_e \Lambda \tag{2.4.1}$$

where λ_B is the reflected wavelength or Bragg wavelength, n_e is the effective refractive index and Λ is the grating period.

The wavelengths that are phase mismatched will not be reflected thus transmit to the fiber end as shown in **Figure 2.4.2**. Since wavelengths will be reflected back only when the Bragg condition is satisfied, attenuation and signal variation are generally negligible. This demonstrates a fundamental advantage of fiber Bragg gratings that ensure a high accuracy of grating wavelength measurements.
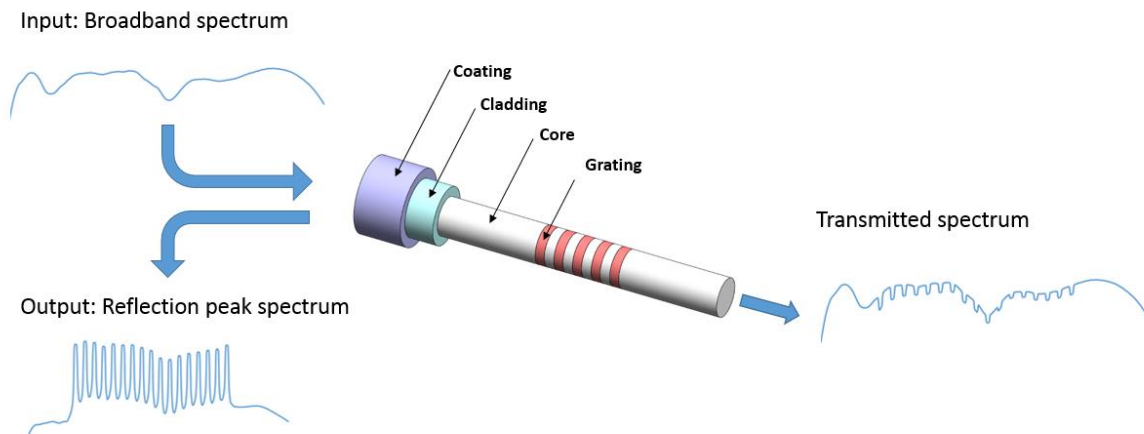
Figure 2.4.2 FBG working principle. Each grating has a fixed index modulation which reflects a particular wavelength of light. For the wavelengths that do not satisfy the Bragg condition will simply transmit to the fiber end. Due to the temperature and strain dependence of the grating parameters, the reflected wavelengths will also change. This enables the sensing of strains or temperatures.

From **Equation (2.4.1)**, the shift in central wavelength of the reflected component, or Bragg wavelength, depends on the effective refractive index and the grating period which are a function of temperature and strain. Therefore, the sensing response varies when our proposed sensor experiences temperature changes or under external forces. When external forces are applied to the sensor, compression or tension stresses will be induced along the whole fiber. The sensor deformation will be transferred to a series of fiber strains which correlates to the strain transfer ratio and bonding quality. The mechanical strains generated which change the grating period and the effective refractive index, resulting in shifts in Bragg wavelengths [157]. Including the effect of temperature, this allows strain and temperature measurements by the reflected FBG spectrum in real-time. This dependency is described as follows:

$$\frac{\Delta\lambda}{\lambda_0} = k\varepsilon + \alpha_\delta \Delta T \tag{2.4.2}$$

$$\alpha_\delta = \frac{\partial n}{n\Delta T} \tag{2.4.3}$$

Where ε is the strain, $\Delta\lambda$ is the wavelength shift, ΔT is the change in temperature in the unit of K, λ_0 is the base wavelength at fabrication, k is the gage factor = 0.78, α_δ is the change of refraction index and n is the refractive index of the fiber.

$$\varepsilon = \varepsilon_m + \varepsilon_T \tag{2.4.4}$$

Where ε_m is the mechanical-induced strain component, and ε_T is the temperature-induced strain.

$$\varepsilon_T = \alpha_{sp}\Delta T \tag{2.4.5}$$

$$\frac{\Delta\lambda}{\lambda_0} = k\varepsilon_m + \left(k\alpha_{sp} + \alpha_\delta\right)\Delta T \tag{2.4.6}$$

Where α_{sp} is the expansion coefficient per K of the specimen, α_δ is the change of refraction index and ΔT is the change in temperature in K.
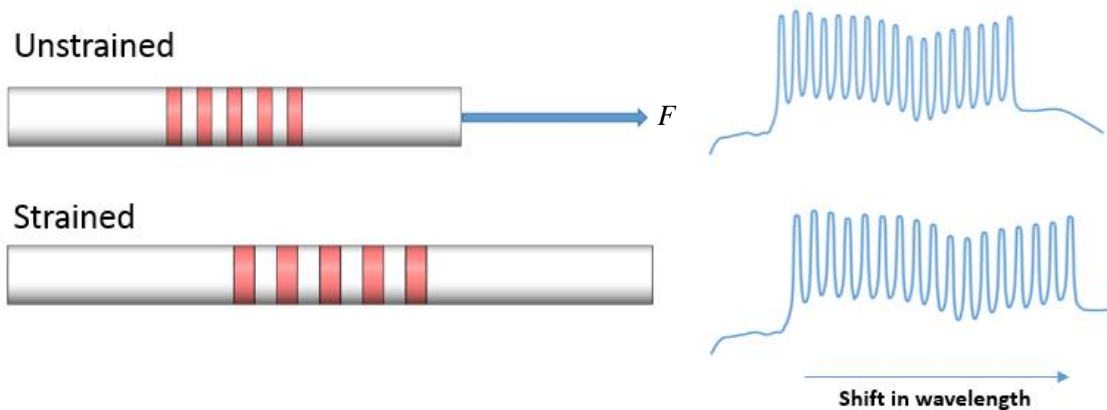
Figure 2.4.3 Strain response due to intrinsic FBG characteristic. When the optical fiber experiences mechanical stress or temperature variations, the induced strains will change the grating separations which affect refractive indices of the gratings. The reflected wavelengths thus will shift from the neural wavelengths due to these changes. By measuring the shifts in wavelength, the induced strains can be interpreted using **Equation (2.4.6)**.

Typical values for temperature sensitivity and strain sensitivity of the FBG are 12 pm/$^\circ$C and 1.3 pm/$\mu\varepsilon$. As the fiber possesses cylindrical geometry of high aspect ratio the FBG is highly sensitive to strain in the longitudinal direction as compared to the transverse or out of plane strain. The first expression in **Equation (2.4.6)** describes the influence of mechanical strains and the second expression refers to the change in glass refraction index n and temperature strains, which is solely depending on temperature. The temperature strains are induced from the specimen strain, therefore, the specimen thermal expansion coefficient is considered instead of thermal expansion coefficient of glass.

For a FBG is bonded to a zero mechanical strain region on a substrate or specimen, i.e. $\varepsilon_m = 0$, it acts as a temperature sensor. The change in temperature ΔT can be calculated by:

$$\frac{\Delta\lambda}{\lambda_0} = \left(k\alpha_{sp} + \alpha_\delta\right)\Delta T \tag{2.4.7}$$

$$\Delta T = \frac{\Delta\lambda}{\lambda_0\left(k\alpha_{sp} + \alpha_{\delta}\right)} \tag{2.4.8}$$

2.4.3.   2.4.3 Temperature Compensation

As the temperature has an impact on sensing signals, temperature compensation has to be done to get precise strain measurements. Conventionally an additional temperature grating is applied and used to correct other strain measuring gratings. The simplest way is to measure the temperature only using a FBG sensor located at zero mechanical strain position. At $\varepsilon_m = 0$, the wavelength shift of the compensation FBG, $\Delta\lambda_c$ is given by **Equation (2.4.7)** and the resultant wavelength shift of active mechanical and temperature strain measuring FBG, $\Delta\lambda_m$ is given by:

$$\frac{\Delta\lambda_c}{\lambda_{0c}} = \left(k\alpha_{sp} + \alpha_{\delta}\right)\Delta T \tag{2.4.9}$$

$$\frac{\Delta\lambda_m}{\lambda_{0m}} = k\varepsilon_m + \left(k\alpha_{sp} + \alpha_{\delta}\right)\Delta T \tag{2.4.10}$$

Subtracting **Equation (2.4.10)** by **Equation (2.4.9)**,

$$\frac{\Delta\lambda_m}{\lambda_{0m}} - \frac{\Delta\lambda_c}{\lambda_{0c}} = k\varepsilon_m \tag{2.4.11}$$

$$\varepsilon_m = \frac{1}{k}\left(\frac{\Delta\lambda_m}{\lambda_{0m}} - \frac{\Delta\lambda_c}{\lambda_{0c}}\right) \tag{2.4.12}$$

where λ_{0c} is the central wavelength of the compensation FBG and λ_{0m} is the central wavelength of the mechanical strain measuring FBG. In this work, the 17th FBG where $\lambda_{0c} = 1540$nm is used as a temperature compensation FBG.

By placing a compensation FBG in a zero mechanical region, correct mechanical strains can be computed by compensating the wavelength shift using **Equation (2.4.12)**. For the case that a zero mechanical strain region is not available, e.g. due to application requirements, a FBG for pure temperature measuring can be used. Replacing ΔT in **Equation (2.4.6)** by the value in **(2.4.8)**:

$$\varepsilon_m = \frac{1}{k}\left[\frac{\Delta\lambda_m}{\lambda_{0m}} - \frac{\Delta\lambda_T}{\lambda_{0T}}\left(\frac{k\alpha_{sp}+\alpha_\delta}{k\alpha_{glass}+\alpha_\delta}\right)\right] \tag{2.4.13}$$

Note that the compensated wavelength value can also be calculated by using other pure temperature measuring devices.

Table 2.4.1 Strengths and weaknesses of FBG sensors when compared to conventional metal foil strain gauges.

Strengths	Weaknesses
✓ Easy to integrate with new composites reinforced with glass and carbon fiber	➢ Higher cost
✓ Small and lightweight	➢ High-temperature dependence
✓ Immune to electromagnetic interference	➢ Low gage factor
✓ Intrinsically passive, no electricity required	➢ Stiffer than foil gages
✓ Long transmission distance (Over 50 km)	➢ Require special test equipment for fixing errors
✓ A single fiber can accommodate multiple sensors	➢ Require interrogator
✓ High long-term stability	
✓ Corrosion resistance	
✓ Can work in a high-temperature environment (> 700 °C)	
✓ Low magnetic field interaction	
✓ Easy to cable, test, and install	

2.4.4. *FBGs Applications*

FBG sensors are used in a wide range of applications after recent advances in grating formation, fabrication and interrogating techniques [116]. Besides optical applications, they have been integrated into composite spars for wing load monitoring [117], a MRI-compactible tactile sensor for force measurement [118], a planar structure for external impact detection and localization by artificial intelligence [119], temperature sensors under different sea levels [120], overhead power transmission lines for fault detection and plate structures for structural damage detection [121, 122].

Currently, most of the available single-core FBG sensor is 9 µm in diameter and 0.15 / 0.25 mm in diameter for fibers coated with outer cladding and a protective polymer layer. The polymer coating also allows better bonding between the fiber and the substrate, so it is simple to attach or embed FBGs for strain measurements. Application examples of FBG strain sensor are reviewed below.

Silva *et al.* presented a soft wearable glove for monitoring hand gestures and posture [123]. A single mode fiber is embedded into the midplane of a PVC thin film which is 900 µm thick. FBGs are located at the position coincident with 14 finger joints which elongation varies from 0 to 14% strain. The strain variation will generate a wavelength shift in 1 nm so over 30 FBGs can be accommodated in a single fiber within the whole C-band. Maximum error obtained by finger bending from 0 to 90 degree is 2 degrees.

[113] demonstrated real-time position, shape and twist measurements on a loaded planar structure. Two configurations of fiber are investigated, i.e. spiral plate and grid plate routing, to simulate coating defects in high-temperature sensing experiment. Promising results obtained with high accuracy even at 1000 °C in the surrounding environment. This result showed the high reliability of FBGs under extreme temperature.

Other applications using FBG strain data including static load tests [111], monitoring systems for magnetic actuators [124], strain measurements in rock specimens [125] and dynamic strain measurement on composite beams [126]. Although FBG was proven its reliability and immunity to various environments, commercial FBG interrogators are usually large in size which limited the fields of application. Thanks to recent miniaturization of the interrogator size [127], FBG sensing

systems become smaller and more compact and potentially capable of being used in stand-alone systems.

2.5. Surface Shape Reconstruction Algorithms

Measuring a 3D surface shape of an object is essential for many applications, including reverse engineering [128], 3D printed implants making [129], creating hybrid reality [130], 3D portrait making [131] and structural health monitoring [132]. Ways to achieve 3D surface shape sensing can be classified into two categories, contact, and non-contact methods. Non-contact types of 3D scanning utilized 3D scanners to measure dense dataset of the target surfaces which usually use lights or radiations. In particular, laser-scanning confocal microscopes, white light interferometry chromatic confocal method are the most common ways to obtain high dense surface information. However, these methods required external equipment such as tracking camera and a large volume of space relative to the targeted object. Moreover, the requirement on the surroundings and the environment is tight due to interference issues. These limited the usage of non-contact type shape sensor in general. Recently, combining cameras and transparent gel, [133] built a kind of contact-based camera sensing system which used colored lights and computer vision algorithm to reconstruct object shapes, hardness, and contact pressures. However, it is worth to take note that the above sensors are not good solutions to soft robotic sensing as their bulky nature and could not provide reasonable flexibility to soft robots.

On the other hand, contact type sensors collect surface information by directly attaching on the target surface. The surface data are retrieved and measured exactly add the location of the sensors. Comparing to non-contact types, these sensors are more applicable to the tasks required mobile ability or the missions that located at unconstrained areas. Note that depending on the type of sensor material, the sensor may modify the original robot kinematics and the level of detail, or resolution is generally lower than the non-contact type. Since the measurements from this type of sensors are low dense comparing to non-contact type and are not capturing the surface shape directly, reconstruction algorithms are required to compute the surface geometry. In this work, a contact type sensing element, i.e. FBG, is used to build our proposed surface shape sensor. The reconstruction techniques in prior arts are reviewed below.

2.5.1. *Strain-Based Displacement Mode Superposition Method*

The strain data-based displacement mode superposition method applied a modal transformation formulation to estimate out-of-plane displacements from in-plane strain measurements [134, 135]. Firstly, accelerometer frequency response functions and strain frequency response functions are obtained to figure out the displacement and strain modes from modal testing. A least squares transformation in modal coordinates is then derived from the strain measurements. The displacements are then computed from the displacement modes by transforming the modal coordinates. The displacement vector $\boldsymbol{\delta}$ and strain vector $\boldsymbol{\varepsilon}$ in modal coordinates are defined as follows:

$$\boldsymbol{\delta} = \mathbf{Dq} \tag{2.5.1}$$

$$\boldsymbol{\varepsilon} = \mathbf{Sq} \tag{2.5.2}$$

where $\boldsymbol{\delta}, \boldsymbol{\varepsilon} \in \mathbb{R}^n$, $\mathbf{D} \in \mathbb{R}^{n \times n}$ is a displacement mode matrix, $\mathbf{S} \in \mathbb{R}^{n \times n}$ is a strain mode matrix and $\mathbf{q} \in \mathbb{R}^{1 \times n}$ is a modal vector.

Rewrite **Equation (2.5.2)** by least squares approximation:

$$\mathbf{q} = \left[\mathbf{S^T S} \right]^{-1} \mathbf{S^T \varepsilon} \tag{2.5.3}$$

Back substituting to **Equation (2.5.1),** the displacements could be obtained from the strains with modal transformation matrix:

$$\boldsymbol{\delta} = \mathbf{D} \left[\mathbf{S^T S} \right]^{-1} \mathbf{S^T \varepsilon} \tag{2.5.4}$$

The limitation of this method is that the rank of strain modal transformation matrix must be lower than the number of strain sensors. The available mode shapes are required for higher order modes such as high-frequency vibrations and deformations. In this work, the number of mode shapes is

large and difficult to be obtained via traditional modal testing. Also, this method is only suitable for small amplitude cases.

2.5.2. Curvature-Based Geometrical Iteration Method

The idea of curvature data-based geometrical iteration method is to convert strain data into curvatures and interpolate by satisfying the curvature continuity. The curvatures could be obtained by linearly interpolating the measured strains. A common way to apply this method is to compute orthogonal curvatures by placing the sensor arrays in an orthogonal configuration as shown in **Figure 2.5.1**.

The strain-curvature for a bending beam is given by:

$$\varepsilon = \frac{y}{R} = \kappa y \tag{2.5.5}$$

where ε is the bending strain at an offset distance y from the neutral plane of the beam, R is the bending radius and κ is the bending curvature.

When the targeted structure deforms, the deformation will generate surface strains along the whole structure except the neutral plane. These strains could be interpreted as bending curvatures, using **Equation (2.5.5)**. Given the curvatures on the structure surface, many interpolation algorithms could be applied, such as non-uniform rational B-splines (NURBS) curves and surfaces which are standard representation in a computer-aided geometric design that is usually used to represent the object shape [136].

The major limitation of this method is the pre-condition that assuming the shear transverse strains on the curved surface are zeros which are not practical in soft surface sensing, unless the surface is constrained by a rigid layer such as paper.
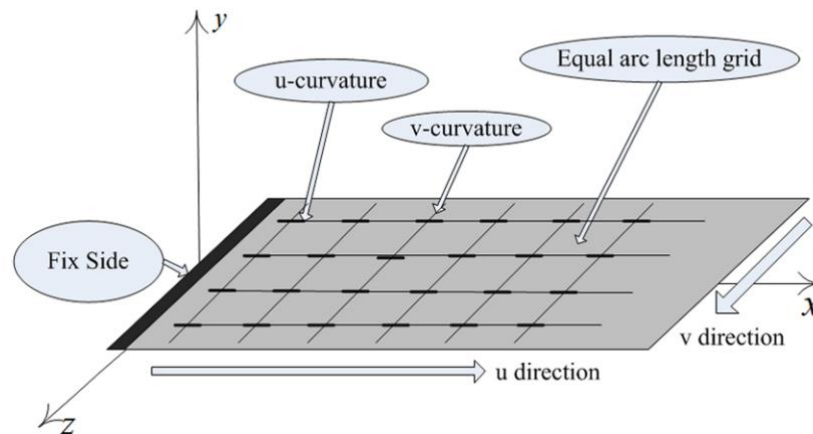
Figure 2.5.1 Typical sensor array configuration for orthogonal curvature sensing in [137]. Sensors are placed along *x*- and *z*- directions with equal separations.

2.5.3.   *Inverse Finite Element Method (iFEM)*

Inverse Finite Element Method (iFEM) originated from Tessler and Spangler [138, 139], based on mechanical relations of the inverse elements. By minimizing a least-square functional with analytical and experimental strains, it can estimate the static and dynamic behavior of the interested structure and reconstruct the surface shape, given the boundary conditions and information of constraints. The major advantage of iFEM is that loading and material information are not required for solving the equations. The robustness of the iFEM formulation is proven by applying to real-time structural health management in NASA [140]. The method is used to monitor aerospace vehicles and preventing accidents caused by structural failures. Accurate three-dimensional displacements, stresses, and strains fields are reconstructed with iFEM for shear deformable shell structures.
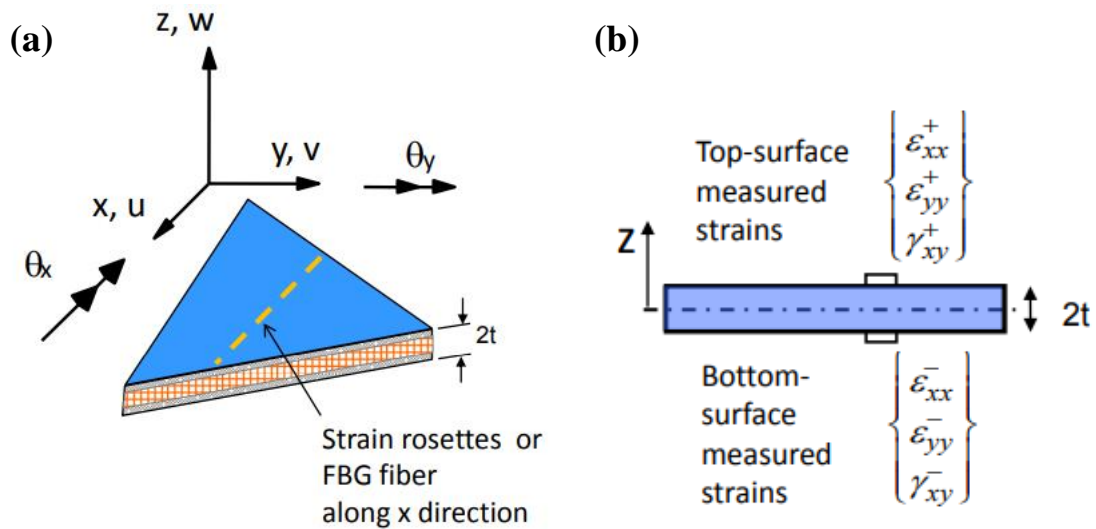
Figure 2.5.2 (a) Typical three-node inverse shell element (iMIN3) from [141]. The reference frame is aligned with the directions for strain measurement. **(b)** Strain sensors are placed on the top and bottom surfaces of a plate structure. In-plane strains and transfer-shear strains are measured by the strain sensors. The measured strains are evaluated using the weighted least-squares smoothing functional with respect to the unknown displacement degrees of freedom.

Recent works focused on the development of a new inverse shell [139, 142] and beam elements [143]. One limitation of iFEM is the need of strain rosettes to reconstruct shapes from torsion [144]. Also, for non-membrane structure, there must be sensors embedded inside the targeted structure. This limited the fiber routing design and made the surface shape sensor fabrication process complex. Moreover, the deformation reconstructed in the above applications are relatively small comparing to the deformation of soft robots. In chapter 4, a data-driven modeling approach is used that allowing simpler fiber routing configuration and reducing fabrication difficulties.

香港大學 圖書館 HKU Libraries

2.6.   Conclusions

In this chapter, a detailed review of soft robotic systems is presented. Flexible sensors are also briefly reviewed. The main objective of this chapter is to introduce the motivation and background for the development of soft robotic sensing systems. Soft sensors are introduced to provide deformation or surface shape information. The review helped to analyze the desirable sensor materials and designing flexible sensors for soft robots. While many soft robots are developed recently, only a few of them provided position or force feedbacks from their deformed bodies. The advantage of adopting soft sensors in soft robotic systems is obvious, including deformation feedbacks for self-monitoring and external force estimation. The remaining structure of this thesis is presented as follows. **Chapter 3** discussed and analyzed the procedures for designing a fiber-based soft sensor and analyzing the sensor parameters using Finite Element Modeling technique. **Chapter 4** presented the fabrication and modeling of the proposed sensor. **Chapter 5** discussed the experimental results and limitations of this work. **Chapter 6** presented the conclusion and future works.

3. Finite Element Analysis (FEA) on Sensor Morphology

3.1.   Introduction

This chapter briefly analyzed the deformation patterns of soft robots with finite element simulations. A strain-based methodology is adopted to design the sensor structure based on strain field information from simplified deformation patterns. Strain fields on the sensor surface are extracted and reconstructed from global deformation patterns due to bending and twisting motions, and local deformation patterns due to pushing motions. Three sensor structures are proposed to identify each deformation pattern with the consideration of deformation patterns discrimination. Corresponding sensor responses are generated and analyzed from finite element simulations. A final simplified sensor shape is selected by comparing its sensor responses in terms of sensitivity, stress concentration on sensing fiber and the ease of implementation. The effect of sensor thickness, sensor fiber offset, and fiber stiffness are discussed with simulated results. The overall sensor stretchability due to different fiber routing configurations is also discussed at the end of this chapter.

3.2.   Sensor Morphology Design

Biological organisms provided evidence and insights to design soft robots and their motion patterns are closely related to deformation patterns of soft robots. Examples such as soft tentacle manipulators, which originated from octopus arms, have demonstrated motions with a high degree of freedoms [145, 146]. Complex motions generated by these actuators can be simplified into elongation, contraction, torsion, and bending, similar to octopus in the biological sense [147]. This demonstrated the importance of studies in animals' motion patterns. A number of studies also indicated that complex motions of soft creatures can be generated by actuation of single or combination of principle postures [145, 148].

Considering simplified robot motion patterns and observations on soft animals, this work focused on soft sensor designs to capture the most common patterns generated in soft robots, i.e. bending and twisting. Local stimulates on the soft sensor resulting in local deformations are also studied. **Figure 3.2.1** shows some typical motion patterns generated from natural creatures.

39

Figure 3.2.1 Motion patterns generated by soft creatures: manta rays swim with disc-like bodies (Left) and octopuses with tentacles (Right).

FBGs have high multiplexing capability to form sensing networks for applications in different scales. In this study, we first worked on a small-scaled silicone substrate with embedded gratings. To make our surface shape sensor flexible and applicable, three major design considerations are discussed as follows:

a) Flexibility

Soft robots are generally highly compliance with the working environments. Sensors that integrate with soft and deformable robots must be adequately flexible to the robot body and surroundings. Silicone rubber is chosen as the substrate layer for high compliance and firm bonding with common soft robots fabricated with silicone.

b) Stretchability

Surface shape sensors usually designed with grid-form sensing networks. However, this configuration can heavily limit the degree of flexibility and stretchability especially when in-plane loadings exist In-plane loadings are commonly found in soft robotic applications due to stretching. The proposed fiber layout in the sensor allows stretchability along different directions. Since the requirement of stretchability varies with applications, discussions on sensor placement are not covered in this work.

c) Reliability

In contrast to rigid robots, soft robots value contact with unknown environments. FBGs provide excellent durability to harsh environments including dramatic temperature changes and chemical corrosions [149]. This ensures long-term stability and reliability of our proposed sensor. In this work, Draw Tower Gratings (DTGs) are selected instead of conventional gratings which can offer over four times mechanical strength when compared to classical FBGs.

To design a proper sensor morphology for deformation patterns sensing, studies and analysis are carried out of the three deformation patterns mentioned above. In this work, deformation patterns are captured by FBG strain sensors due to their excellent EM immunity and strain sensitivity. Strain fields are measured from FBGs to provide geometric information of the soft sensor. Assuming elasticity, each deformation pattern refers to a unique strain field pattern. Utilizing strain information on sensor surface under different deformations, unique regions are identified, clustered and represented by strain vectors. These strain vectors indicated the locations where sensor responses are most sensitive when the fiber is aligned along that particular strain vector direction of the region of interest. The design of sensor morphology is divided into 4 parts: deformation pattern and finite element modeling, strain fields extraction, strain regions clustering and sensor responses analysis. The objective of this sensor morphology design is to find out a simple design to capture targeted deformation patterns. Detailed steps are explained in the following sections and sensor fabrication and modeling are presented in **Section 4.2**.

3.2.1.   Finite Element Modeling of Deformation Patterns

Bending, twisting and local pushing motions on a soft plate are simulated using a commercial software Abaqus 6.14. Abaqus is used to model part instances of the soft sensor and generate 3D deformation results with displacement, stress and strain outputs. The soft sensor is discretized to element blocks of different shapes and approximated the original sensor shape. Each element is associated with a user-defined material property and element type. The element size can be adjusted by varying global and local element seeds for a better sensor shape representation.

The first proposed sensor is a square plate of 100 mm side length and 5 mm height. A linear hexagonal hybrid element C3D8RH is selected for the soft sensor body with constant pressure, reduced integration, and hourless control. A hybrid truss element is chosen for the fiber sensor with 2-node linear displacement and responses to axial forces. Ecoflex 30 is used as the sensor substrate is used in this work. From literature [150], the sensor body material is assigned with three-term hyperelastic Ogden model where the coefficients are: μ_1 = 0.024361, μ_2 = 6.6703×10^{-5}, μ_3 = 4.5381×10^{-4}, α_1 = 1.7138, α_2 = 7.0679, α_3 = -3.3659, D_1 = 3.2587, $D_2 = D_3$ = 0. The modulus and poison ratio of the silica FBG fiber are 70GPa and 0.16 respectively. The fiber truss element cross-section is defined as 0.049087 mm^2 considering a standard 250 µm diameter buffer.

External forces and moments are applied to the sensor model with properly assigned boundary conditions to generate desired patterns. The sensor plate is first partitioned by 8 lines for setting boundary conditions. Four nodes and nine geometry sets are defined for convergence study and applying external forces as shown in **Figure 3.2.2**. Consider negative bending moments about the x-axis, the displacement of 2 vertical lines 1-2 and 3-4 are constrained along the z-direction, the displacement of a horizontal line in the middle of the plate is constrained along the y-direction and the displacement of a vertical line in the middle of the plate is constrained along the x-direction. A cylinder with a diameter of Ø 50 mm and 100 mm tall is then placed on top of the plate. Interaction properties are set as no-slip and frictionless between the sensor body surface and cylinder surface. To create pure bending motion, the displacement of the cylinder is increased along the z-direction. Twisting motions are simulated by fixing the displacement along x-, y-, z-direction on one side of the sensor plate. Moments are applied at the free end. Pushing motions are simulated by setting 9 boundary conditions on the sensor plate and limiting the movement along x- and y-axis while applying displacement along z-direction on the target pushing location. The corresponding setting on boundary conditions and loads and the respective deformation patterns are visualized in **Figure 3.2.3**.
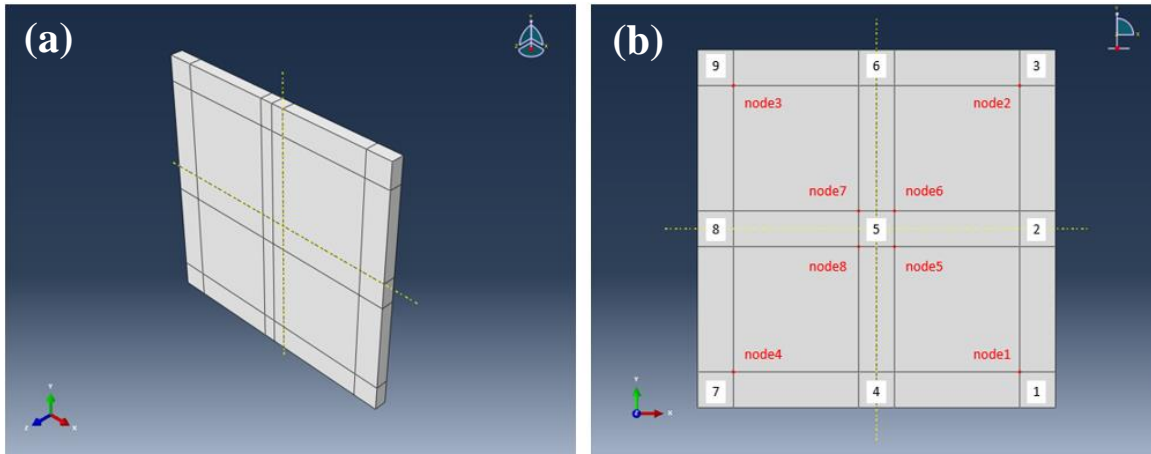
Figure 3.2.2 (a) Sensor model partitioning using Abaqus. **(b)** Nine surface sets are defined and labeled from the bottom right corner to top left corner. Eight nodes are defined and monitored during convergence studies.
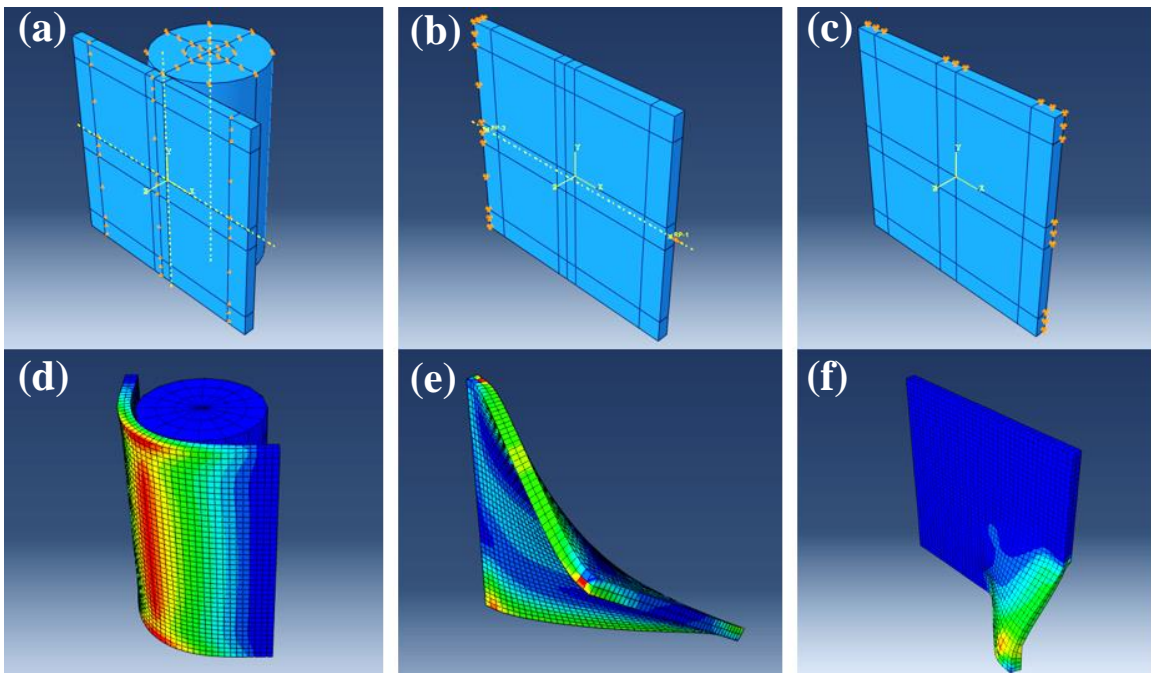
Figure 3.2.3 (a – c) Boundary conditions and loadings applied on the sensor plate body for 3 principal deformation patterns. The simulated results of the corresponding deformation patterns: **(d)** bending, **(e)** twisting and **(f)** local pushing.

Good meshing quality for the sensor model can provide an accurate simulation result. However, very fine meshes are impractical in terms of convergence and computation time. The idea of FEM convergence testing is to identify an element size that provides accurate enough solutions. To figure out the suitable element size of the sensor body, a number of simulations are computed with the three deformation patterns and different element size n, i.e. 1, 2.5, 5 and 10. Since strain is the main interest in this work, the maximum principle logarithmic strain is set as the output to evaluate the quality of the meshes. Twenty simulations are done and 160 logarithmic strains are extracted from the element nodal. The convergence figures of the principal deformations, i.e. bending and twisting, are shown in **Figure 3.2.4** and a visualization plot on the solution convergence is shown in **Figure 3.2.5**.

(b)   Bending
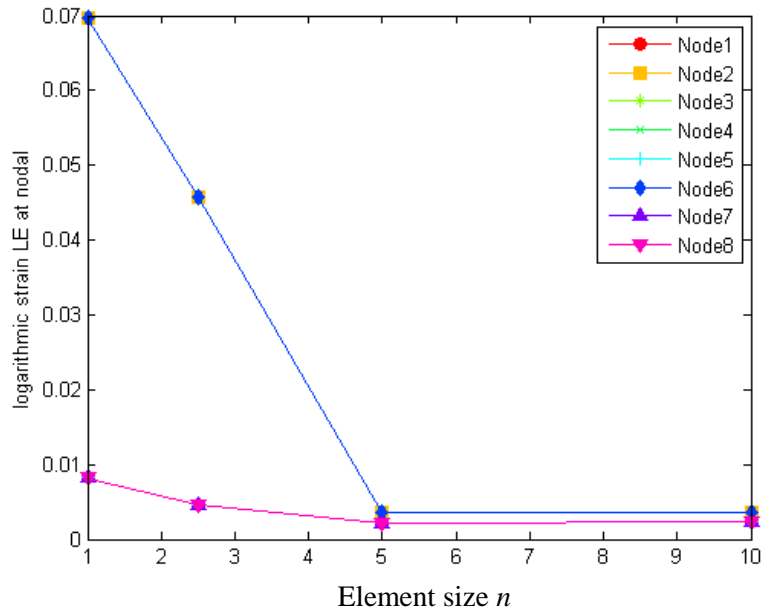
(a)   Twisting
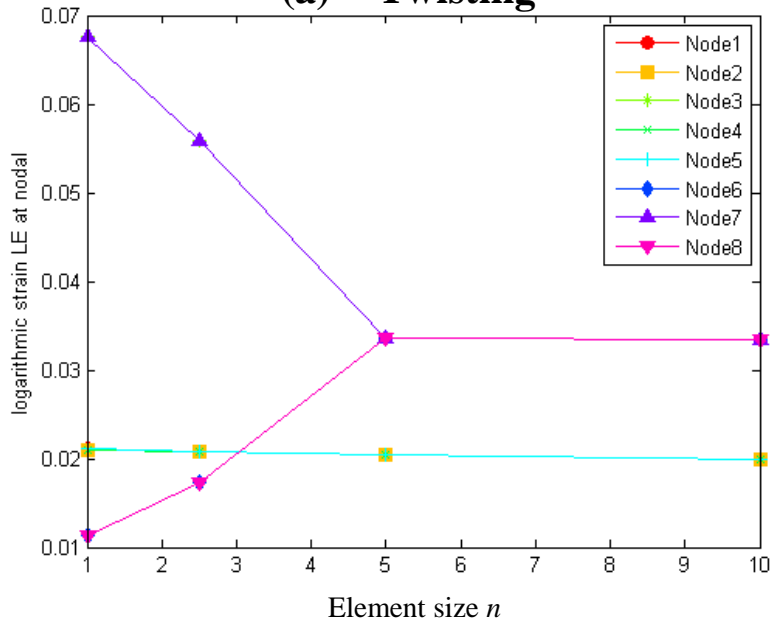
Figure 3.2.4 Convergence studies in finite element simulations. Simulations are performed under **(a)** plate bending and **(b)** twisting. Nodes are defined in **Figure 3.2.2**. The logarithmic strain value started to converge from $n < 5$.
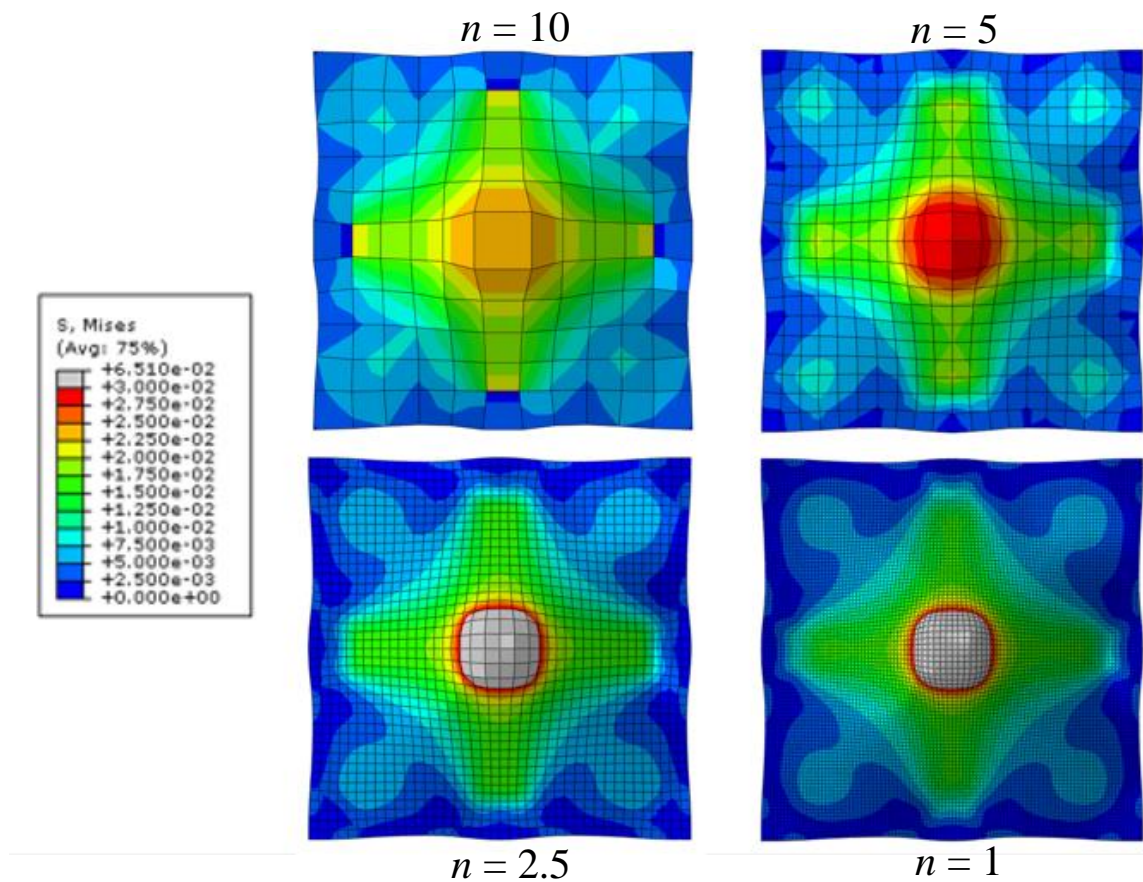
Figure 3.2.5 Stress field visualization of refined meshes. From $n = 10$ to 1, stress distributions became more accurate.

From the results of convergence studies carried out above, an element size of $n = 2.5$ is chosen for the soft sensor body in the remaining simulations. The sensor model is then discretized into 3200 elements which consist of 2 layers of 40×40 elements.

3.2.2.   *Extraction of Strain Vectors*

With a proper boundary and load settings, finite element simulations are used to find out the unique strain patterns generated from the 3 selected deformation modes. For simplicity, strain fields are extracted from the top surface of the soft sensor. It is reasonable since the FBG strain sensor is

placed on the soft sensor surface and only strains on the sensor surface are being measured. 2 global deformation patterns and local deformations at 3 positions considered and simulated. Strains along *x* and *y* directions and the positions of the elements are outputted in the following format for further analysis: [Element number, *x* position, *y* position, strain E13, strain E23]. Resultant strain fields are plotted by summing the strain fields along E13 and E23 directions. The extracted resultant strain fields are then used for clustering analysis in the next section. **Figure 3.2.7** - **Figure 3.2.9** showed the strain fields in E13 and E23 direction and the resultant field generated from local pushing on the sensor center.
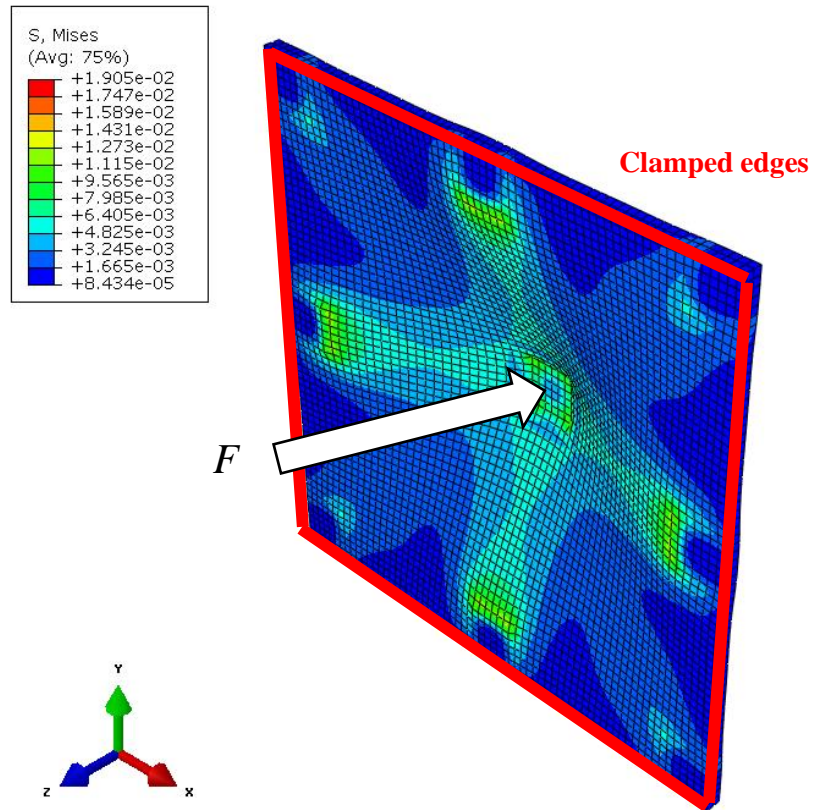
Figure 3.2.6 Boundary and loading conditions of the FEA study. All the four edges are clamped. A pressure load *F* is applied on the surface set 5 which is defined in **Figure 3.2.2**.
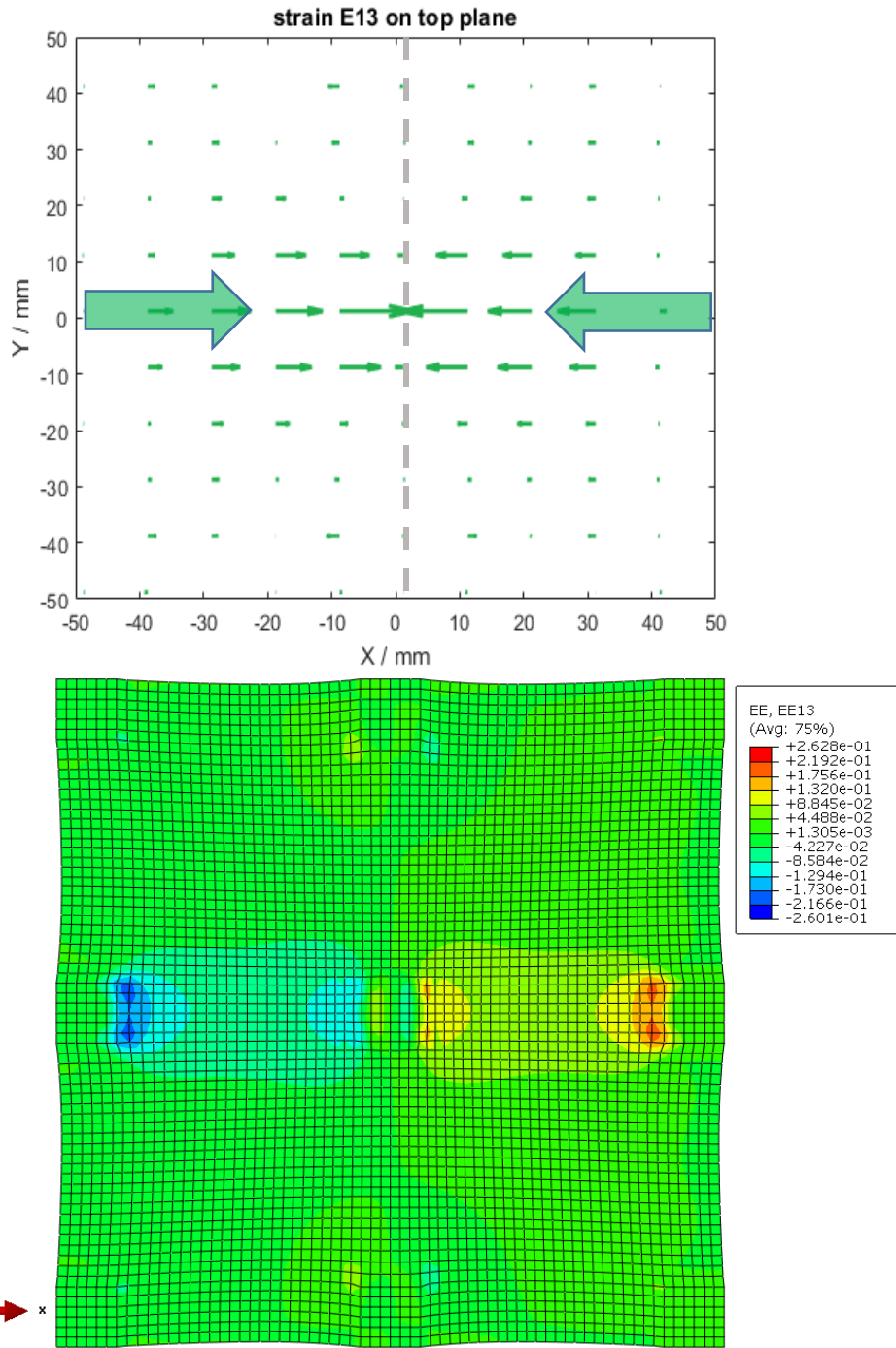
Figure 3.2.7 Strain field (E13) generated from local pushing at the center of the soft sensor. The strain vectors pointed inwards along *x*-direction on the top surface of sensor.
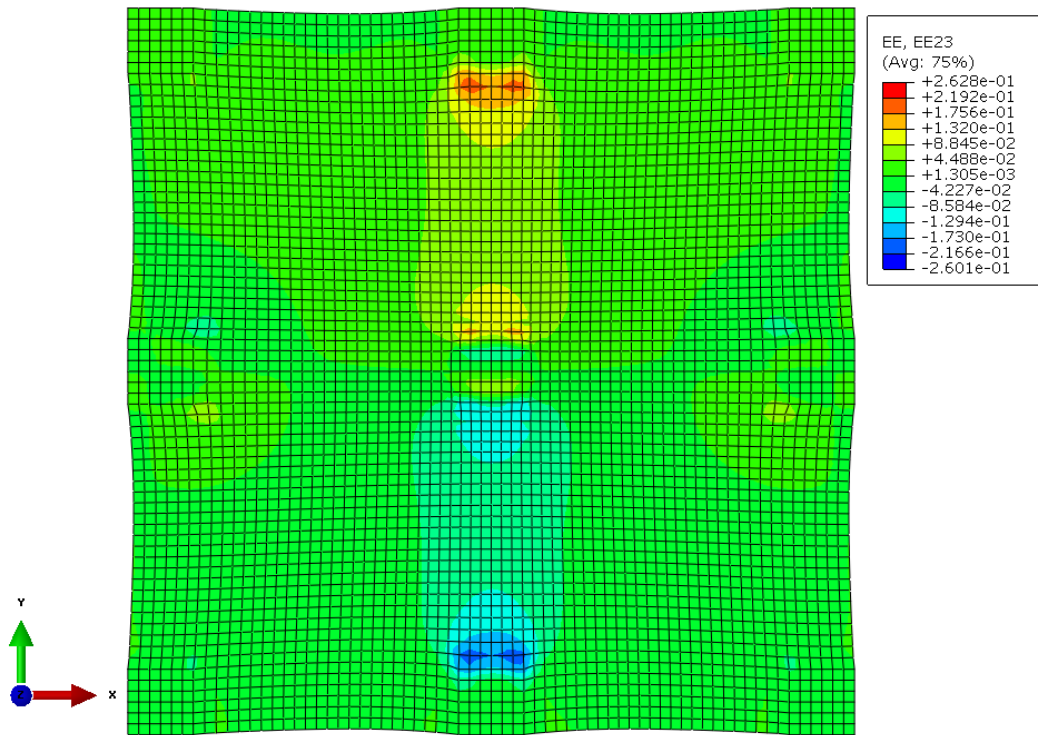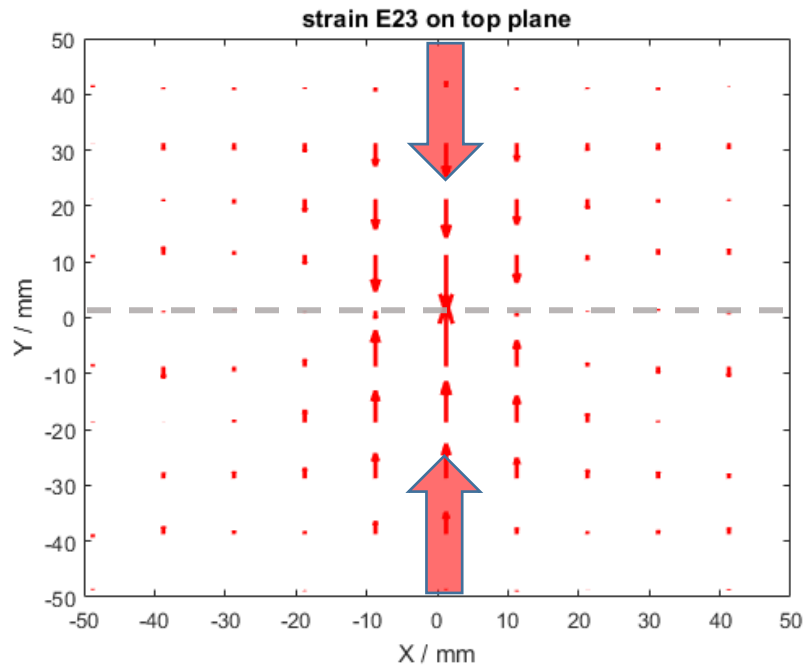
Figure 3.2.8 Strain field (E23) generated from local pushing at the center of the soft sensor. The strain vectors pointed inwards along *y*-direction on the top surface of sensor.

香港大學圖書館 HKU Libraries
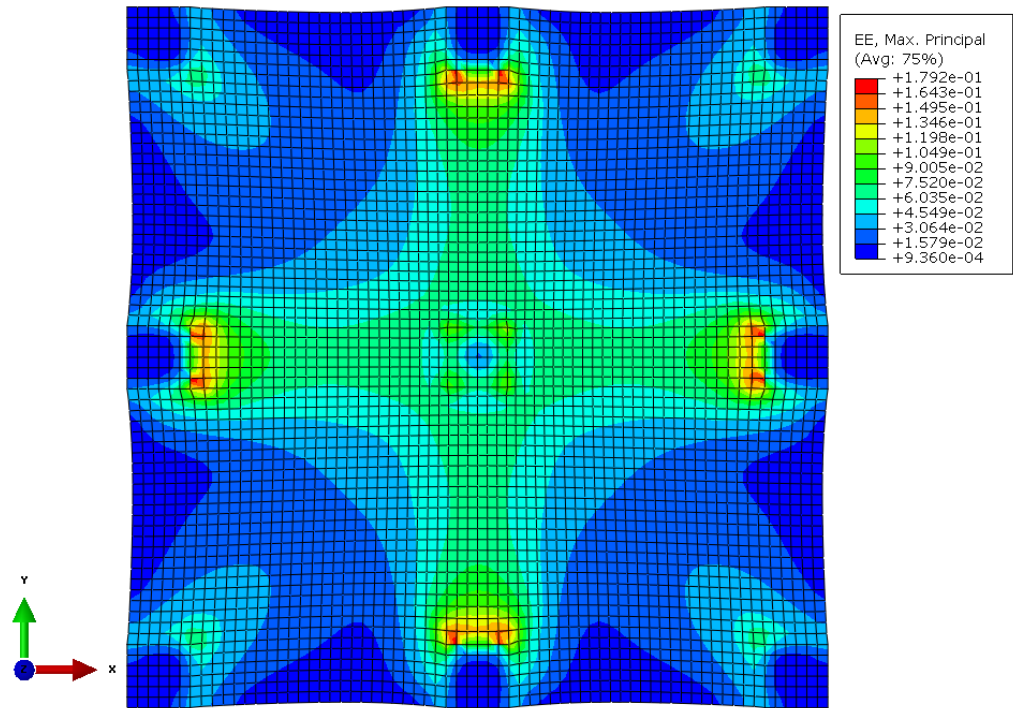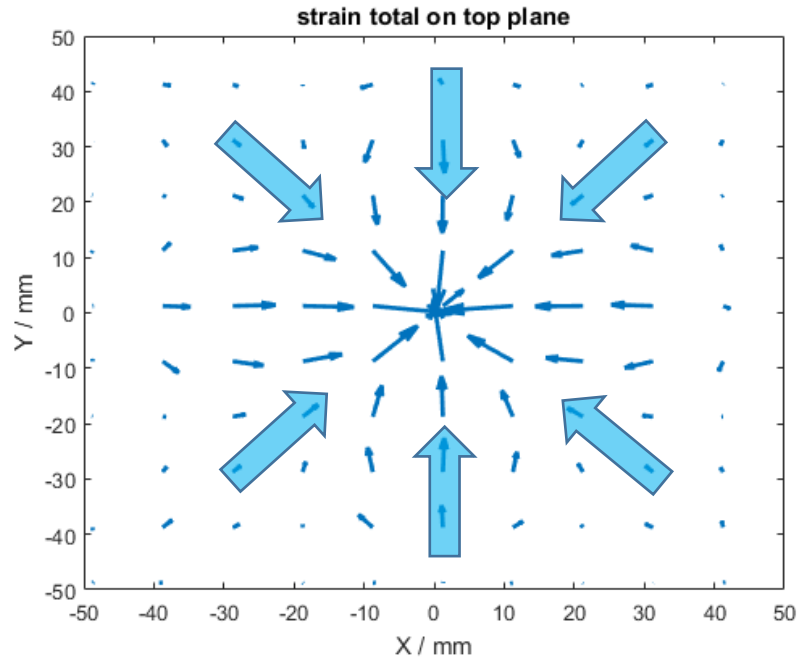
Figure 3.2.9 Resultant strain fields obtained from local pushing at the center of the soft sensor. The strain vectors pointed to the center on the top surface of sensor.

3.2.3. *Clustering of Strain Vectors*

Due to the fiber orientation, only part of the strain component will reflect and sense by the FBG strain sensor. The resultant strain fields obtained from the last section are analyzed with the strain vector directions. By placing FBG sensors along the direction of particular strain vectors, the responses can be maximized. To get those strain vectors, the directions of the strain vectors are first identified as a set of strain angles and grouped as strain regions having similar directions. This is done by using a cardinal direction clustering algorithm:

$$S^* = \operatorname{argmin}_S \sum_{i=1}^{k} \sum_{\theta_j \in S} \left| \theta_j - \varphi_i \right| \tag{3.2.1}$$

where $k \in [1, 8]$, $\varphi_i \in \mathbb{R}$ is the principle cardinal direction, $\theta_j \in \mathbb{R}$ is the strain angle computed from strain field outputs in the cluster set S_i. S^* is a large cluster set containing $S_1 S_2 \ldots S_k$.

The five deformation patterns are then clustered with the above algorithm and group in 8 different cluster groups and shown in **Figure 3.2.10.**

3.2.4. *Fiber Shape and Location Planning*

Sensor placement or the sensor morphology plays an important role in the final sensor sensitivity. [151] considered the optimal placement of strain gauges and accelerometers in structural monitoring problem to estimate loads. In [152], strain analyses are conducted to design two conductive thermoplastic elastomers (CTPE) sensors for twisting and serpentine sensing. Here, clustered resultant strain fields are used to identify potential locations for sensor placement. In **Figure 3.2.10**, major cluster regions are represented with vector showing the direction of strain flow in that region. Strains of small magnitudes and small local cluster group are neglected.
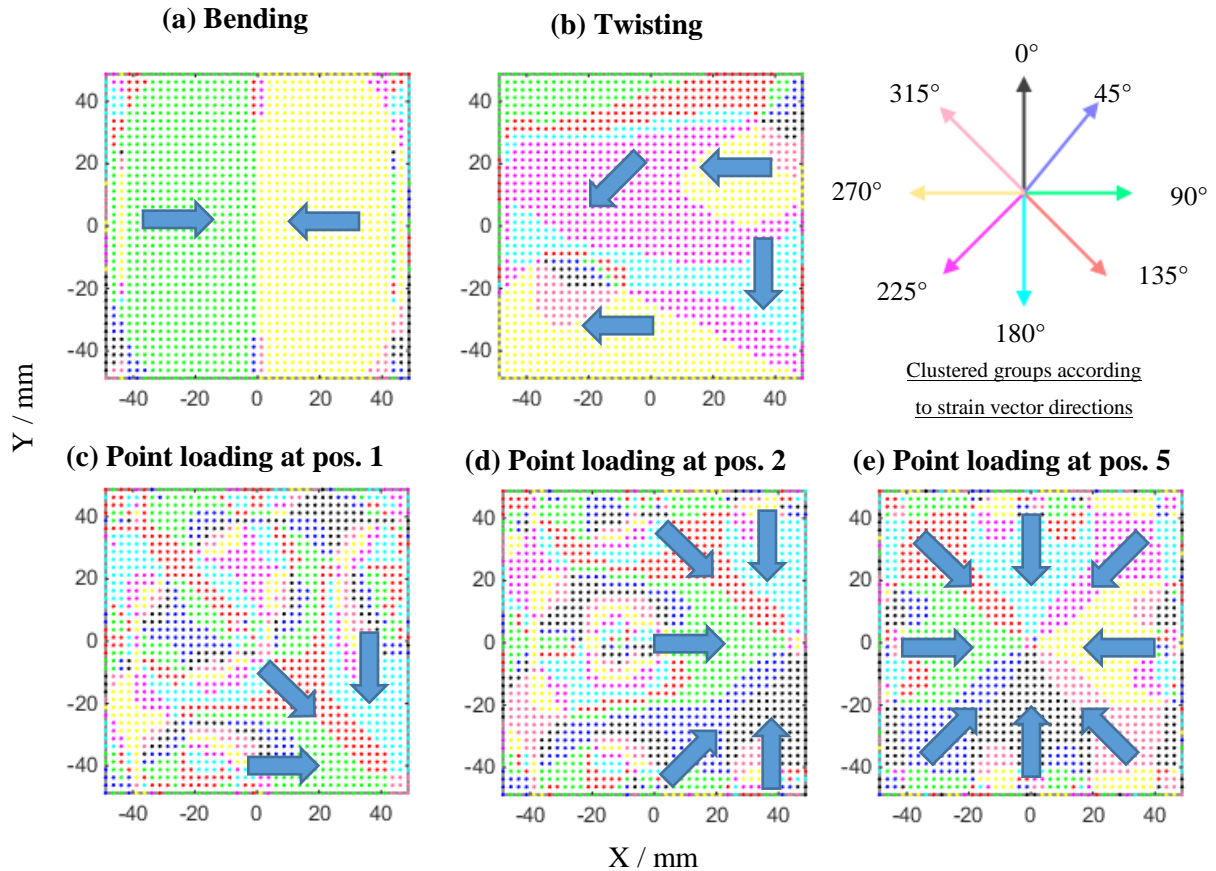
Figure 3.2.10 Strain direction vectors are plotted in clustered regions, each color represents a clustered cardinal direction group. The sensor is deformed by **(a)** bending, **(b)** twisting and point loading at **(c)** surface set 1, **(d)** set 2 and **(e)** set 5, where the surface sets are defined in **Figure 3.2.2**. Regions with low magnitudes and small cluster group are neglected.

The uniqueness of local strain pattern is also considered. Although the strain patterns generated from different deformation patterns are unique, local strain fields may be identical or similar to each other. Thus the uniqueness of local strain fields is computed by finding the difference between two deformation patterns. The resultant strain field from the difference between bending and twisting patterns are shown in **Figure 3.2.11**. The uniqueness of the two deformation patterns can be visualized as regions with strain vectors of high magnitude and the regions with strain vectors close to zero indicated the commonalities of these two patterns. Sensors should be placed outside the common regions in order to minimize the sensing cost and placed to uncommon regions to maximize the pattern discrimination accuracy.
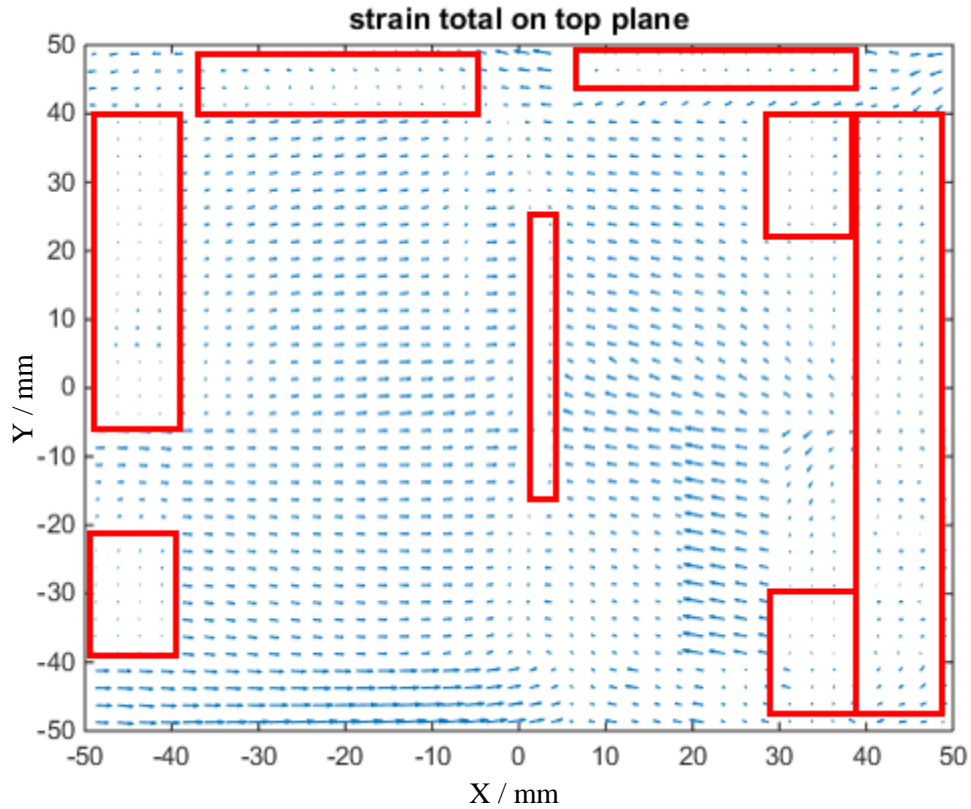
Figure 3.2.11 Resultant strain fields from the difference between bending and twisting of the sensor. The strains at the boundary have similar direction and magnitude in both deformation modes. FBGs should be placed outside of the red regions to ensure uniqueness of the measurement.

Considering the local strain pattern uniqueness of the deformation patterns, three fiber configurations are proposed and shown in **Figure 3.2.12**. The sensor placement locations are bounded 10 mm from the boundaries after analyzing the local strain field uniqueness. These fiber configurations are designed with a single fiber to minimize the cost and fabrication effort.
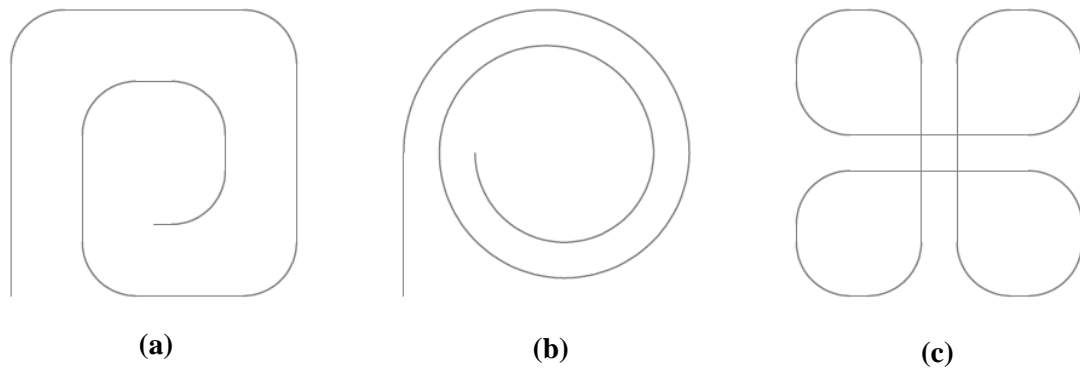
Figure 3.2.12 Proposed fiber shape: **(a)** square spiral, **(b)** spiral and **(c)** butterfly shape. The initial size of silicone substrate is a square with a side length of 100 mm.

Sensor responses are obtained from finite element simulations. The sensor fiber is first modeled in Abaqus, meshed into truss elements and tied onto the sensor surface. Each element is defined at a global seed size of 5, which is the actual grating size. The sensor fibers are modeled as 86, 91 and 104 truss elements for the shapes of square, spiral and butterfly accordingly. The fiber responses are measured as axial strain components E11 of each element and the strains are plotted along the elements in **Figure 3.2.13** - **Figure 3.2.15**.

(a) Bending

Fiber position from lead-in / 5 mm

(b) Twisting

Fiber position from lead-in / 5 mm

(c) Point Loading

Fiber position from lead-in / 5 mm
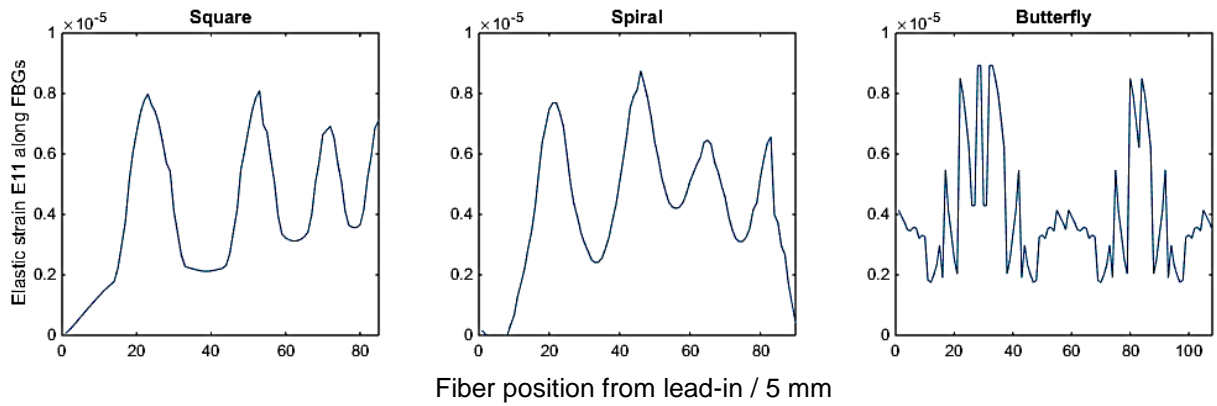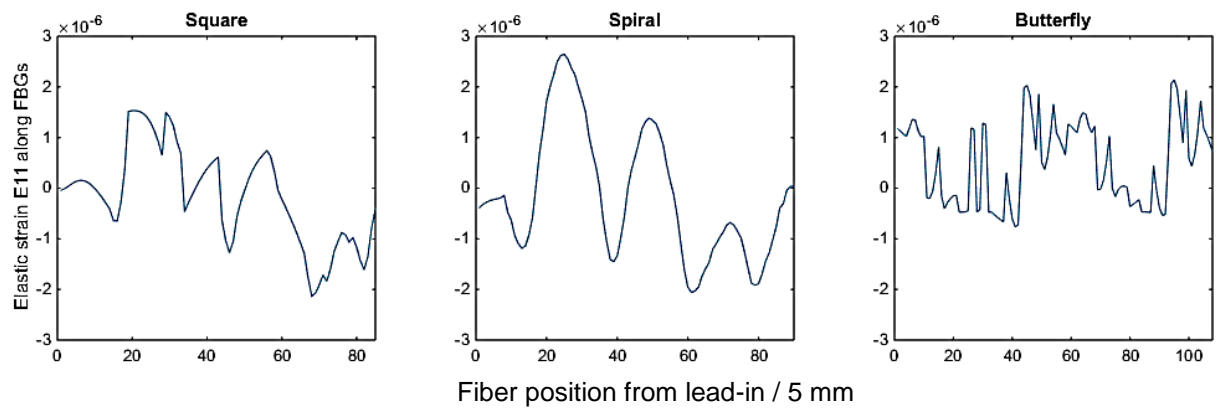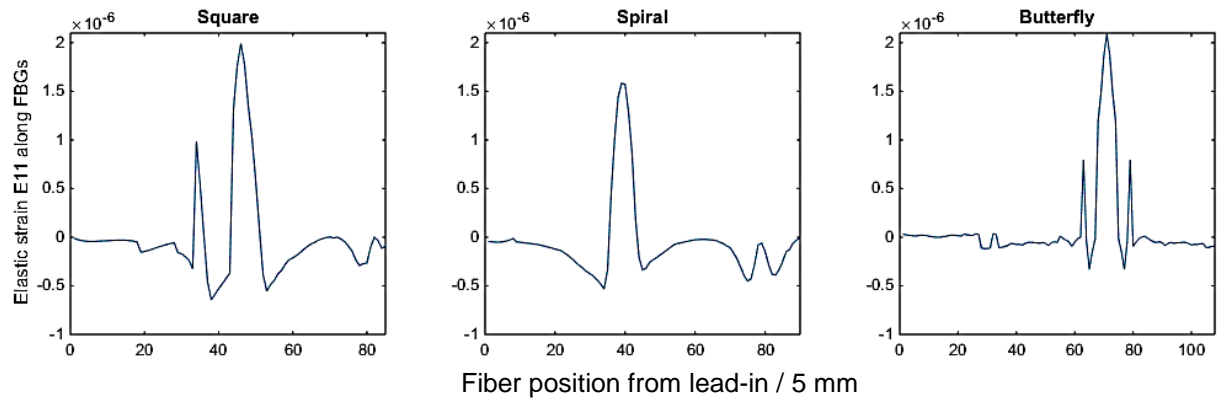
Figure 3.2.13 Fiber strain responses due to **(a)** bending, **(b)** twisting and **(c)** point loading at a corner. Similar sensitivities are observed for all fiber configurations.
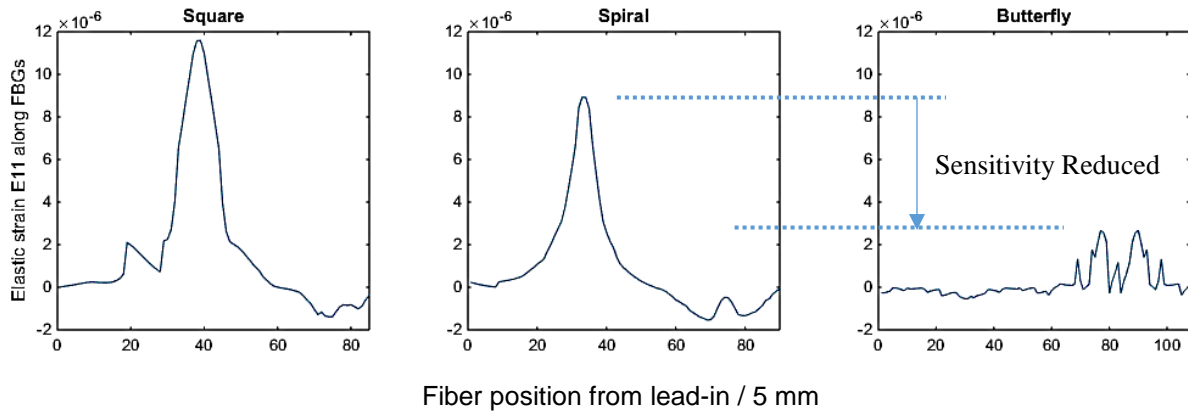
Figure 3.2.14 Fiber strain responses due to a point load at the mid-point of an edge. The butterfly design has low sensitivity as the mid-point of the edges are not constrained by fibers.
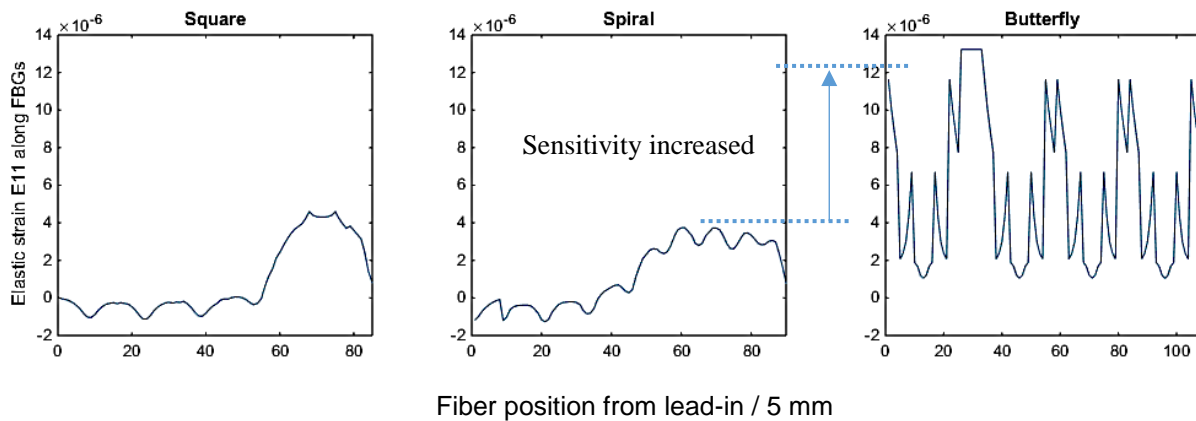
Figure 3.2.15 Fiber strain responses due to a point load on the center of the sensor. The butterfly design has a high sensitivity as a large number of gratings are concentrated at the center.

The above figures showed the strain patterns captured by the sensor fiber and uniqueness of the three deformation patterns. The simulated results showed a similar performance in sensing bending and twisting patterns. The strains measured at those elements showed comparable axial strains, i.e. 8e-6 and 2e-6 at bending and twisting respectively. However, the third design is insensitive to local pushing at the midpoint of the boundary. Also, the implementation of the fiber sensor onto the soft

silicone plate is difficult since there are overlapping of the fiber. This makes design 3 unfavorable as this work aimed to present a simple sensing architecture with the lowest implementation cost. Design 2 is chosen at the end as less stress concentration than design 1 and further simplified into the circular structure as shown in **Figure 3.2.16**.

(a)   **(b)**
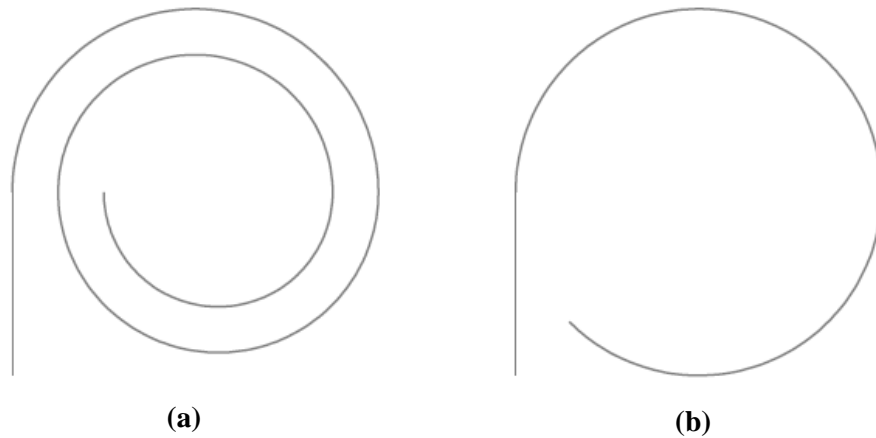
Figure 3.2.16 Selected design in **(a)** spiral and **(b)** the simplified shape. The diameter of simplified design 2 is Ø 80 mm.

Sensor responses of design 2 and the simplified version are compared and shown in **Figure 3.2.18**. The simplified design showed a promising result in identifying bending, twisting and pushing patterns. The only disadvantage compared to design 2 is the lower sensitivity to local pushing at the center of the soft sensor. Only 53 elements are used in the simplified fiber model comparing to 86 elements used in the original design. The length of the sensor fiber required is reduced by ~ 40%.
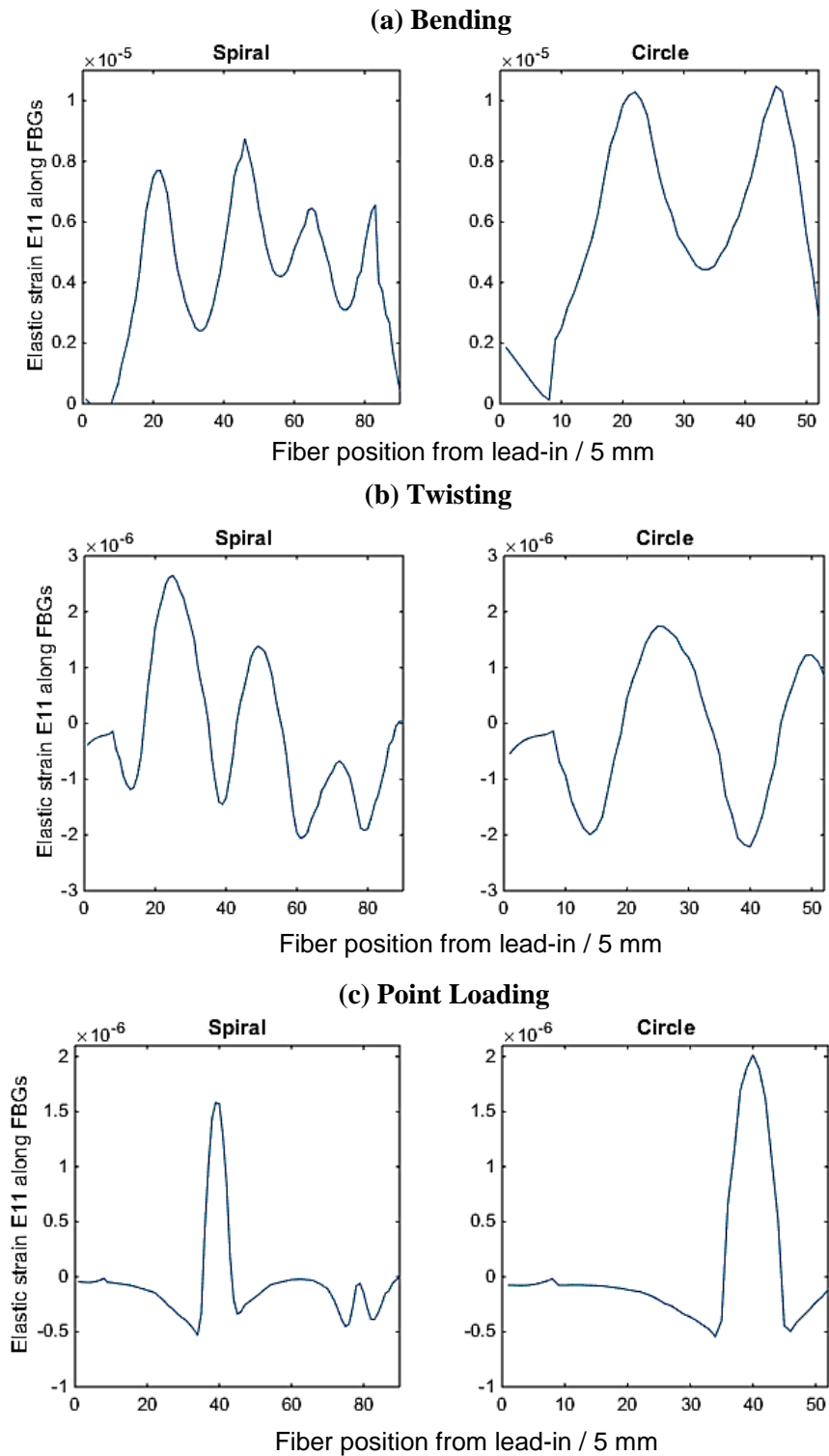
Figure 3.2.17 Strain response of different fiber configurations: spiral (Left) and simplified design (Right) under **(a)** bending, **(b)** twisting and **(c)** point loading on the corner. Similar sensing sensitivities are observed in both fiber configuration.
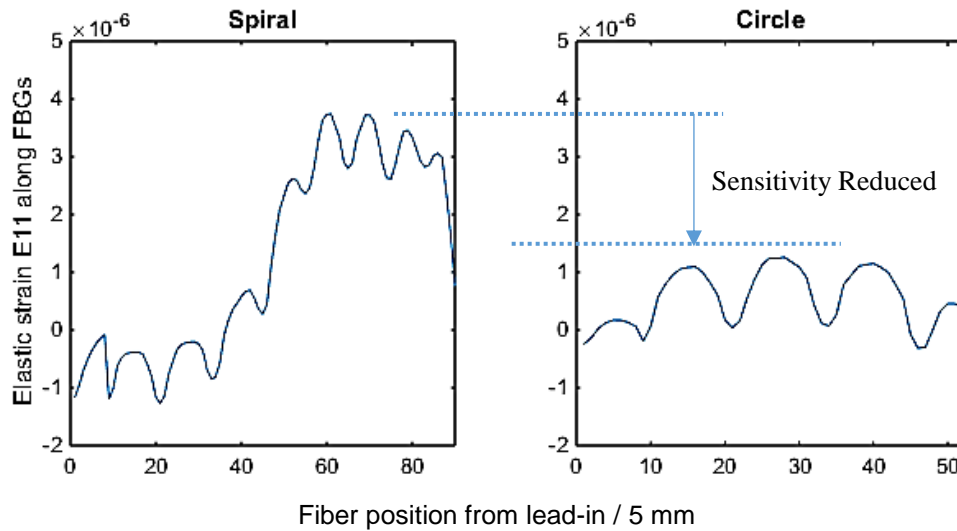
Figure 3.2.18 Strain response of different fiber configurations: spiral (Left) and simplified design (Right) under a concentrated load on the center of the sensor. The simplified design demonstrated a lower sensitivity but still comparable to the averaged sensitivity of the spiral configuration.

The above analysis is based on single layer FBGs. However, single layer FBGs cannot reconstruct the shape correctly under stretching or compression loads along the surface normal since FBGs are also sensitive to pressure. Note that unlike conventional plate definition, the silicone plate varies its thickness during deformation and the strains along the thickness are no longer zero and negligible. For practical surface shape sensing on soft robots, multiple layers of FBGs are required. With multiple layers of FBGs, stress and strain distributions can be captured and reconstructed for the internal layers of the sensor. To include the effect of in-plane loadings, the final circular design is extended to dual layer FBG design, as shown in **Figure 3.2.19**. The number of layers is selected as two due to the sensor thickness. Thinner the sensor, smaller variations between the FBG layers thus a higher number of layers are not required. Typically, two layers are enough as the sensor is designed to be soft and flexible. Thicker sensors will hinder the original movements of the soft robots. The final size of the sensor is also reduced to 45 mm × 45 mm to coop with smaller surfaces which can be easily scaled up by increasing the number of FBGs and fiber length.
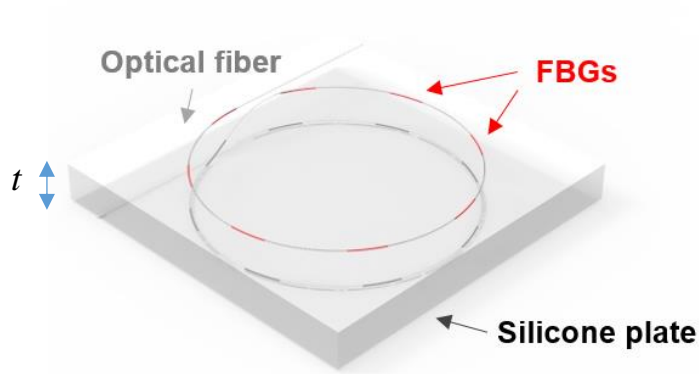
Figure 3.2.19 Overall sensor structure: **(i)** top thin silicone protection layer, **(ii)** first FBG layer, **(iii)** silicone plate, **(iv)** second FBG layer, **(v)** bottom thin silicone protection layer. Silicone layers are made by Smooth-On Ecoflex-0030 using injection molding and a high-strength optical fiber is coiled as two FBG layers. Gratings are written on a custom-made low bend loss fiber (FBGS LBL-1550-125, DTG®s) with 17 draw tower gratings as strain and temperature sensors. Distance from mid-plane to fiber is defined as *h* and sensor thickness is defined as *t*.

Table 3.2.1 Simulation parameters for our FEA study.

FBG: silica material	
• Young's Modulus	70 GPa
• Poisson's Ratio	0.16
• Cross-section Area	0.0298648 mm^2
• Element Type	2-node linear 3-D truss, hybrid.
Silicone substrate	
• Hyperelastic, Ogden model	
○ μ_1	0.024361
○ μ_2	6.6703×10^{-5}
○ μ_3	0.00045381
○ α_1	1.7138
○ α_2	7.0679
○ α_3	-3.3659
○ D_1	3.2587
○ D_2, D_3	0
• Element Type	8-node linear brick, reduced integration, hourglass control.
Loading Cylinder: Steel	
• Young's Modulus	209 GPa
• Poisson's Ratio	0.3
• Element Type	8-node linear brick, reduced integration, hourglass control.
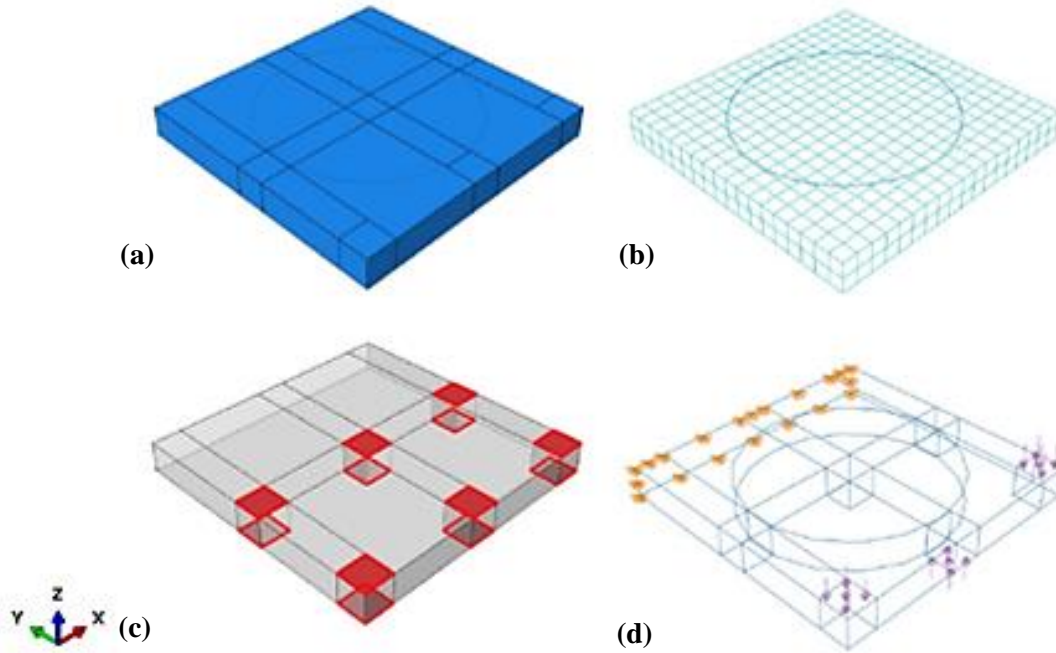
Figure 3.2.20 Finite element modeling workflow for the two-layer model. **(a)** Part model and assembly: Silicone plate and optical fiber are built with desired dimensions. Silicone protection layers are neglected due to the low thickness. Fiber model is tied on the surface of silicone plate model with surface-to-node region constraint. **(b)** Meshing: The silicone plate model (45 mm × 45 mm × 5 mm) is meshed to 5184 C3D8RH elements (36 × 36 × 4) and the sensor fiber is meshed to 44 T3D2H elements which are 2-node linear 3D trusses that only allow axial strains. **(c)** Loading and surface set definition: 12 surface sets are predefined to apply random pressure loadings for simulating external forces acting on the sensor surfaces following the nodal rotations. **(d)** Boundary conditions: one side of the sensor is in clamped condition while others are free ends.

3.3. Sensor Sensitivity Analysis

In the previous section, sensor morphology is briefly discussed and a final circular sensor fiber shape is adopted. As strains captured from the FBG strain sensor also varies with different parameters and eventually affect the sensor performance, various parameters relating to the sensor structure and materials are discussed in below sections. To select proper design parameters for sensor thickness t and fiber offset h, parametric studies are conducted to evaluate the sensor performances with different sensor designs. The estimated and predicted the sensor responses of

the designed shape sensor are computed from a commercial finite element analysis software, Abaqus 6.14. Finite element analysis is adopted in our analysis due to its high adaptability in computing sensor responses with various sensor geometry. In this research, two selected parameters are studied.

The workflow to analyze sensor parameters is shown in Fig. 3. Part models are firstly built with designed dimensions. The silicone sensor base and the sensor fiber are modeled as 3D deformable models. The protection layers are not included in the simplified model which has a negligible effect on overall sensor rigidity. The materials are then assigned to the models. For silicone rubber, it is modeled as a hyperelastic material using Ogden strain energy potential. Parameters of the 3-term Ogden model are adopted from literature [150] and listed in **Table 3.2.1**. Take note that the use of FE simulation in this work is to figure out wavelength shift patterns, but not the actual sensor measurements which require precise and accurate material and mechanical parameters.

To model the mechanical behavior of the fiber material, a linear elastic model is used with Young's modulus of 70GPa and Poisson's ratio of 0.16. The final sensor base is meshed to 648 C3D8RH elements ($18 \times 18 \times 2$) and the sensor fiber is meshed to 44 T3D2H elements which are 2-node linear 3D truss that only transfer axial strains. The fiber part is tied to the desired sensor base surface with node region-to-surface constraint. To simulate sensor response under different loading conditions, one side of the sensor is set as a clamped condition while others are unbounded as free ends. All the simulations are done under static loading steps. To generate deformations such as bending and twisting patterns, surface loads are applied on twelve surfaces which marked in red in **Figure 3.2.3**.

3.3.1. *Fiber Offset Distance*

According to the bending theory, strains along the neutral plane are the same when the sensor is subjected to positive and negative bending moment if the fiber sensor is located at the neutral position. Thus, sensor fiber has to be offset from the midplane of the sensor substrate in order to identify the direction of bending with a minimal number of sensor fibers embedded. In this simulation study, the sensor body is discretized and meshed with an element size of 1.25. The sensor is then subjected to positive and negative bending moment resulting in a bending radius of 40 mm and the sensor responses are shown in **Figure 3.3.2**.

The first parameter studied is the effect of fiber offset distance h where the thickness t is arbitrary set as 5 mm. The thickness t will further discuss in the second part of the analysis. Considering the bending theory, strains along the neutral plane are the same when the sensor is subjected to a positive or a negative bending moment. This indicates the FBGs must offset from the neutral plane to identify the direction of bending. A simulation study is done by applying a three-point bending on the sensor. In **Figure 3.3.2**, sensor responses are obtained when the sensor is placed on two supporting pins and subjected to a loading F by displacing a cylinder where the radius is 20 mm. The x and y displacements of the cylinder are restricted and only movable along the z-direction. At $step = 1.0$, the sensor is bent to the same radius. This simulated a typical deformation pattern that bending is created by pushing. When the fiber offset from mid-plane $h = 0$ mm, the simulated strains are slightly positive due to the in-plane stresses induced by pushing. For pure bending, the sensor will have approximately zero strain readings when pre-strain is not considered. At $h = +0.25t = +1.25mm$, a significant rise in strain magnitude is observed. At $h = -0.25t = -1.25mm$, simulated strains shifted to negative region due to compression. At $h = \pm 0.5t = \pm 2.5mm$, a further increase in strains is observed. However, the gain in compression strain sensitivity is much lower. Noting that when the fiber is in compression, it may buckle. Thus, the deformed fiber will experience lower stresses in magnitude comparing to tension load. To maximize the strain magnitude for better strain pattern discrimination, the highest offset value is selected, i.e. $h = \pm 0.5t = \pm 2.5mm$.
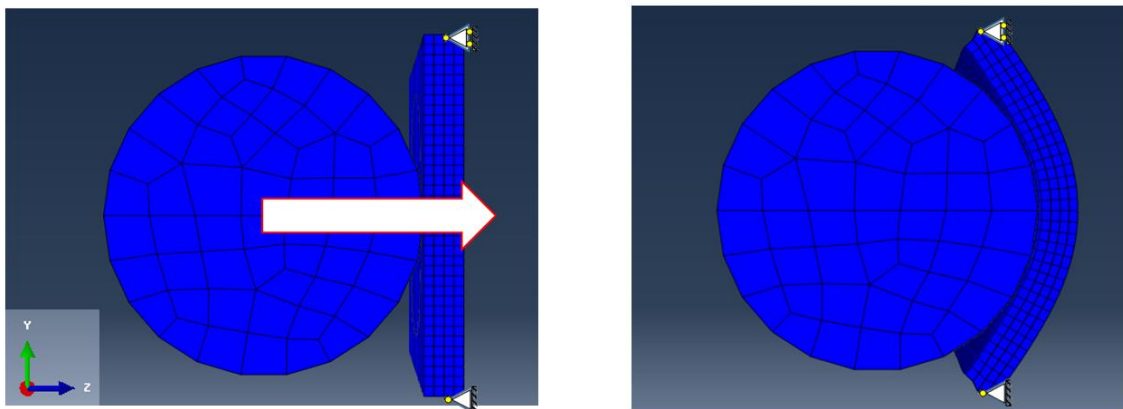
Figure 3.3.1 Three-point bending simulation settings. At the mid-plane of the sensor, one edge is pinned and the opposite edge is set as a roller support. A rigid cylinder is applied onto the top surface to generate bending deformation.
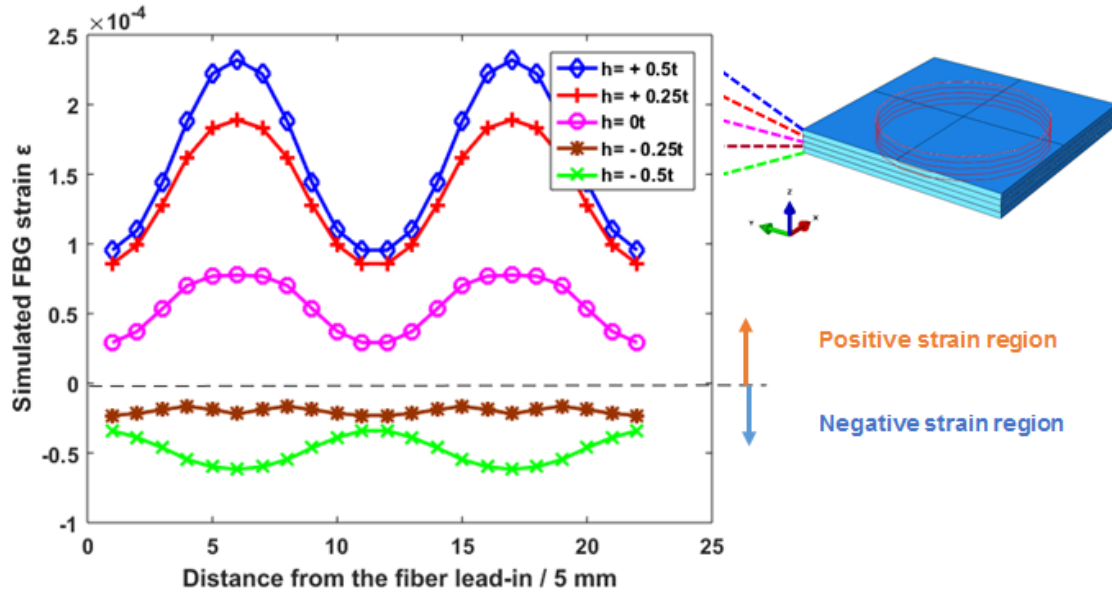
Figure 3.3.2 Simulated strain responses of our sensor at five offset distance h under 3-point bending. Each simplified fiber ring model measures the strains in the corresponding plane, e.g. at $h = 0$, the fiber is embedded in the mid-plane. Magnitudes of the negative strains caused by compression loads are small. Thus strains at small h is less favorable. Note that the neutral plane is not necessarily the same as the mid-plane.

3.3.2.   *Sensor Thickness*

The second analysis is conducted to study the thickness t of the sensor base. For the soft and flexible sensor, the low thickness would be an advantage when integrating the sensor on actuators and other components for flexibility. However, a single core fiber is used in this work, the fiber needs to offset from the mid-plane and with a suitable thickness to discriminate deformation patterns. The thickness t is determined by considering the strain patterns with varying thickness (2.5 – 7.5 mm). The range is selected by considering the overall sensor thickness that is high enough and will not inhibit flexible motions. In the first analysis, we concluded the sensor fiber should attach to the surfaces of the sensor to acquire maximum strain responses. In **Figure 3.3.3**, the strain responses of our proposed sensor structure are simulated under the same bending as **Figure 3.3.1**. When the sensor base thickness t is close to ten times of sensor fiber diameter, i.e. $t = 2.5mm$, the compression strain responses are not significant to identify shape patterns due to the overlapping and may be altered by sensor noise. By increasing the sensor thickness, the output responses also increase and become noticeable. At $t = 7.5mm$, the sensor responses are maximized. However,

several compressive strains started to saturate. Further deformations may induce unfavorable compressive stress and lead to instability, buckling of the fiber and eventually break the fiber inside the silicone plate. After comparing the sensor responses with more deformation modes, 5 mm is selected as the sensor thickness of our primary shape sensor to yield distinct strain patterns while providing high flexibility.

Note that the strain response is low when the sensor is too thin while the strain response is high and noticeable when the sensor is thick. This result indicated the sensor thickness has to be thick enough to allow measurable deformation patterns. However, if the sensor is too thick, it may constrain the original movements of the soft robots. Depending on the robot design and sensing requirement, the sensor thickness can be adjusted for optimal performance.
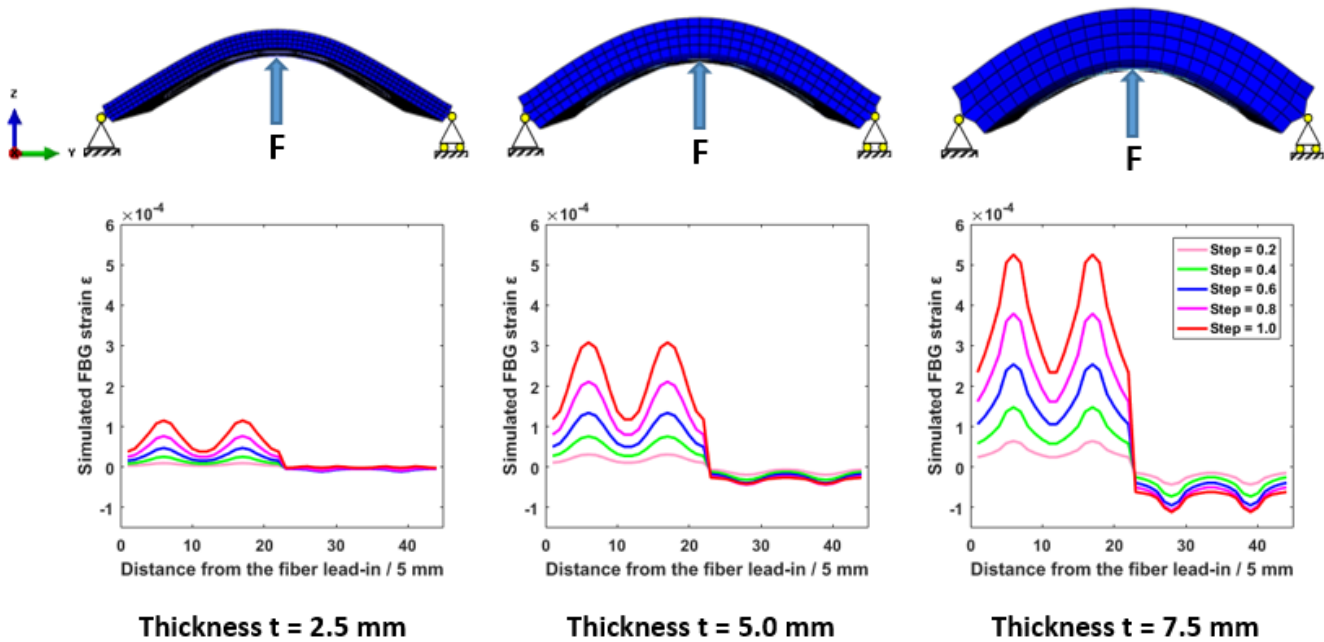
Figure 3.3.3 Simulated strain responses of our sensor at three different thicknesses under three-point bending where offset $h = \pm 0.5t$. The magnitude of strains varied proportionally to the sensor thickness. At thickness $t = 2.5mm$, strains due to compressive loadings are overlapped. At thickness $t = 5mm$, negative strains can be clearly identified and used to discriminate deformations. At thickness $t = 7.5mm$, the sensitivity is further increased with several acute points, however, this also leads to a higher possibility of instability, fiber buckling, and less flexibility.

3.3.3.   *Fiber Material Stiffness*

The third element is the fiber stiffness, which affects the minimum bending radius and maximum strain sensible. The simulation environment, physical and material variables are same as **Figure 3.3.1**, where the sensor is under bending condition.

Consider the applied stress is lower than the ultimate tensile stress of the optical fiber, a fiber with lower modulus allows larger strains while higher modulus reduces the fiber strains and limits the motion of the soft robot. Sensor responses are shown in **Figure 3.3.4**. In the above simulations, the elastic modulus E of the optical fiber is set to be 70GPa from the literature. For an elastic modulus is an order above the current, the strain responses are nearly not observable. The strains induced are low and only coarse measurements can be made. Note that small strain variations could not provide enough information for surface recognition, no matter which analytical or data-based solution is applied to. In order to discriminate the deformation patterns, a flexible fiber with low elastic modulus is preferred. At $E = 7$GPa, the maximum strain induced is about 0.01% which is much noticeable and favorable when comparing the strains at $E = 700$GPa. This indicates less stiff fibers such as polymer fibers are favorable in soft sensor design due to higher strains, i.e. high resolution relative to the same measuring device, are available and better adhesion to other substrates.
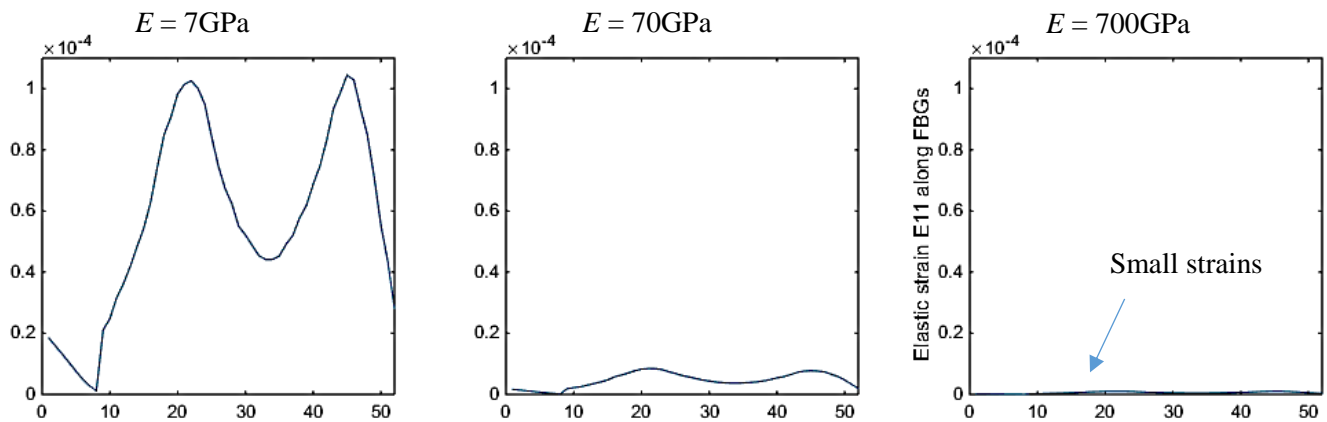
Figure 3.3.4 Strain responses at three fiber stiffness E: $E = 7$GPa, 70GPa and 700GPa. Fibers with lower stiffness can enhance the sensor sensitivity and also reduce the constraining effects on the soft robot body

3.4. Stretchability Analysis

The main difference of surface shape sensing between soft robotics and flexible electronics is the dimension considered in the measurement. Flexible electronics are usually thin and in micron scale, and measuring the effect of single type of loading at a certain time interval only, e.g. pressure, pure bending and pure twisting. In contrast, the surfaces of soft robots are always deformed by different kinds of loading and the combination of those. Thus a multi-layer approach is adopted in the previous section.

In this work, rigid fiber Bragg gratings are used as the sensing element which may hinder the movement of the soft robot, in particular for the high stretching motions. The fiber layout has to be properly designed for better stretchability depending on the applications. In this section, a further study on sensor stretchability is conducted to investigate the effect of fiber configuration on overall sensor elasticity under the different direction of loadings.

(a) **(b)**
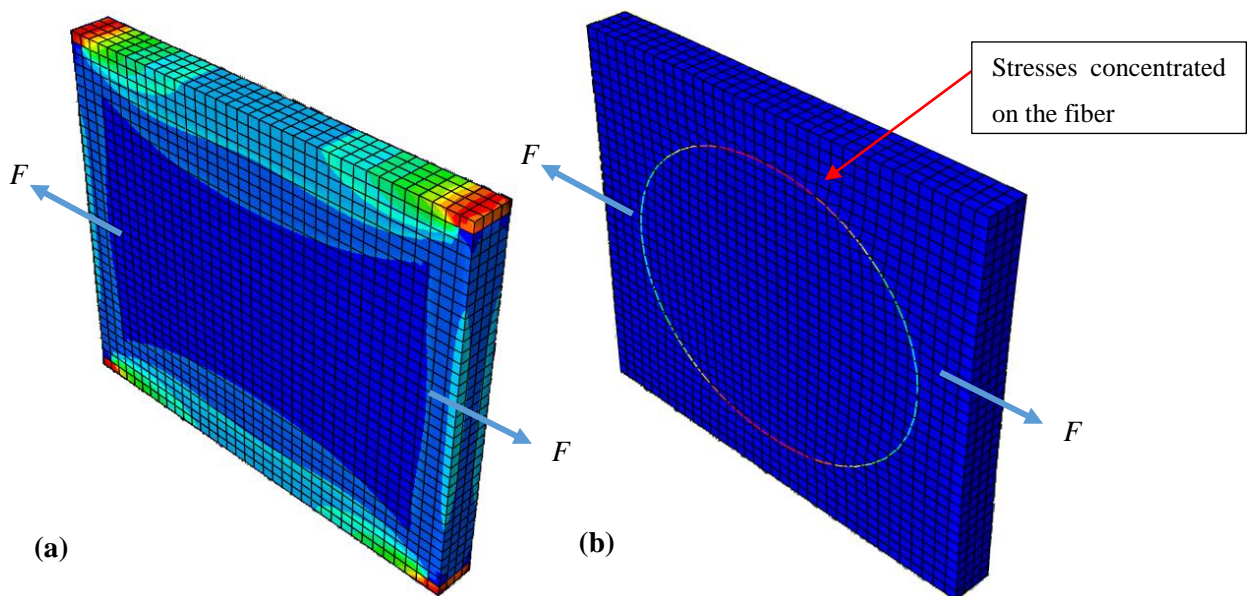
Figure 3.4.1 Effect of fiber embedment to overall sensor rigidity. Stretchability of the overall sensor reduced with fiber embedment. **(a)** With no fiber embedded, stresses spread evenly on the silicone substrate. **(b)** With fiber embedded, stresses are concentrated on the fiber due to an elasticity discontinuity.

3.4.1. Fiber Strength and Buckling Effect

Designing a wavelike structure essentially refers to pre-straining and pre-stressing the fiber even when the sensor under the neutral state, given the sensing elements are fabricated with standard manufacturing processes. To enable soft and flexible characteristics of a sensor, two major factors are considered, i.e. the stiffness and the structural arrangement of sensing elements. For a stiff sensing element, the common approach is to induce wavelike structure on it to enhance its flexibility [153, 154]. For smaller-scale sensing elements, pre-strain can be applied on the substrate before bonding the sensing elements onto the substrate. After releasing the strain, a wavelike structure will be generated with enhanced stretchability [48]. In our case, the optical fiber has relatively high elastic modulus with a large diameter, the first approach is adopted for further analysis.

Note that fiber buckling is the major failure mode of our sensor, rather than the mechanical failure due to poor fiber bonding, substrate adhesion and overstress concentration at the loading point.

In normal operation with optical fibers, the stresses experienced by the optical fibers can be either compressive or tensile. Buckling may occur when the fiber is subjected to compressive stresses. When the fiber buckles, it will become unstable and bend in a sudden to the sideway. Further loading could generate random and significant deformations and eventually cause the failure of the fiber. While fiber strength characterizes the failure stress of the fiber, the failure due to buckling could be much lower than the fiber strength. A destructive experiment has been conducted to evaluate this failure mode. An optical fiber (used in **Section 4.2**) is bonded to a silicone plate (EcoFlex-0030) with a silicone-based adhesive ELASTOSIL® E41 and formed two dummy sensing modules. One module is then tested with the tensile testing machine until it broke. Another one is compressed until the fiber broke. As discussed, the fiber broke due to compression required lower stress than tensile. Once the fiber buckled, it started to deform locally with excess compression stress. This stress further developed and created an acute angle, causing a small bending radius that exceeds the minimum bending radius available. The fiber is then broken as the fiber surface strain is too high. A typical fiber failure sequence due to over-strain is shown in **Figure 3.4.2**.
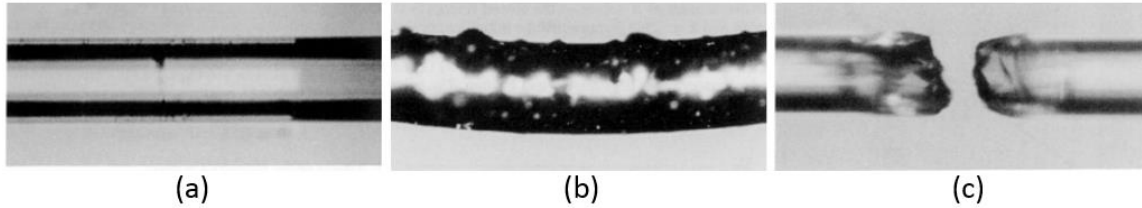
Figure 3.4.2 Mechanical failure of an optical fiber due to buckling from literature [155]. **(a)** Initial state without deformations. **(b)** Compression state: axial loadings are applied from the two ends, first buckling mode is induced. **(c)** Breakage state: compression forces are further increased and the fiber deformed dramatically. Induced surface strains exceeded the strain limit then broke the fiber.

In **Figure 3.4.3**, a simple FEA study is done to visualize how the fiber buckles under compressive loadings. This explains why fiber buckling should be carefully taken into account when designing the fiber structure and for a particular degree of stretchability. Note that the compression on the fiber can also be induced by common bending modes of the sensor.
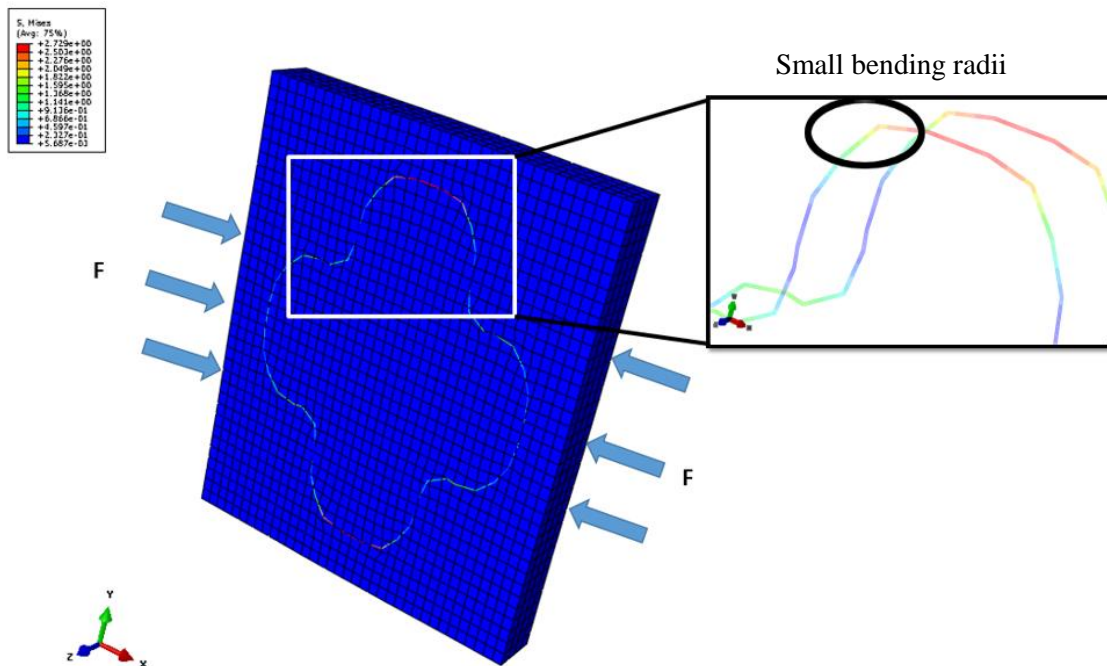
Figure 3.4.3 Fiber buckling in FEA. A compression load $F = 0.01$MPa is applied on two edges of the sensor. Bending radii of the fiber are sharp at several locations which may further develop to fiber failure.

3.4.2. Fiber Routing Configuration

Stretchable sensor routing design for rigid sensing elements has been discussed in depth in [156]. For a typical coplanar wavy or serpentine routing, four parameters are considered, i.e. radius of the arc, arc angle, straight section of routing and width of routing. However, in this work, most of these factors are controlled by the minimum bending radius of the FBG. Considering the sensor dimension in **Section 3.3** as the smallest sensing segment and can be scaled up by repeating the fiber unit, the minimum bending radius of the fiber and the circular pattern angle are the two parameters that being concerned in this work.

The minimum bending radius of the FBG is predefined by the fiber characteristic, e.g. fiber material and diameter. In this work, a fiber with low minimum bending radius (6 mm) is picked in the market. In general, lower outer fiber diameter will lead to a smaller minimum bending radius. The selected high-strength and low-bend-loss fiber has a cladding diameter of 125 µm and coating diameter of 195 µm. Below section will focus on the effect of overall sensor stiffness at different circular pattern angles.

Since the sensor is designed for general application with no bias in sensing direction, the fiber configuration should follow a rotational symmetry in order to retrieve the same degree of sensing responses. This defined the circular pattern angle φ as:

$$\varphi = \frac{360}{number\ of\ repeated\ segments} \tag{3.4.1}$$

Based on the above-mentioned parameters, three fiber routing configurations are designed to study the sensor stretchability at different circular pattern angles. The designs are shown in **Figure 3.4.4**.

(a)   **(b)**   **(c)**
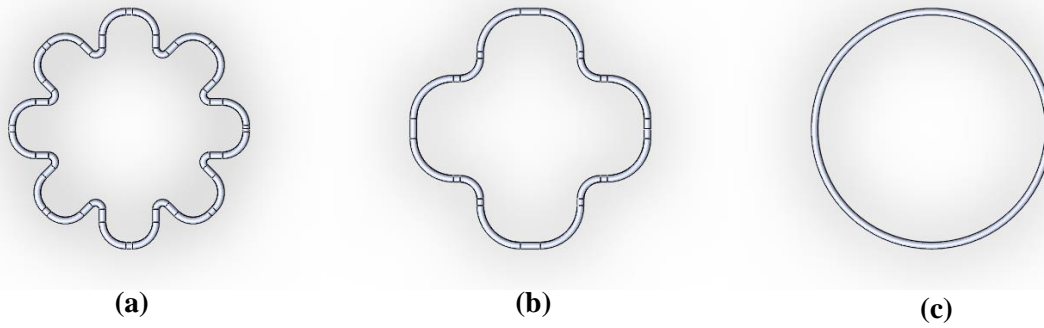
Figure 3.4.4 Fiber routing configurations with three different circular pattern angle φ. **(a)** $\varphi = 45°$: the fiber is shaped with 8 repeating units where the radius of arc is 3.5 mm; **(b)** $\varphi = 90°$: the fiber is shaped with 4 repeating units where the radius of arc is 6 mm; **(c)** $\varphi = 360°$: the circular shape as analyzed in **Section 3.3**.

Three fiber routing configurations are modeled in Abaqus 6.14. The material parameters are the same as **Table 3.2.1**. The only difference is the element size of the FBGs. The selected element size is 1.25 which is half of the size using in **Section 3.3**. This is due to more complex configurations which required more and finer elements for correct representation. One hundred and sixty truss elements are used to represent the configuration where $\varphi = 45°$. One hundred and four truss elements are used to represent the configuration where $\varphi = 90°$. Eighty-eight truss elements are used to represent the configuration where $\varphi = 360°$. All the remaining variables except the geometry of fiber are the same for comparison.

To investigate the variations of sensor stiffness due to the change in geometry difference of fiber shape, i.e. the fiber routing configuration, two stretching tests are simulated. The numerical loadings and boundary conditions are shown in **Figure 3.4.5** and **Figure 3.4.7**.

The first test is stretching along the horizontal axis. Two equal pressure loadings are applied separately at the sides of the sensor. At $\varphi = 360°$, i.e. the circular configuration as determined in **Section 3.3**, the stiffness is the highest among the three fiber routing options. The overall sensor stiffness, or stretchability, decreases with increasing circular pattern angle φ. For higher φ, the elastic modulus of the sensor shifts closer to the elastic modulus of raw silicone plate which refers to a higher sensor stretchability. For the pressure loading $F = 0.02$ MPa, the allowable strain increases up to 144.95% of the original strain at $\varphi = 360°$.

72
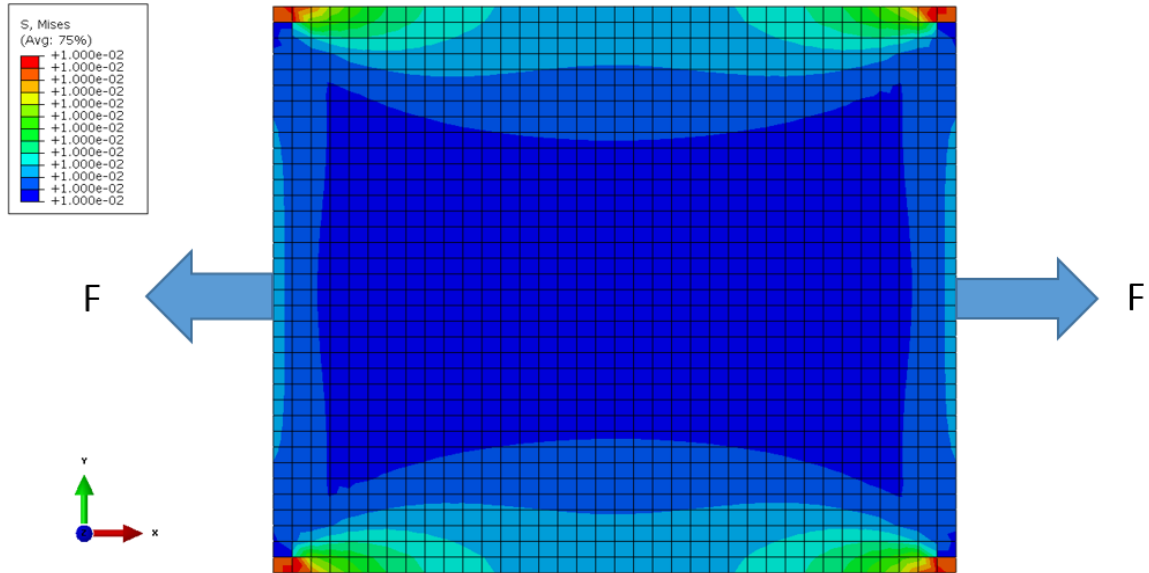
Figure 3.4.5 Tensile testing along the *x*-axis. A ramp pressure loading $F = 0.02$ MPa is applied on edges of the sensor. Mid-plane in *y*-direction is bounded as U2 = UR1 = UR3 = 0. Mid-plane in *x*-direction is bounded as U1 = UR2 = UR3 = 0.
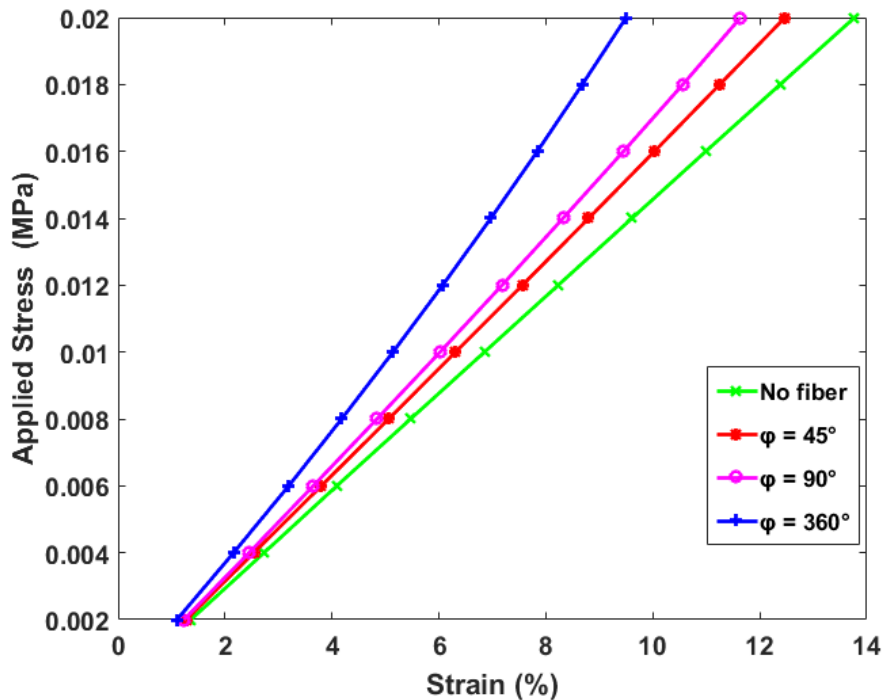
Figure 3.4.6 Changes in apparent elastic modulus along the horizontal. Strains along the horizontal are extracted every 0.1 time step and the loading ramped up to 0.02 MPa at step = 1.0. Without fiber embedment, apparent stiffness was the lowest and increased with the circular pattern angle *φ*.

73

The second test is stretching along the diagonal of the sensor. Two equal traction loadings are applied separately at the corners of the sensor since there is no normal surface to apply loading. At $\varphi = 360°$, i.e. the circular configuration as determined in **Section 3.3**, the stiffness is the highest among the three fiber routing options. The overall sensor stiffness, or stretchability, decreases with increasing circular pattern angle φ. For higher φ, the elastic modulus of the sensor shifts closer to the elastic modulus of raw silicone plate which refers to a higher sensor stretchability, similar to the case of the horizontal tensile test. For the pressure loading F = 0.01 MPa, the allowable strain increases up to 103.96% of the original strain at $\varphi = 360°$. The reduction in elastic modulus is much lower than the case in **Figure 3.4.5** as a smaller loading is applied to the sensor corners to avoid excessive element distortions. Better simulation results can be obtained by refining element size, modify the way to apply loadings and boundary conditions.
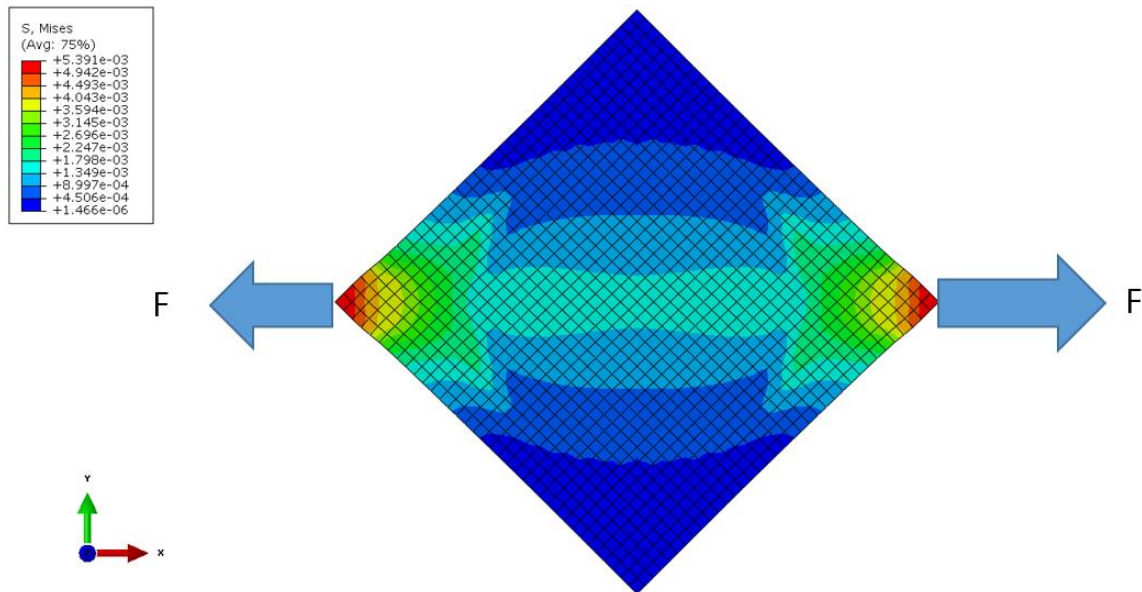
Figure 3.4.7 Tensile testing along the diagonal. A ramp traction loading $F = 0.01$ MPa is applied on two corners of the sensor. Mid-plane in z-direction is bound as U3 = UR1 = UR2 = 0. Unlike the tensile testing in **Figure 3.4.5**, testing along the diagonal required concentrated loadings on specific elements thus was easy to cause element distortions.
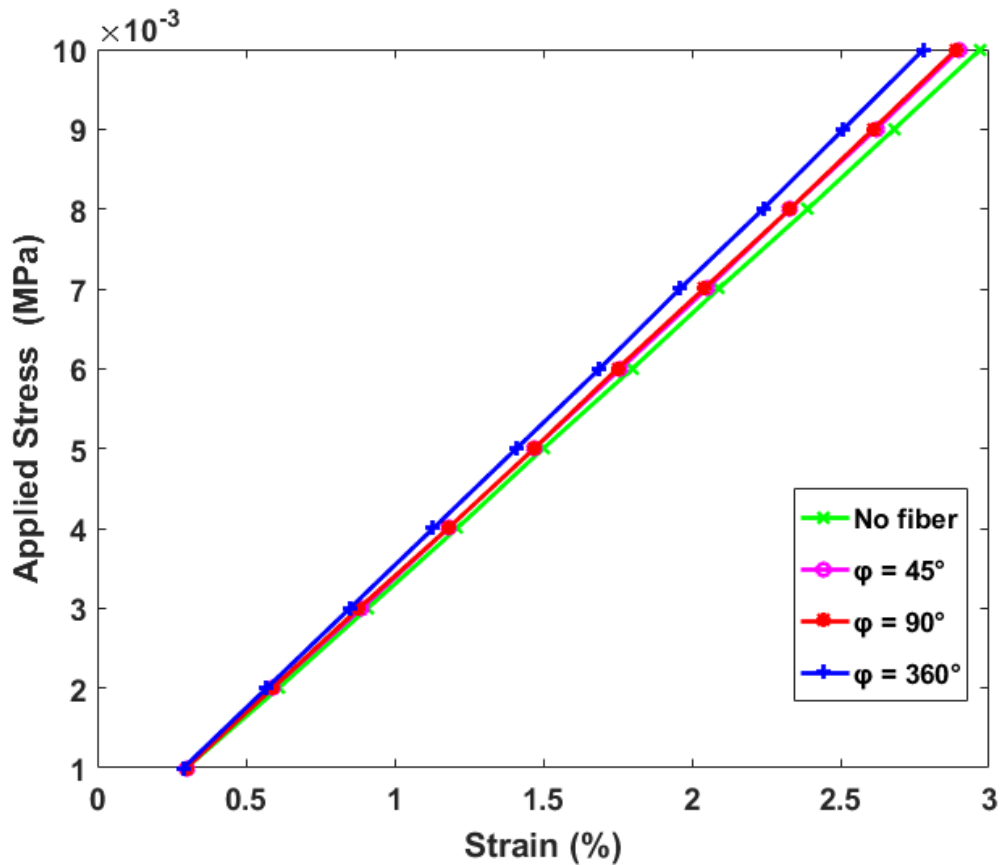
Figure 3.4.8 Changes in apparent elastic modulus along the diagonal. Strains along the horizontal are extracted every 0.1 time step and the loading ramped up to 0.01 MPa at step = 1.0. Without fiber embedment, apparent stiffness was the lowest and increased with the circular pattern angle φ. The difference is smaller comparing to **Figure 3.4.6** since the applied loading is smaller.

The simulated strains in the above tests are extracted for further analysis in **Figure 3.4.9** and **Figure 3.4.10**. It is worth mentioning that the repeat in sensing signal is due to the rotational symmetry nature of the fiber routing configurations and simple stretching loadings. In actual applications that include bending, twisting, stretching and the combination of them, the strain patterns are not necessary to be periodic. Magnitude order of the simulated strains for $\varphi = 45°$ and $90°$ are the same while the strain for $\varphi = 360°$ doubles the other fiber routing configurations. Note that for smaller circular pattern angle φ, more number of wavy sections are available for stress and strain distribution, thus with lower stress and strain concentration. This supports our initial hypothesis in this section that wavy design could enhance reliability and provide a higher stretchable range of the sensor.

(a) $\varphi = 45°$　　**(b)** $\varphi = 90°$　　**(c)** $\varphi = 360°$

Small strain variations

Distance from fiber lead in / 2.5 mm

Strain-relaxed region

S.Mises

Strain E11
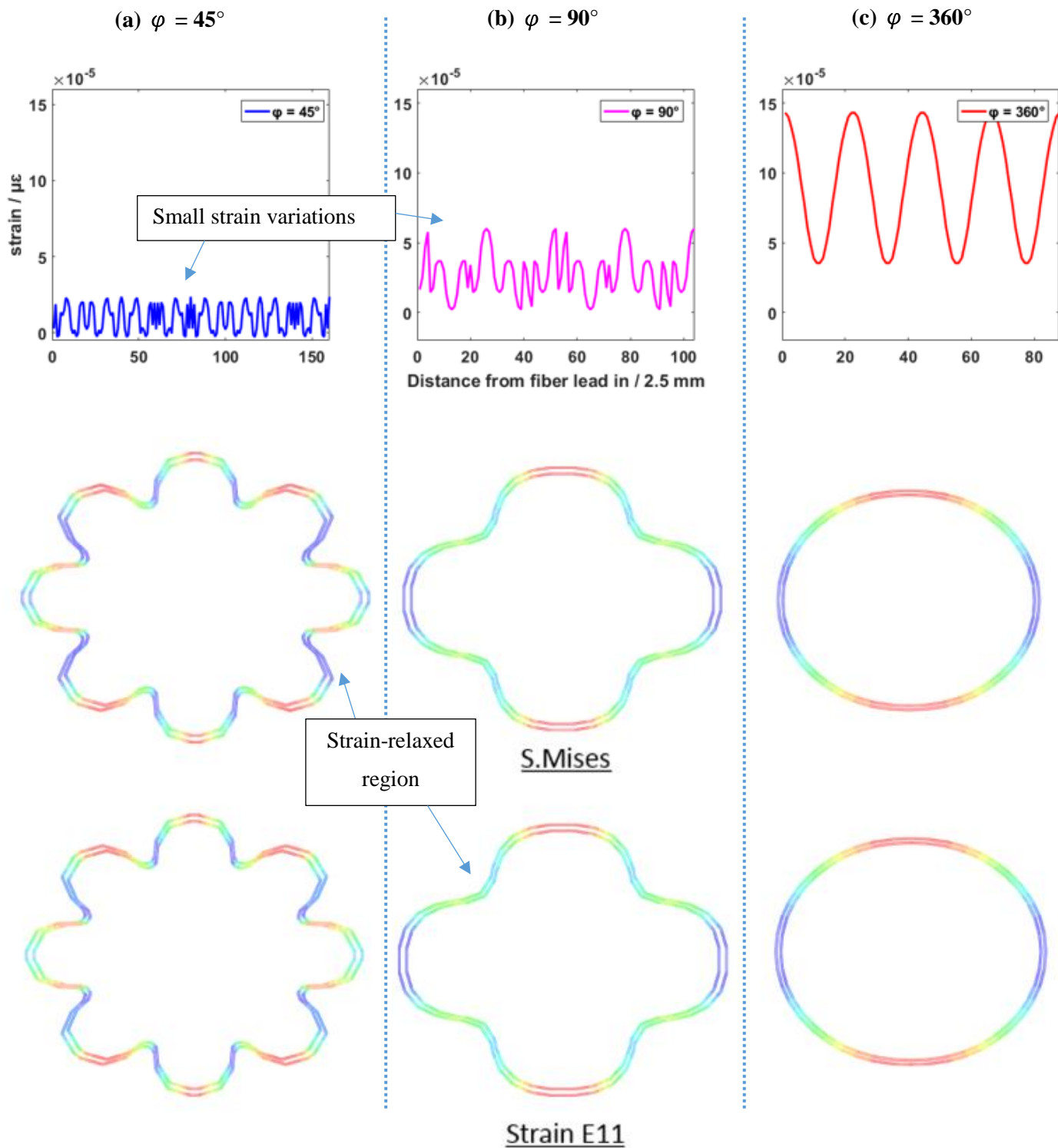
Figure 3.4.9 Simulated strain responses from tensile testing along the *x*-axis. Lowest strain range is found at $\varphi = 45$ and the range gradually increases with φ.

(a) $\varphi = 45°$ **(b)** $\varphi = 90°$ **(c)** $\varphi = 360°$

Strain-relaxed region

S.Mises

Strain E11
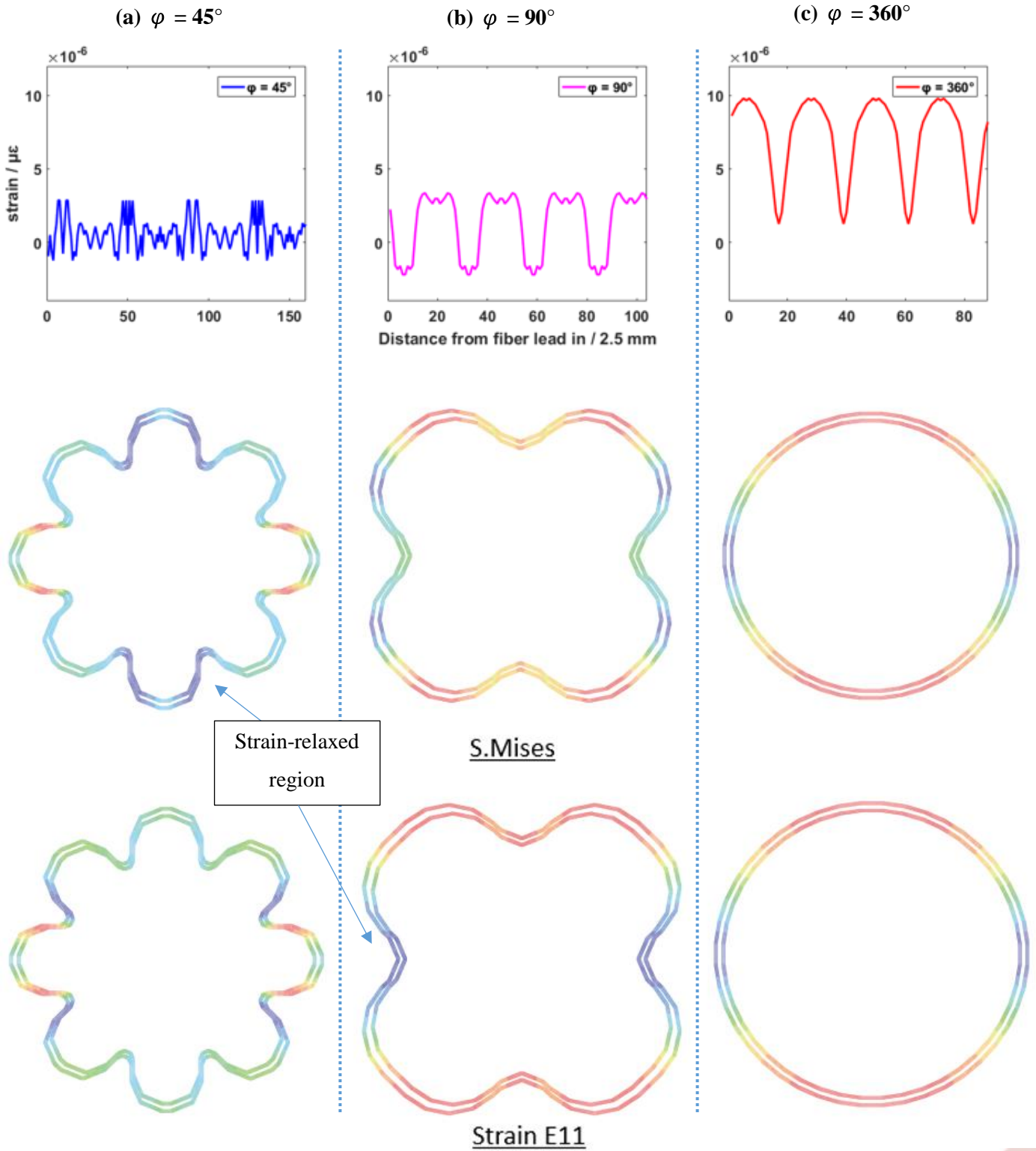
Figure 3.4.10 Simulated strain responses from tensile testing along the diagonal. Similar ranges of fiber strain responses are found at $\varphi = 45°$ and $90°$. Strain range is the highest at $\varphi = 360°$.

Although at $\varphi = 45°$, the elastic modulus is the closest to the raw silicone substrate, this fiber routing requires a small minimum bending radius which is smaller than the suggested minimum bending radius of the FBG. In practice, $\varphi = 90°$ would be a better routing configuration by considering a safety factor on the FBG breaking limit.

3.5. Conclusions

In this chapter, a Finite Element based sensor design workflow is introduced. Strain distributions of common deformation modes are simulated and analyzed to determine the general shape and position of the optical fiber. Three sensor parameters, i.e. the optical fiber offset distance from mid-plane, the overall sensor thickness, and the fiber material stiffness, are briefly discussed and selected to maximize the sensor responses. The potential buckling failure mode of the proposed sensor is mentioned and suggested to be considered in the further design. Taking the fiber buckling issue into account, a study on the apparent elastic modulus of the sensor is conducted to suit applications with higher stretchability requirements. A fiber routing configuration is suggested for high stretchability applications. In the next chapter, the circular double layer design is adopted for fabrication and experimentation since stretchability is not the fundamental requirement of this work.

4. Fabrication and Learning-Based Modeling of the Sensor

4.1. Introduction

This chapter described the sensor fabrication procedure and surface shape reconstruction method by the data-driven approach. A four-step molding process is applied to fabricate the duel layer surface shape sensor. The grating parameters of FBGs are listed and discussed. The working principle of FBG is briefly introduced with the idea of Bragg wavelength detection. Owning to the multimode sensitivity of fiber Bragg gratings, i.e. thermal and strain sensitivity, a temperature compensation scheme is used to retrieve accurate and precise mechanical strain-induced wavelength data. The reflected spectrum from our proposed sensor is captured by the FBG interrogator and post-processed to discrete wavelengths which represent the transferred strains from the sensor deformation, via peak searching algorithm. The resultant strains are simulated by FEA and used as neural network inputs. The simulated strain patterns are then tested to ensure the uniqueness of sensor responses. The accuracy of the proposed sensor is estimated by trained network errors.

4.2. Sensor Fabrication

Fabrication procedure

The surface shape sensor was fabricated by casting platinum-catalyzed silicones, i.e. Ecoflex 00-30. Ecoflex silicones were chosen due to their low viscosity that favors mixing and de-airing in fabrication and high bonding strength with current soft robots which commonly use similar silicones. Molds were designed with special patterns for different fiber configurations. In this work, we focused on general surface sensing and the structural simplicity, hence a circular fiber configuration was used. Additional simulation studies have been carried to analyze sensor responses and structural properties on various configurations and will not be discussed in this context.

As shown in **Figure 4.2.1**, a mixed portion of silicones was degassed and injected into 3D-printed molds which coated with releasing agent. It was then kept in an oven at 55 °C for 60 minutes. After demolding the patterned silicone plate, the top and bottom surfaces of the plate were penetrated with a needle for passing the fiber. Since stresses were induced by shaping the fiber to target configuration, small pins are used to temporally fix the fiber shape on the silicone plate, avoiding the fiber returns to neutral position. A thin layer of ELASTOSIL® E41 was applied to partially seal the optical fiber and silicone plate. Step 3 was repeated on the other surface and pins were removed. Finally, two thin silicone coatings (same material as silicone plate) were placed and bonded firmly on the top and bottom surface of the silicone plate as protective layers. Destructive tests have been conducted and demonstrated a high bonding strength developed between the fiber and silicone plate.
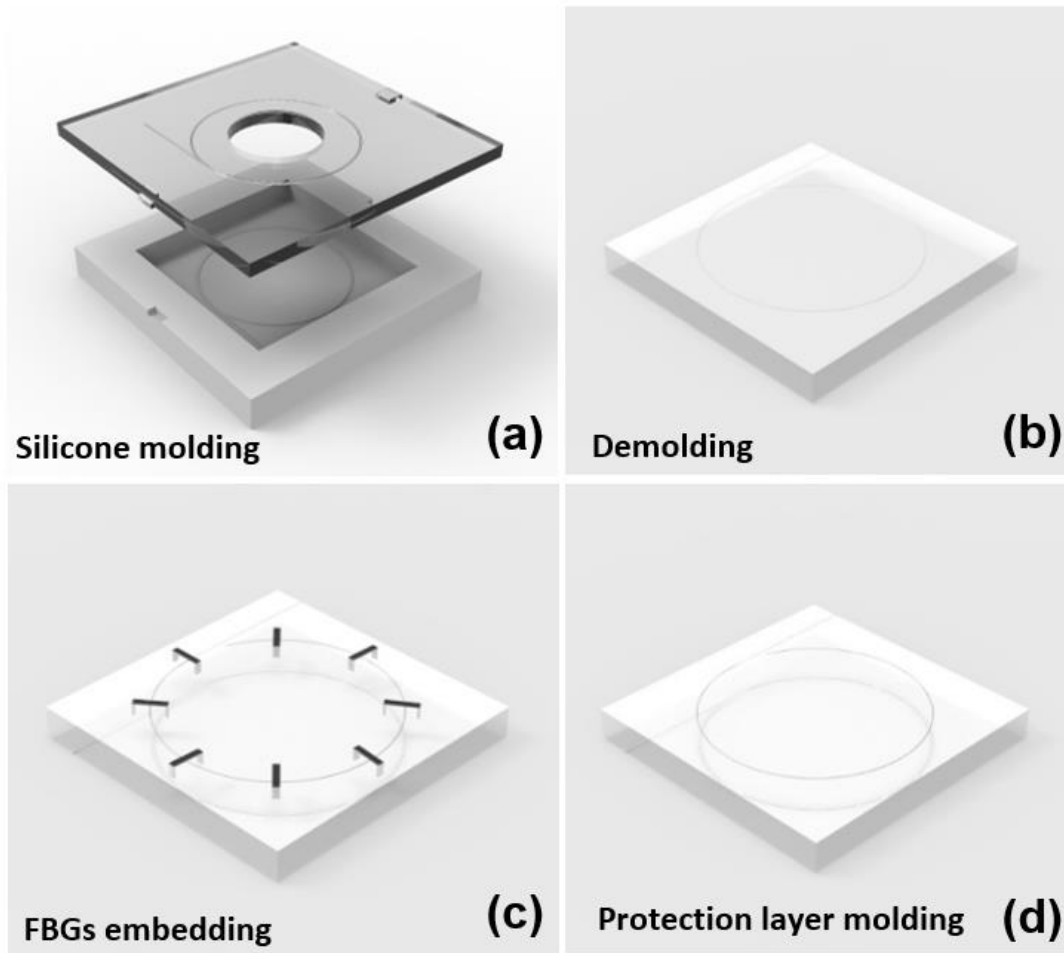
Figure 4.2.1 Fabrication process of our proposed surface shape sensor. **(a)** Silicone molding: Silicone is injected into 3D-printed molds. **(b)** Demolding: Cured silicone with designed channels is removed from the mold. **(c)** FBGs embedding: A fiber carrying FBGs is pinned to the desired configuration. The silicone-based adhesive is applied for bonding. **(d)** Protection layer molding: Fixture pins are removed. Thin layers of silicone are filled on the two sensor surfaces for protection.

Grating design of FBGs

The fiber Bragg gratings embedded in the silicone plate are made from intense ultraviolet light exposure on the optical fiber core. A fixed index modulation, i.e. a grating, is created and increased the core refractive index permanently. The locations and separations of the fiber Bragg gratings on the designed single mode (SM) optical fiber are described in **Figure 4.2.2**. It has a cladding diameter of 125 um and is coated with Ormocer (a diameter of 195 um). Each grating has a length

of 5 mm which smaller length is also available in practice. Each grating is separated with a 10 mm gap for the first 16 FBGs and the distance between 16th and 17th FBG is 450 mm. 16 FBGs covered two surfaces of the silicone plate to capture strain information and the remaining FBG is used as a temperature compensation sensor. It is positioned away from the 16th FBG for the ease of assembly. The first grating starts at 1588 nm and ends at 1540 nm for the last grating. The center wavelength of each FBG reflection peak has a wavelength separation of 3 nm to its neighbors to prevent overlapping of reflection peaks and to ensure clear peaks identification. Depending on the applications, the separation could be tuned for more/fewer FBGs. Gratings with shorter wavelengths, e.g. 1540 and 1543 nm are located closer to the fiber lead-in end while gratings with longer wavelength are put near to the lead-out end. Consider the optical energy propagates in optical fiber, a large portion of energy is confined in the core while the remaining travels in the cladding. Since the shorter the reflected Bragg wavelengths, the larger the optical loss is, FBGs with shorter wavelengths are placed near to the lead-in end. The reflectivity of the fiber is over 10% and Full width at half maximum (FWHM) is 0.15 nm. The fiber is bend-insensitive and has a bending radius up to 6 mm. The reflected spectrum captured by an optical spectrum analyzer (Anritsu MS970A).
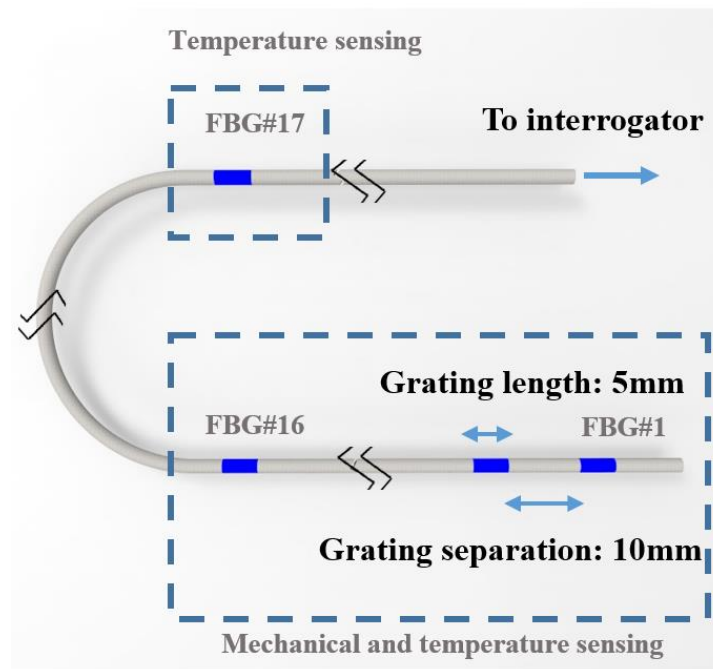
Figure 4.2.2 FBGs configuration. Gratings are fabricated inside an Ormocer coated low bend loss 125um fiber that is optimized for 1550nm wavelength window. A temperature sensing grating is put near the lead in position. The grating is 5-mm long. The grating separation is 10 mm among FBG#1 – 16 and 50 mm between FBG#16 and #17.

For any local deformation occurs on the side of the sensor, strains will be generated according to the deformation location and resulted in individual grating responses. For deformations on the center of the sensor, it is expected to generate global grating responses but with lower magnitude, since the gratings are surrounding the center but not in align with the resultant strain. Using the combination of these grating responses, the sensor is able to reconstruct and discriminate different deformation mode shapes, including bending and twisting poses, which are commonly seen in soft robotics.

4.3. Surface Shape Reconstruction

The sensing principle of our flexible shape sensor is based on global and local strain sensing. When the sensor is deformed by bending load, twisting load or other loadings, the FBG sensors embedded experience unique displacements or strain fields generated from the deformations. The strains are transferred onto the FBG sensors with a particular strain transfer rate, depending on the fabrication and bonding quality. The decomposed axial strains along the fiber are then converted to optical signals in which different strains will result in different wavelength components and measured by FBG integrator. By the strain-displacement mapping, the shape reconstruction is determined. In 3D elasticity, the relationship between strain ε and displacement u is defined as:

$$\varepsilon_{ij} = \frac{1}{2}\left(u_{i,j} + u_{j,i} + u_{k,i}u_{k,j}\right) \tag{4.3.1}$$

Where k sums over 1, 2 and 3.

4.3.1. Neural Network Training

An artificial neural network is composed of a network of neurons that change their internal activation states and generate outputs when inputs are received. The outputs and inputs of specific neurons are linked to each other and formed a direct and weighted graph. The weights are computed throughout a training process with a preselected learning function. The performance of the network can be adjusted by varying the governing learning rule thus weights of the neurons and activation. This data-driven approach usually requires a large

number of samples for training the model which maps the input variables to target outputs. A typical neuron transfer function is shown as follows:

$$o = f\left(\sum_i w_i I_i\right) + b \tag{4.3.2}$$

$$f(x) = \frac{1}{1 + e^{-x}} \tag{4.3.3}$$

where o is the scalar output, f is the sigmoid function, w_i is the i-th weight, I_i is the i-th input and b is the bias.

In this work, we focused on the surface reconstruction from the sensor measurements. To prove the uniqueness of the mapping and predict our proposed sensor accuracy, surface information (i.e. displacement data) and simulated strain responses are extracted from FEA database for training. Using the finite element model defined in the previous section, pressure loadings were generated randomly on the highlighted surfaces as shown in **Figure 3.2.20**. The use of pressure loadings creates a smooth deformed surface without applying a concentrated force on a particular element or node, which will easily distort the elements. With a defined range of pressure, 729 simulations are done where each contains 10 steps thus 7290 data sets are generated. Some simulated responses are shown in **Figure 4.3.1**. The x, y and z displacements of the nodes are extracted as target outputs, while the fiber strains (strain patterns) are defined as network inputs.
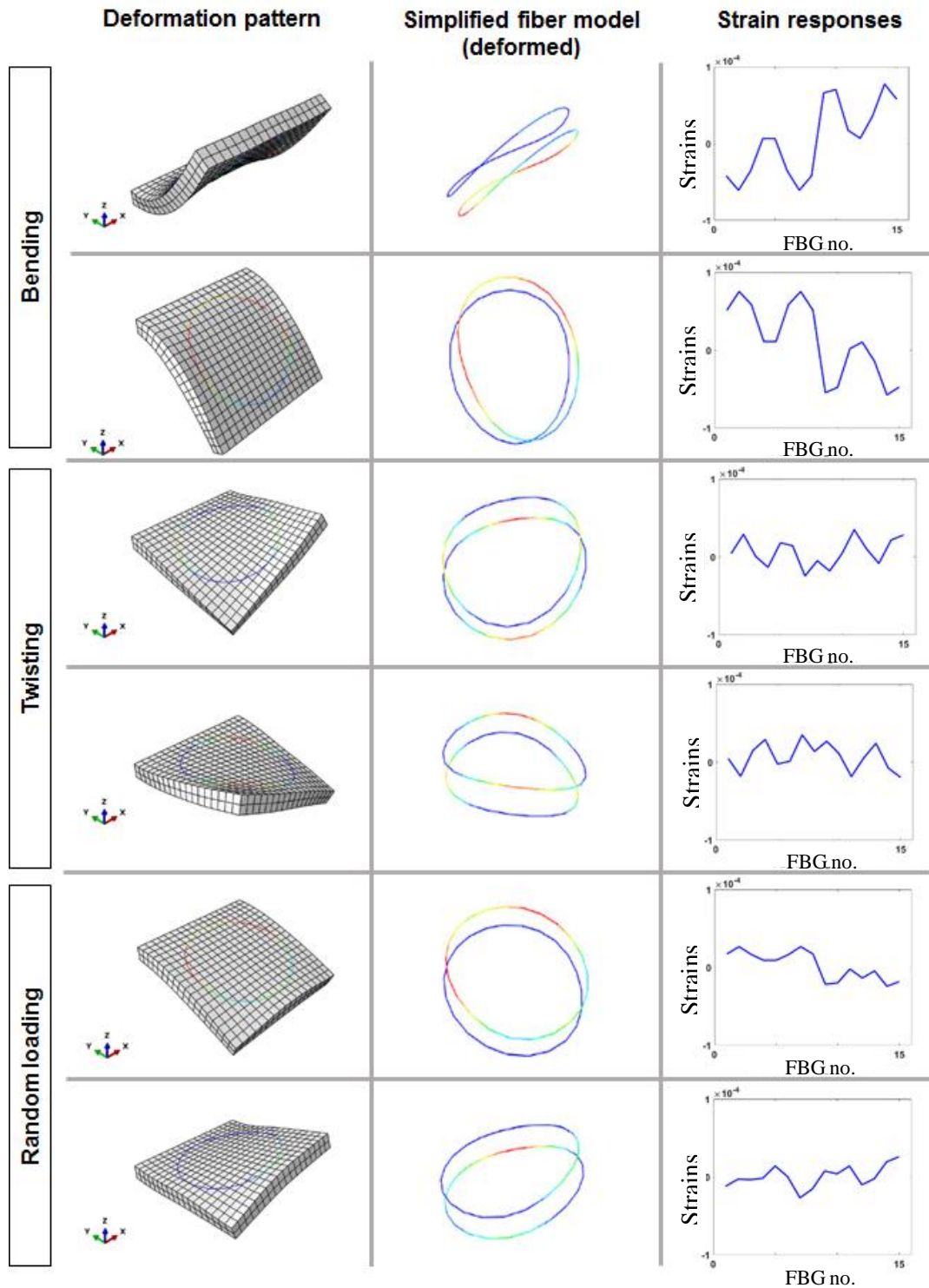
Figure 4.3.1 Simulated fiber strains under different deformations. The first column shows the deformed shape sensor under different loading combinations. The second column shows the colormap of the deformed fiber in elastic strain component E11. Warmer color indicates a higher strain induced on the fiber. The third column shows the simulated fiber strain patterns which are the basis for identifying and discriminating different deformation modes. The strain responses are neural network inputs and the node displacements are targeted neural network outputs.

4.3.1.1.   *Data-driven uniqueness*

Figure 4.3.1 clearly showed that the mapping between strain patterns generated by common deformation modes and the deformed shape was unique. However, there could be non-unique mappings for other deformation modes which visual inspection is inappropriate and impossible to be used in determining whether the remaining mappings are unique or not. An alternative solution is to form a neural network to examine the uniqueness of the mappings. By learning a large dataset with randomly generated FE simulations, a network could be trained to predict the deformation or surface shapes by inputting fiber strains or wavelength responses. Given the regression index is low, a poor network estimate can be concluded which indicates non-unique deformation-wavelength mappings exist and the sensor could not discriminate the surface deformations.

A typical multilayer feedforward network with two layers was built for training. The first hidden layer contains 10 neurons which connect to the inputs and the second layer produce the network outputs. The transfer function for the hidden layer is hyperbolic tangent sigmoid function and the function of the output layer was linear transfer function. The inputs in the neural network were the 44 sparse axial strains in fiber truss elements and the output nodes were from 1083 displacement data. Scaled conjugate gradient backpropagation was used since the network output dataset was large and requires less memory for calculations and quick estimations which the performance is close to Levenberg-Marquardt backpropagation. In the experimental section, Levenberg-Marquardt backpropagation was used instead as network size reduced in actual sensor prototype. It updates the $(k+1)^{\text{th}}$ network weight vector $w \in \mathbb{R}^n$ using the following rule:

$$w_{k+1} = w_k + \Delta w_k \tag{4.3.4}$$

where w_k, w_{k+1} are the updated network weights at step k and $k+1$.

The Levenberg-Marquardt algorithm aims to minimize the sum of square error functions. The error function E at i-th iteration is given by:

$$E(w) = \frac{1}{2} \sum_{i=1}^{M} \sum_{j=1}^{N} e_{i,j}^2 (w) \tag{4.3.5}$$

86

where $e_{i,j}$ is the error of j-th output in the i-th pattern, M is the number of outputs, N is the number of patterns.

By minimizing **Equation (4.3.5)** w.r.t. the new weight vector,

$$\nabla E(w) = J^{\mathrm{T}}(w)e(w) \tag{4.3.6}$$

$$\nabla^2 E(w) = J^{\mathrm{T}}(w)e(w) + S(w) \tag{4.3.7}$$

$$S(w) = \sum_{i=1}^{N} e_i(w)\nabla^2 e_i(w) \tag{4.3.8}$$

$$\Delta w = -\left[\nabla^2 E(w)\right]^{-1}\nabla E(w) \tag{4.3.9}$$

Where J is the Jacobian matrix of derivatives of each error with respect to each weight.

Defining the approximation $J^{\mathrm{T}}J + \mu I$ to the Hessian matrix, the changing network weighting at step k is:

$$\Delta w_k = -\left[J_k^T J_k + \mu I\right]^{-1} J_k^T e_k \tag{4.3.10}$$

where I is the identity matrix, μ is a scalar which changes adaptively during iterations and e is the error vector.

For $\mu = 0$, **Equation (4.3.10)** becomes Newton's method. For large μ, **Equation (4.3.10)** becomes gradient descent method with a small step size. After each successful step, μ will be reduced. After a tentative step, μ will be increased to obtain reduced performance function at each iteration.

The training stopped when the magnitude of performance gradient was less than 1e-6 or the validation performance stop decreasing. In designing this neural network, 70% of the data was used for network training, 15% was used for validation and the last 15% was used for testing. In **Figure 4.3.2**, the results showed a good fit with a regression value of 0.989 and the overall errors were small. This training result was selected from the epoch 5855 with a mean square error of 0.055439 mm as shown in **Figure 4.3.3**. The high coefficient of regression implied the unique mapping of surface displacements and FBG strains. This also indicated the suggested fiber configuration was well positioned and abled to represent and reconstruct the sensor surface accurately.
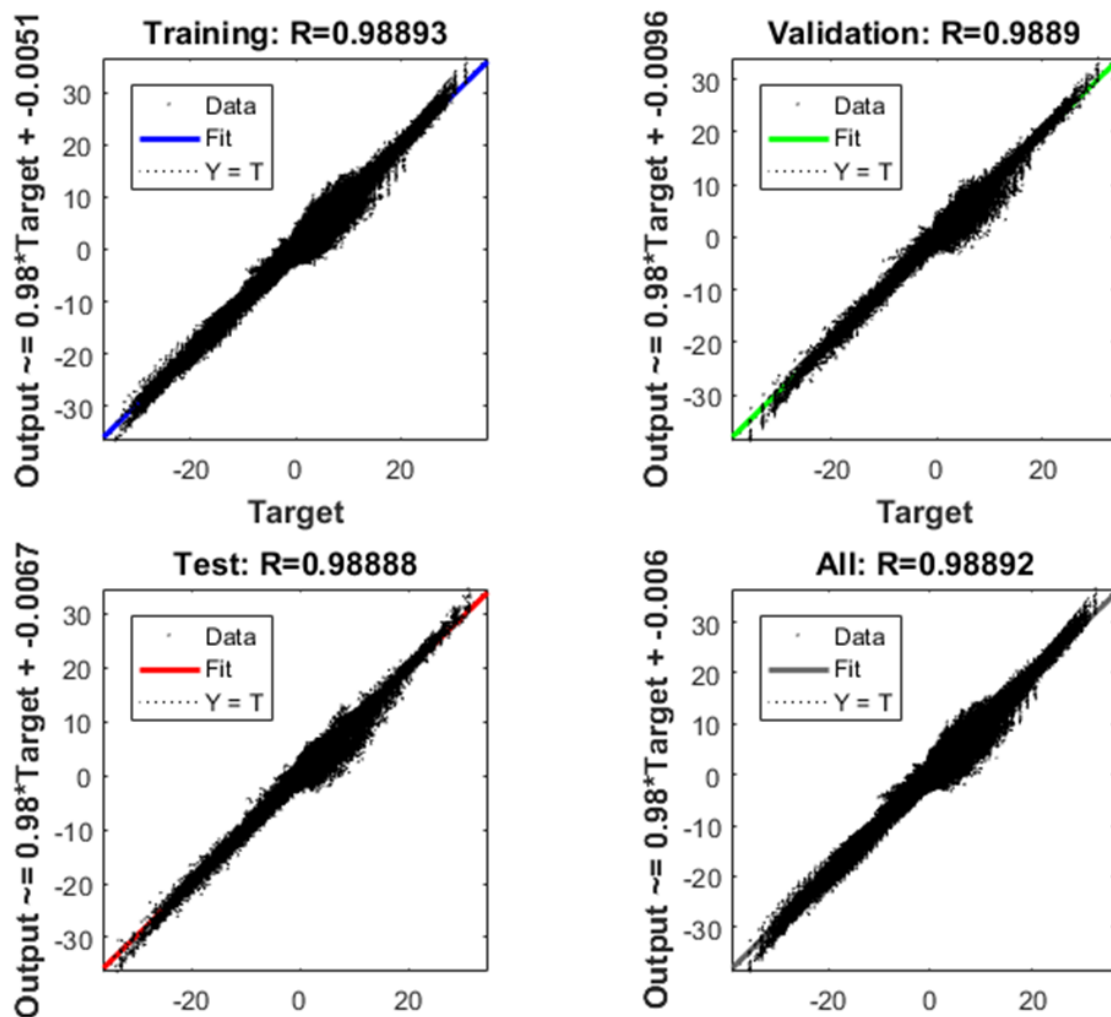
Figure 4.3.2 Regression plot for the trained neural network. The solid line in the plot is the line showing the best fit linear regression between input fiber strains and output node displacements. The datasets are fitted with a high regression index *R* that proved the mappings are unique. A more accurate network could be obtained by retraining the network with more hidden neurons, thus providing higher flexibility to the network.
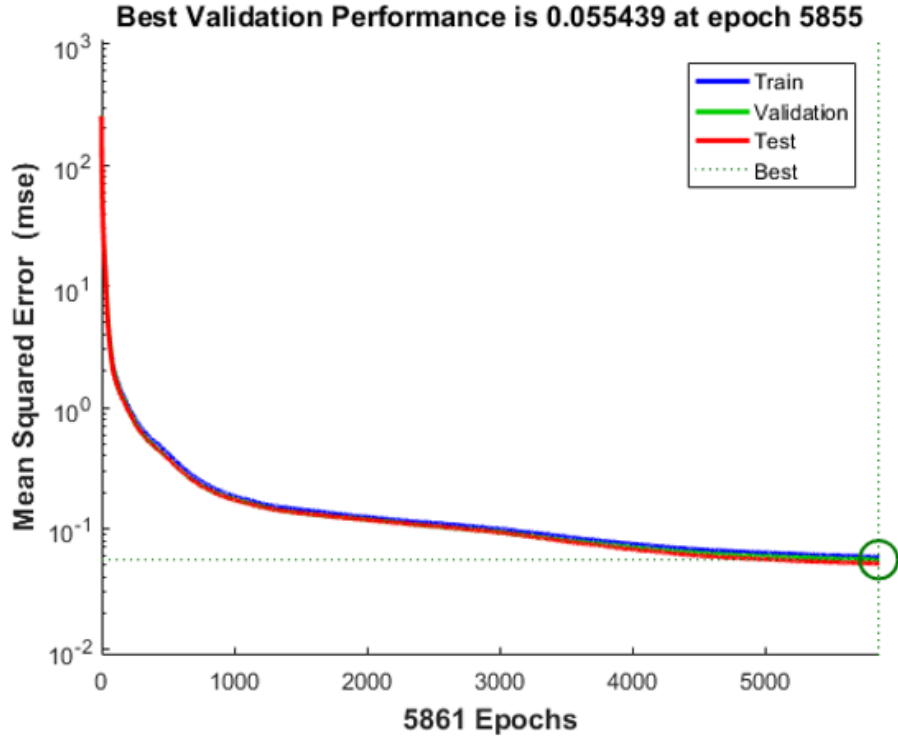
Figure 4.3.3 Neural network performance which is evaluated by the mean square error (in mm). The neural network is trained with simulated FE datasets. Axial strains of the fiber elements are neural network inputs and top surface node displacements are neural network outputs. The training stopped when preset conditions are fulfilled. The best validation performance is 0.055439 mm at epoch 5855.

After validating the uniqueness of the surface shape/displacement to strain/Bragg wavelength mappings of the proposed sensor, further analysis was done on the trained network to evaluate the network performance and predict the actual shape sensor performance. The accuracy, or the output displacement errors were defined by the root mean square error (RMSE):

$$RMSE = \sqrt{\frac{1}{n}\sum_{i=1}^{n}\left(u_{i(actual)} - u_{i(nn)}\right)^2} \qquad (4.3.11)$$

where $u_{i(actual)}$ is the ith actual displacement in the experiment and $u_{i(nn)}$ is the ith output displacement from the trained network.

Using the simulated fiber strains as neural network inputs and surface node displacements as neural network outputs from FEA, the trained neural network has a root mean square error of 0.2354 mm and a maximum error at 5.3485 mm. **Figure 4.3.4** showed the error distribution of the trained network using Matlab neural network toolbox.
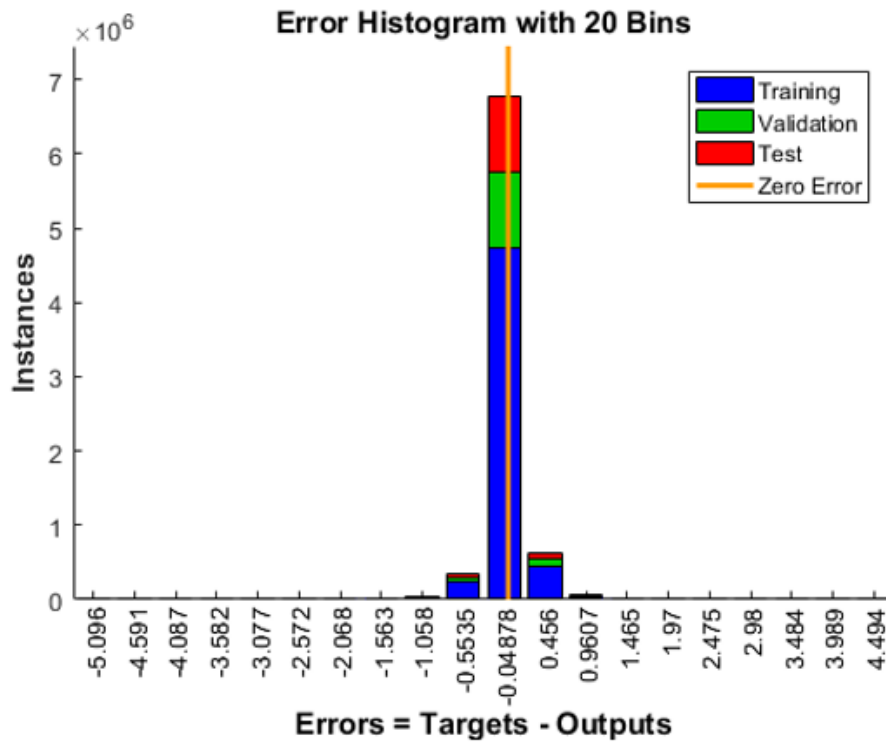
Figure 4.3.4 Error histogram of a trained neural network. FE-simulated displacements are target outputs. 70% of the data is used for network training, 15% are used for validation and the last 15% are used for testing. The root mean square error is 0. 2354 mm and the maximum error is 5.3485 mm.

4.4. Conclusion

In this chapter, prototype of the proposed sensor was fabricated with parameters determined in **Chapter 3**. The fabrication procedure was shown and the grating design of the FBGs was briefly discussed. The concept and working principle of FBGs were explained in detail. To eliminate the effect of temperature, a compensation scheme was introduced by using a temperature-measuring FBG. The uniqueness of the mapping between fiber strains and surface shape of the sensor was proven with the aid of an artificial neural network. Based on FE simulations and neural network training results, the accuracy of the proposed sensor was estimated. In the next chapter, the fabricated sensor was tested and evaluated.

5. Experimentation and Result Discussion

5.1. Experimental Setup

To capture the data on the deformed surface, the sensor was clamped to a rigid fixture which limited the displacements only at one side, as shown in **Figure 5.1.1**. The Optitrack motion tracking system was used with two Flex 3 cameras to retrieve surface displacement information which provided groundtruth data for neural network training. Passive markers were placed on the sensor surface to reflect IR light for tracking. As the silicone surface has low surface energy and difficult for markers to attach firmly, Loctite 495 was first applied to the surface and bonded to small paper strips that allow markers to position. The paper strips can be easily debonded after capturing data. The streaming rate is 100 frames per second and the total number of markers is nine because of the tracking system's limitations. After calibration, the mean positional error is 0.015 mm.
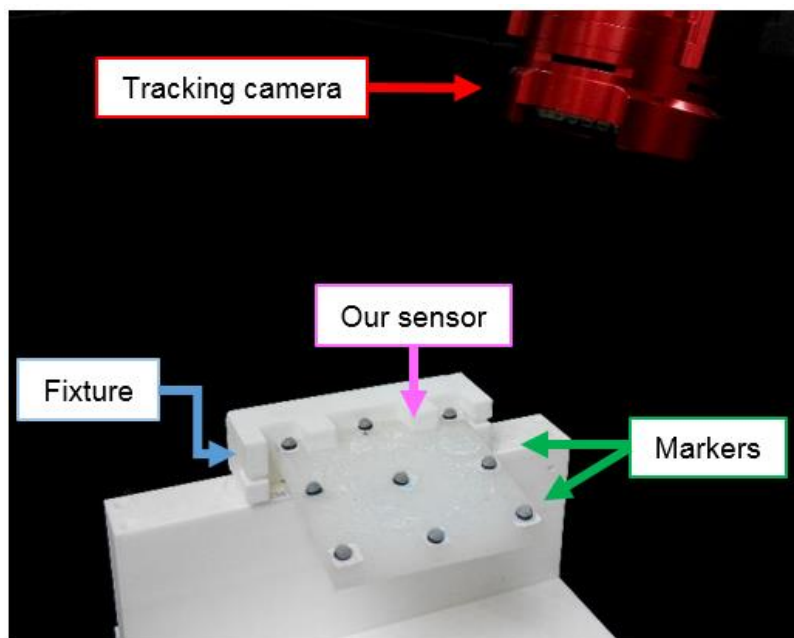
Figure 5.1.1 Experimental setup for training data collection. The sensor is covered with 9 passive tracking markers and clamped on a fixture. Two Optitrack Flex 3 cameras are used to record the surface displacement data from the markers' positions at 100 fps. The mean positional error is 0.015 mm after calibration.

A light source (Amonics ALS-CL-GFF-18-B-FA) transmited broadband invisible light from 1500 to 1595 nm to the optical fiber via an optical circulator (PIOC-3-CL-P-90-10-FA). Light was reflected due to the change in core refractive index which is strain dependent. Since light is multiplexable, light reflected at each grating adds up to a reflected spectrum as shown in **Figure 5.1.2**. The reflected spectrum was sent to a FBG interrogation monitor (I-MON 512 USB) from the output port of the optical circulator. This interrogation system can sense and identify over 70 FBGs with a wavelength resolution smaller than 0.5 pm and a maximum measuring frequency of 3000 Hz. The Bragg wavelengths were identified by peak searching algorithm and sent to PC for analysis and surface reconstruction.
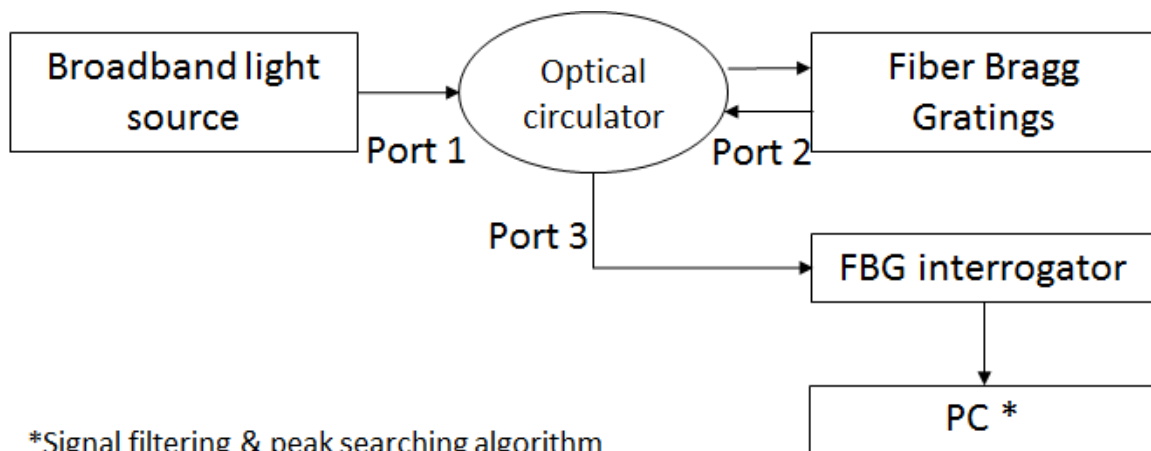
Figure 5.1.2 Schematic diagram of the sensing system. A light source, the presented shape sensor, and a FBG interrogator are connected by a three-port optical circulator. With most of the incident spectrum transmitted to the end of the fiber, the reflected spectrum exited at port 3 and captured by the FBG interrogator. The optical signals are then sent to PC for wavelength calculations.

To generate different and complex deformation patterns, the sensor was bent manually without blocking the tracking markers for sensing. Linear actuator arrays were not used to generate loading patterns due to the size limitation and low flexibility of controlling sensor's degrees of freedom. It could easily block the markers when the actuator end was not fixed to the sensor or causes damage to the sensor when firmly fixed. As we have an optical interrogation system and motion tracking

system at a high sampling rate, deforming the sensor manually allows complicated pattern formation with short sampling time. 1000 postures with corresponding Bragg spectrum were captured and trained with the same neural net setting in **Section 3.3**. Although there could be fabrication defects and fiber dislocations, no calibrations are required since these errors are automatically compensated when training the neural network.

5.2. Sensor Performance Analysis

After fabricating the physical sensor model, an artificial neural network (ANN) was trained to develop the sensor model. The parameters used in **Section 4.3.1** were applied to the training of this ANN. The neural network outputs were changed to displacements of the 9 surface nodes as shown in **Figure 5.1.1**. The neural network inputs were changed to temperature-compensated Bragg wavelengths. The node displacements were captured by the motion tracking system and mapped to the Bragg wavelengths at the same timestamp. In **Figure 5.2.1**, the proposed sensor was able to reconstruct the surface shape using the trained sensor model. The performance of the proposed sensor is discussed in the next section.
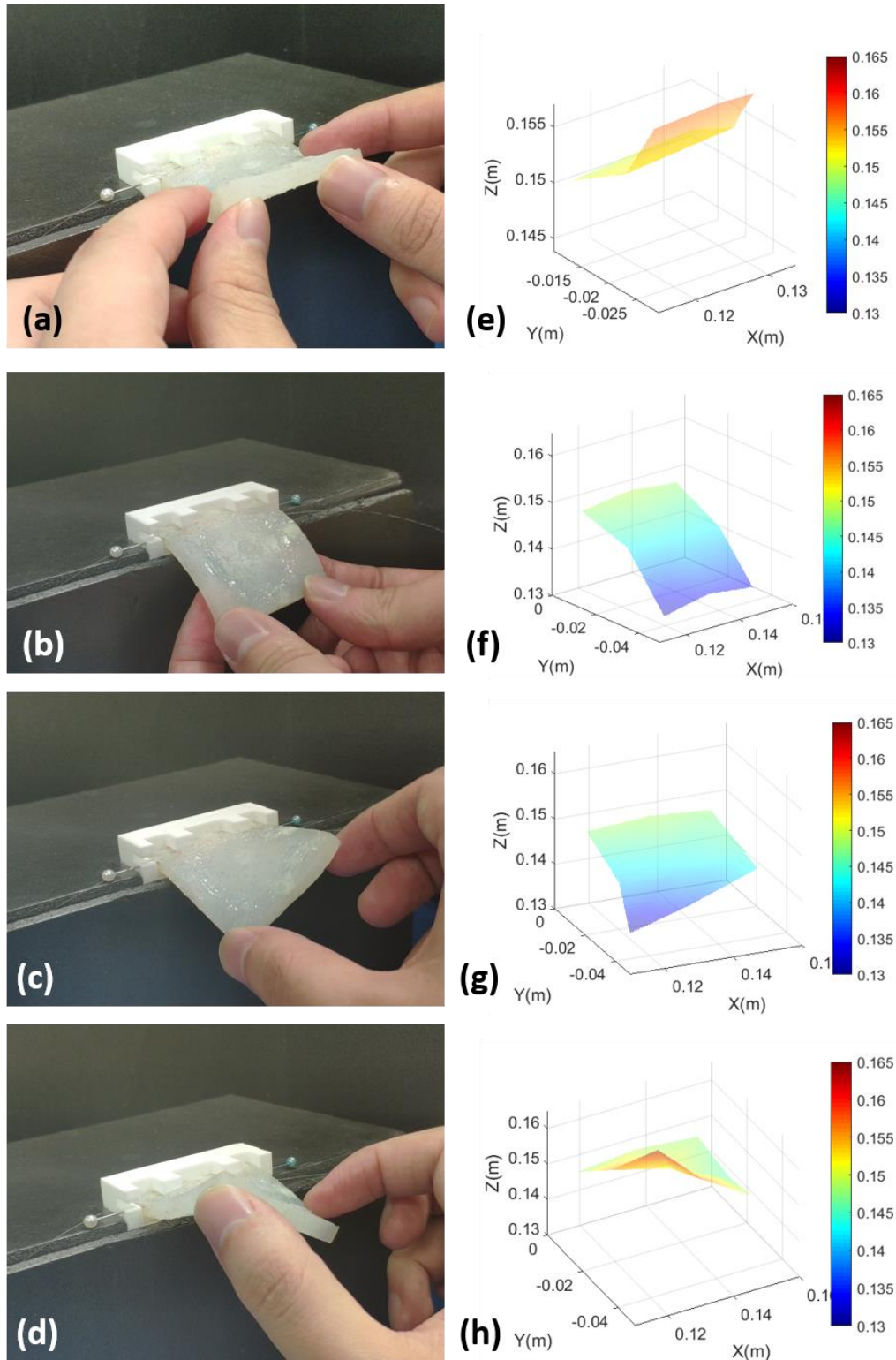
Figure 5.2.1 Surface shape reconstruction example. **(a-d)** A force is applied to the sensor and caused deformations on the sensor surface. **(e-f)** The sensor surface is reconstructed by the trained neural network. The colormap indicated the depth of the surface.

During the training, the error reduces in general with the number of epochs. In dataset validation process, the training data may be overfitted by the neural network, causing sudden changes in performance gradient. This can be observed from the training performance plot shown in **Figure 5.2.2**. The network training stopped when the validation error increased in six consecutive tests. The best validation performance was 8.5275×10^{-7} m at epoch 46 which has the lowest error among the validation tests. The trained network performance is also validated from the regression plot. The plot showed the trained neural network outputs against the expected outputs (the targets / actual outputs) for the three datasets, i.e. training, validation and test datasets. In **Figure 5.2.3**, most of the data was plotted on the line where the slope of the line is 1. This suggested the degree of fitness of the data. In this work, the R-value equals to 0.999 which showed a precise fit of the data and a superior performance of the trained network. Note that with different training parameters, algorithms and seed, the training result may vary as the network weights and biases change.
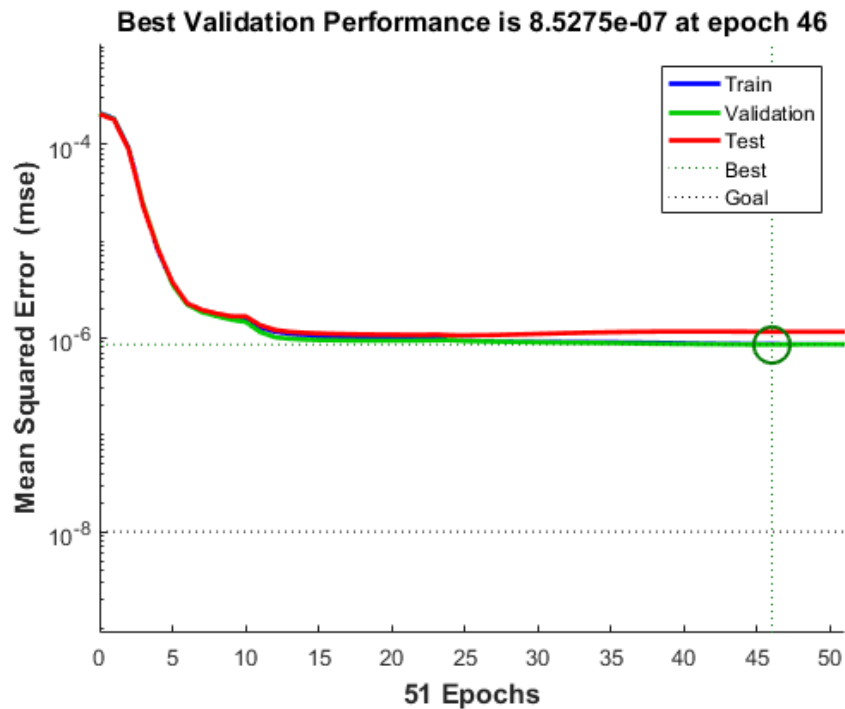
Figure 5.2.2 Neural network performance which is evaluated by the mean square error (in m). The neural network is trained with sensor displacements and Bragg wavelengths. Bragg wavelengths of the proposed sensor are neural network inputs and top surface displacements are neural network outputs. The training stopped when preset conditions are satisfied. The best validation performance is 8.5275×10^{-7} m at epoch 46.

96
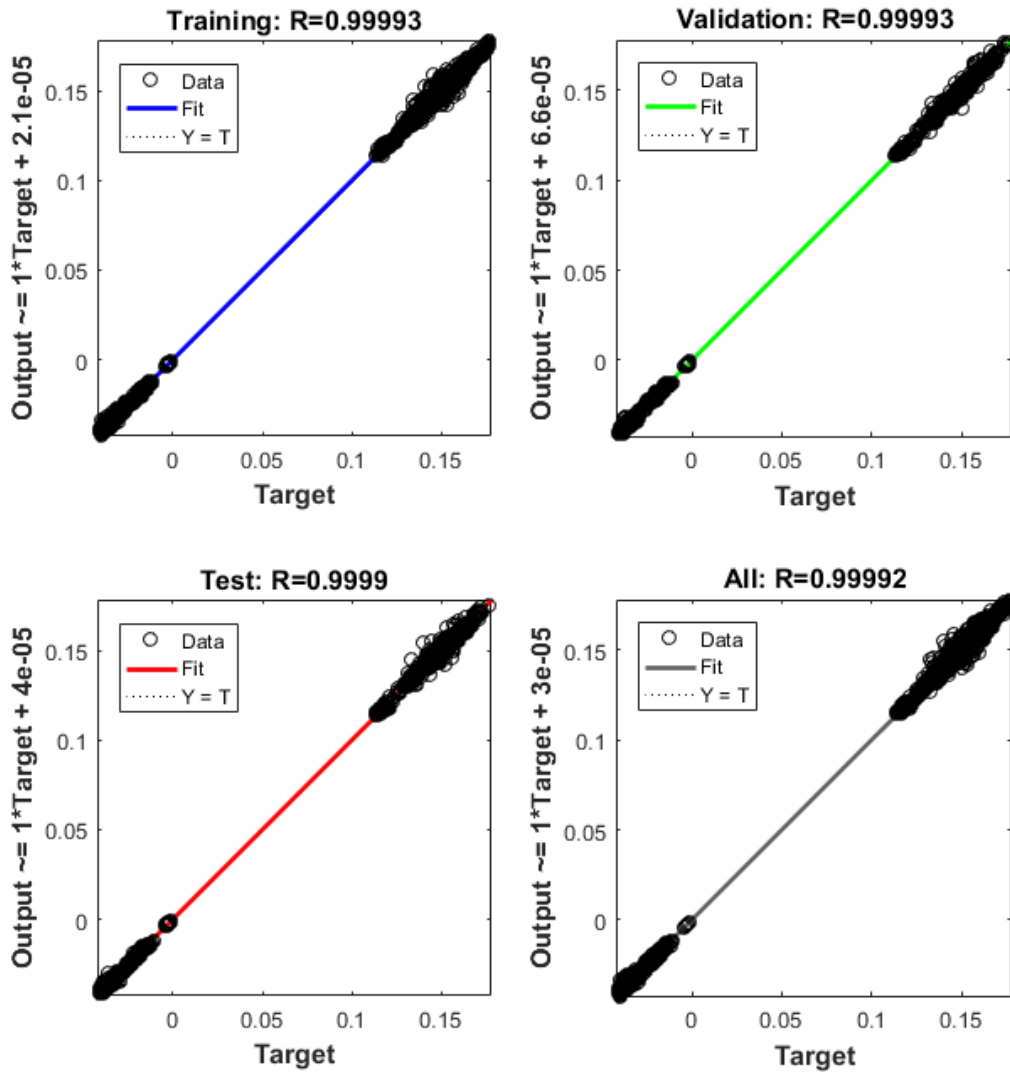
Figure 5.2.3 Regression plot for the trained neural network. Solid lines in the plot are the lines showing the best fit linear regression between input Bragg wavelengths and output displacements on the sensor surface. The datasets are fitted with a high regression index *R* that proved the mappings are unique as previously tested in **Section 4.3.1**. A more accurate network could be obtained by retraining the network with more hidden neurons, thus providing higher flexibility to the network.

5.2.1. Accuracy

Similar Bragg wavelength patterns were observed and agreed with simulation results. In this experiment, 16 Bragg wavelengths with temperature compensation were set as inputs and 27 displacements were defined as outputs, to model wavelength and displacement relationship. The root mean square error for all reconstructed displacement nodes was 0.9234 mm and maximum error was 4.81 mm. The rose in RMS error (compare to the FE simulation) result may come from the measurement noise, calibration errors from groundtruth measurements and the use of simplified FE model. However, still, the sensing accuracy outweighs recent shape sensing devices. Common deformation mode shapes, such as bending and twisting, can also be reconstructed by the trained network. The measurable bending curvature is from 0 to 0.04 mm^{-1}. The refresh rate of the surface sensing loop was over 10 Hz with Matlab surface plotting function. Higher refresh rate can be achieved by using other programs with better graphics and update capability. An error plot indicating x-, y- and z- displacements errors is shown in **Figure 5.2.4**. In low error range, all directions have similar displacement errors. High errors always found at z-displacements because the boundary condition forced and limited the total displacement along x- and y-axis. So generally, the nodes move with a larger z displacement hence the z-displacement error has a larger portion at higher error range. The errors tend to locate at nodes near the free boundaries (**Figure 5.2.5**) as a result of larger displacements experienced. When loadings are added on the free corners, the moment is larger than other loading positions. This makes the sensor deformed more at the loading position thus a larger resultant displacement comparing to other nodes. Also, the corners are far from the gratings, thus the deformations at the corners may not be reflected in the sensing data. **Figure 5.2.6** shows the nodal displacement tracking over a period of time under random deformations.

The accuracy at these positions could be improved by relocating the FBGs to the free ends to increase the sensitivity at the boundaries. Hence the free edge will be more sensitive to large displacements and higher accuracy could be reached with better training results.
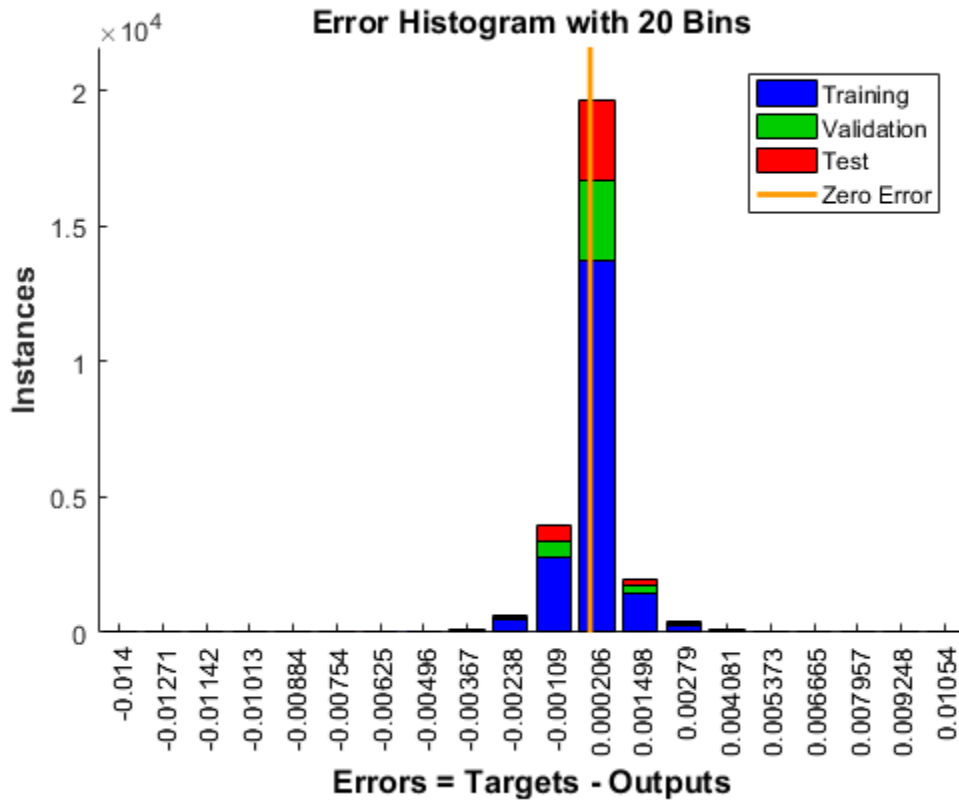
Figure 5.2.4 Error histogram of a trained neural network. Actual displacements, i.e. the tracking marker positions are target outputs. 70% of the data is used for network training, 15% are used for validation and the last 15% are used for testing. The root mean square error is 0.9234 mm and the maximum error is 4.081 mm.
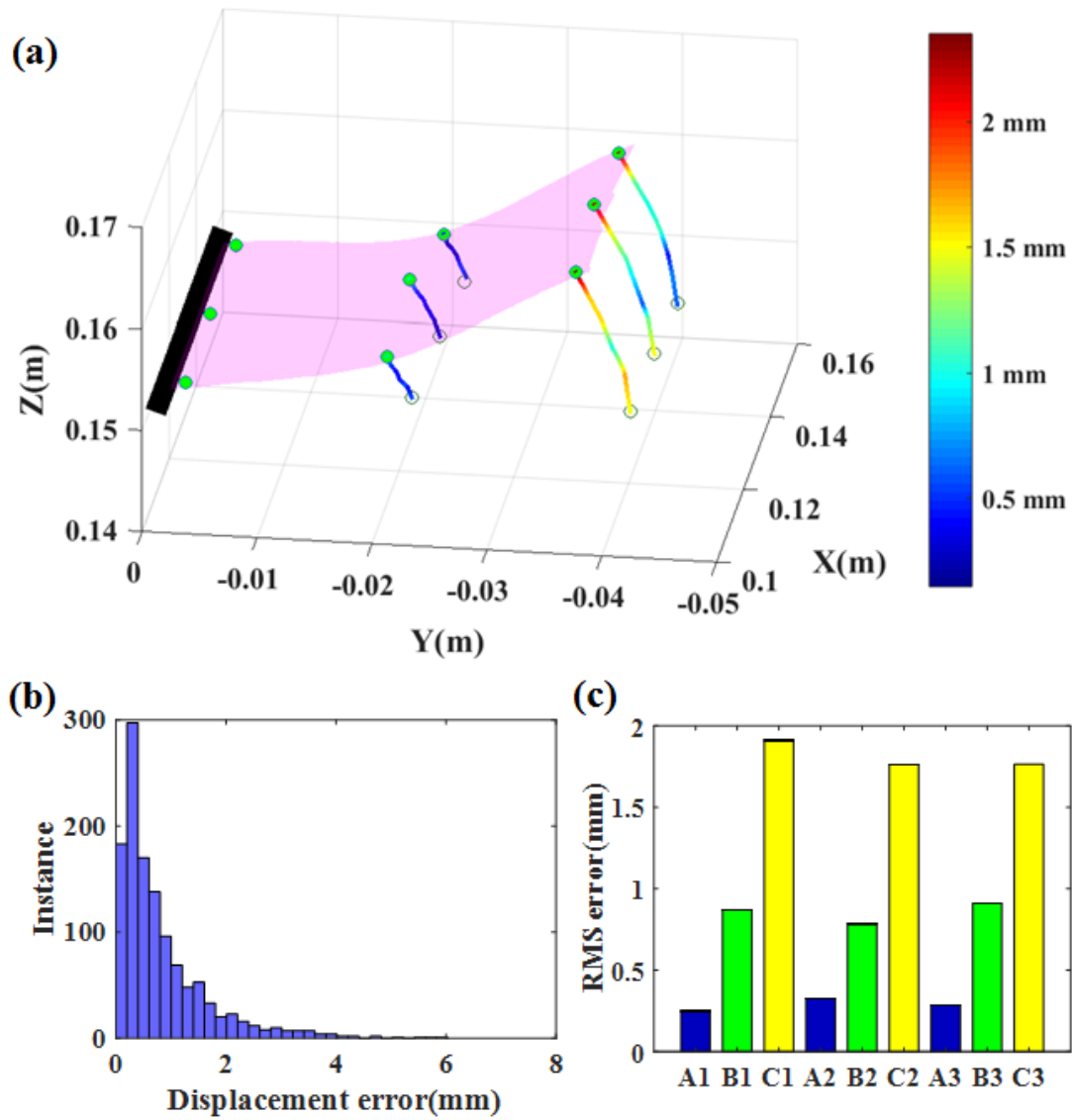
Figure 5.2.5 Accuracy analysis on the surface shape reconstruction. **(a)** Surface reconstruction with trajectory lines of the nodes, where the color represented the magnitude of displacement errors. The distribution of all nodal displacement errors was shown in **(b)**, and **(c)** indicated that the nodes far from the clamped side suffered larger RMS error.
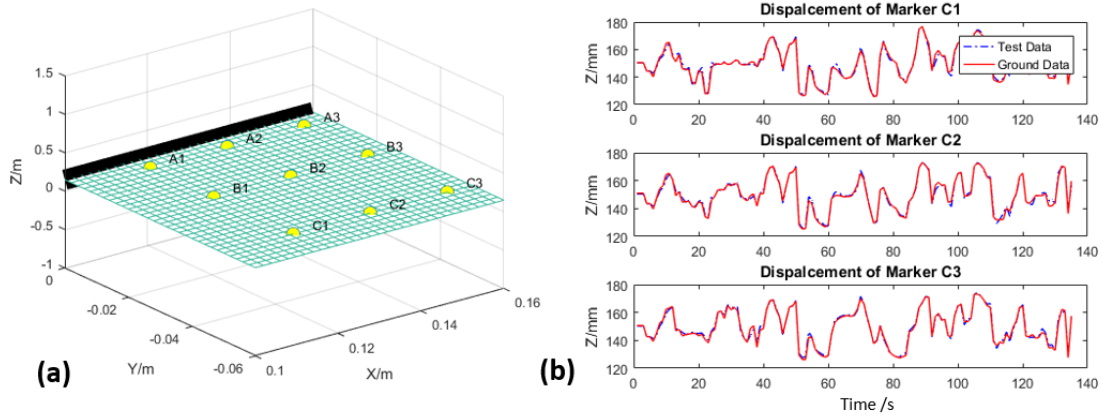
Figure 5.2.6 (a) Markers definition over the sensor surface. **(b)** Tracking performance of the nodal displacements (C1-C3) under continuous deformations.

5.2.2. *Spatial Resolution*

Two types of resolution are considered in this work. The first one is the Bragg wavelength capturing resolution. Recalling that the shift in Bragg wavelength is proportional to the mechanical strain, the displacement and strain resolution is limited by the wavelength fit resolution of the FBG interrogator which is 0.5 pm. From **Equation (2.4.6)**, when there is no temperature variations ($\Delta T = 0$) and the base wavelength $\lambda_0 = 1500nm$, the change in strain equals to 0.42735 $\mu\varepsilon$. Note that the apparent wavelength resolution could be affected by the random error in wavelength detection which is discussed in the next section.

Another one is the grid size of the reconstructed surface shape which is controlled by the desired control points (loading points). In this work, the grid resolution in both *x* and *y*-direction is 45/2 = 22.5 mm for the actual sensor. The grid resolution could be increased as demonstrated in the simulations in **Chapter 3 and 4**. Regarding the physical limitations of the proposed sensor, i.e. thickness and the selected routing configuration, it is difficult to generate deformations with a distance smaller than 22.5 mm, between two control points. The grid resolution can be refined by reducing the thickness of the sensor and fiber configurations as suggested in **Section 3.4**. Smaller grid size is available with a sensor of higher flexibility.

5.2.3. *Signal-to-Noise Ratio (SNR) and Hysteresis*

The signal-to-noise ratio (SNR) for the bent up configuration is 14.9dB, calculated by comparing the vertical displacements of the distal node and noise. The hysteresis of the sensor was also evaluated by repeatedly displacing the distal side of the sensor (nodes C1 to C3) upwards by 20 mm and returning to the neutral flat position (3 cycles at ~1 Hz). The nodes are defined in **Figure 5.2.5**(a). The vertical displacement was provided by a linear actuator, and the vertical position of the node C2 and the wavelength shift of the FBG with the largest shift was recorded. A small disparity between the bending up and return motion was found, as illustrated in **Figure 5.2.7**, suggesting a low level of hysteresis in the presented sensor. To test the resolution of the sensor, a range of vertical displacement steps ranging from 0.1 mm to 1 mm were applied to the distal sensor side. The sensor could detect displacement changes down to the applied 0.1 mm displacement, suggesting that the sensor resolution is 0.1 mm or lower.
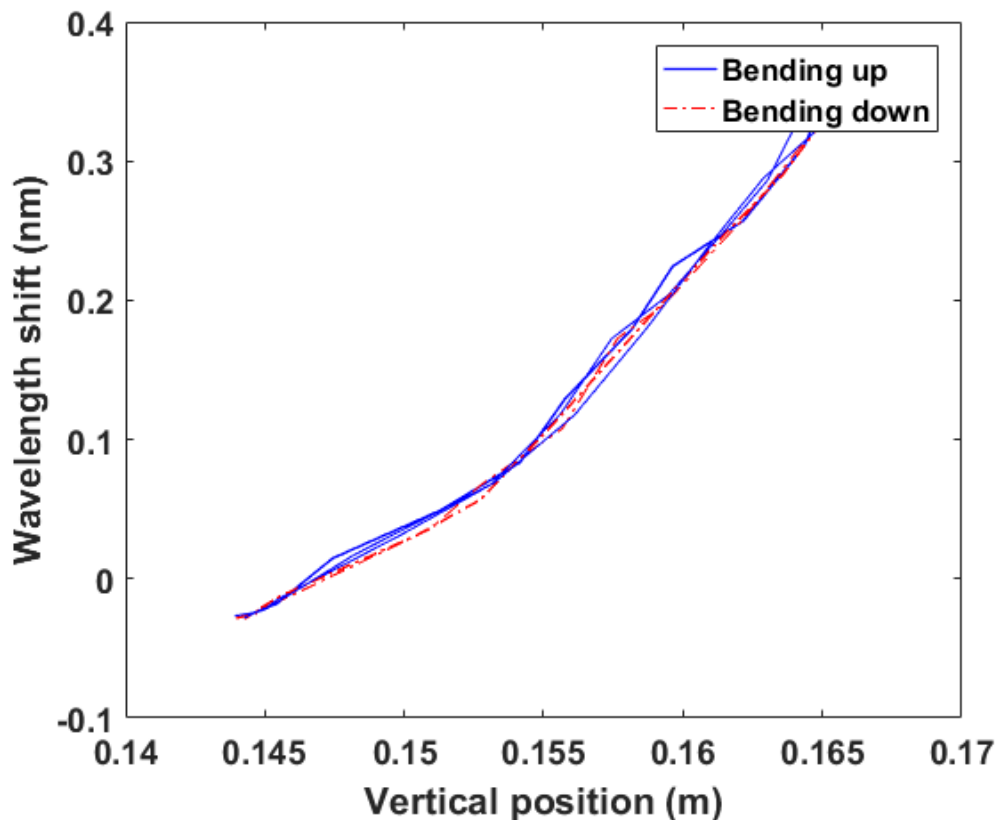
Figure 5.2.7 Hysteresis plot comparing the vertical position of the distal node C2 and wavelength shift of the FBG with the largest shift. The sensor was bent up and returned to the flat position for 3 cycles.

5.2.4. Reliability

Many existing flexible electronics are not durable and will degrade dramatically within hours. Examples are the electric skins described in **Table 2.3.1**. For robotic applications, the sensor for monitoring and feedback must be reliable in terms of functions and resistivity. FBG equipped with electromagnetic immunity and chemical and corrosion resistance in nature. For the functional reliability, reliability tests were done to ensure consistent responses over a long operating period. A cyclic loading was applied to our sensor as shown in **Figure 5.2.8**. It was bent from the normal position, upward, downward and finally back to the normal position in 2 seconds. The Bragg wavelength responses are recorded at the last step of each loading cycle. The output responses remain stable and consistently for more than 5000 cycles with a wavelength error of ± 0.0318 nm. The source of this random error could be induced from the testing environment.

From the previous section, the actual wavelength detection (random) error refers to a random error in mechanical strain measurements of 27.1795 $\mu\varepsilon$. This error should be taken into account for future development in sensor design and optimization.
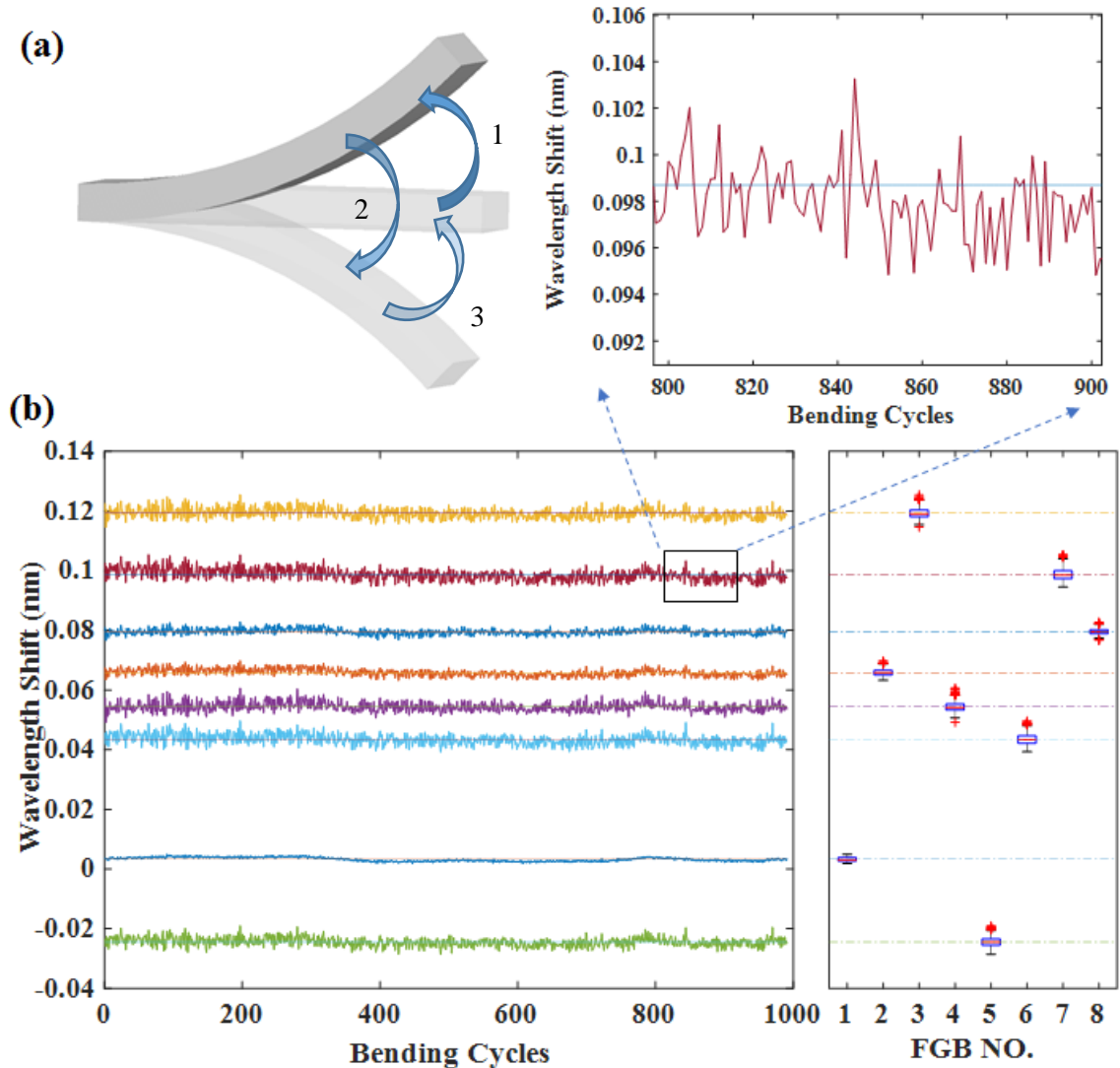
Figure 5.2.8 Repeatability test of the proposed shape sensor under periodic loadings. The sensor is clamped on a fixture and bend along the free end. The bending sequence is completed in 2 seconds for each cycle. The wavelength shifts of 8 FBGs (first layer FBGs) were shown in the figure. The wavelength shifts fluctuate around horizontal lines during the periodic motions. The boxplot shows the distributions of the wavelength shifts. From the zoom in the figure, fluctuation of the wavelength shifts is less than 0.005 nm, which is much smaller compared with the total shift.

5.3. Limitations

One major limitation of our proposed sensor is the minimum bending radius of the optical fiber. This is a physical limitation that is difficult for further enhancement. This property of FBG is

closely related to the fiber material that would affect the surface strain limit of the fiber directly. In particular, this constrained the fiber configuration design and the stretchability of the sensor.

Another limitation is the stretchability. Although the current prototype is stretchable and flexible, the allowable strain is small from pure in-plane loadings. The strain is limited by the rigid optical fiber which acts as a constraint. By varying the fiber configuration, stretchability could be enhanced as analyzed in **Section 3.4** but requires compromise with other performance or cost factors such as the length of the optical fiber, number of FBGs required and sensitivity. Further studies are required to optimize fiber configurations with different application requirements and the fabrication method for special configurations.

The remaining limitation is pressure sensitivity. As Bragg wavelengths response to mechanical strains, pressuring the sensor could affect the output displacements thus the shape reconstruction result. Other works such as optical power measures and supersonic cluster beam implantation (SCBI) technique [22], may provide information to distinguish different stimuli.

5.4. Potential Applications

To demonstrate the potential of this surface sensor, it is embedded into a wing of a small stingray model (**Figure 5.4.1**) and used to reconstruct the wing shape opposing the water current flow in real-time (**Figure 5.4.2**). In this case, the morphology and swimming movement of soft and flexible robots can be studied directly with surface information feedback. Another example is to estimate the self- or externally excited vibrations on a flexible device. Instead of surface reconstruction, displacement data are captured continuously to construct vibration waveforms and to compute the vibration periods. Since Bragg wavelength responses are captured locally over the whole sensor, motion capturing and compensations at various locations are possible with the feedbacks from our proposed sensor. Example responses of the sensor are shown in **Figure 5.4.3** where an impulse load is applied on the opposite side of the clamped edge. Similar waveforms are observed with small phase differences which indicate the vibration frequency and wave propagation.

105
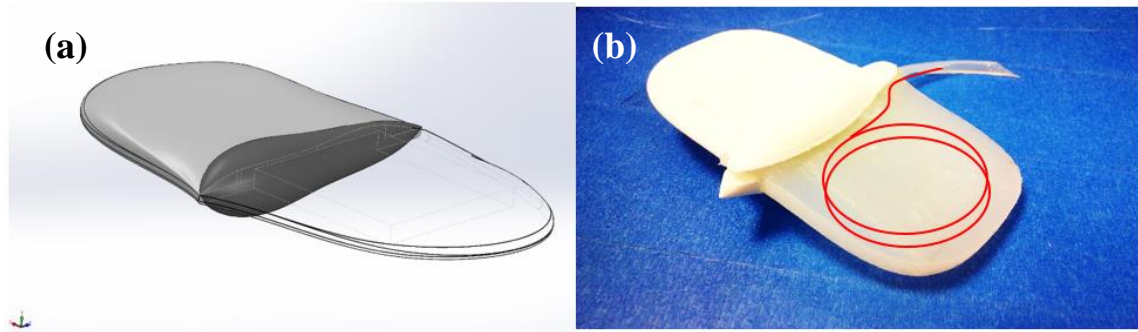
Figure 5.4.1 Surface shape sensing example. **(a – b)** The proposed sensor is embedded into the side wing of a soft stingray model. The model is placed in a water tank with oscillating currents and surface (wing) morphology can be reconstructed in real-time. This can be applied in swimming gait sensing and feedback control.

The above example demonstrated a way to study quantic locomotion. Organisms living in the ocean experience and overcome unbounded fluid flows. Studying swimming gait of these creatures help understanding interactions between dynamically changing fluid motions and benthic fish. It can also provide precise and accurate measurements on the wings of benthic fishes, or the bio-inspired robots, in order to model the dynamics under both free-stream and near-ground situations.

Understanding the swimming mechanisms of near-ground fishes, which has a higher swimming efficiency comparing to fishes with undulating fins, could inspire ocean robotic design with an energy efficient actuation system. This helps to develop a new generation of soft, ocean robots by minimizing water drag and ground effect, thus benefiting ocean exploring missions. In **Figure 5.4.2**, a surface shape sensor (which is the same as the one fabricated in **Section 4.2**) is embedded in a dummy stingray model. The model is then placed inside a water tank and experienced random water currents. The change in surface shape and nodal displacements are plotted under Matlab in real-time.
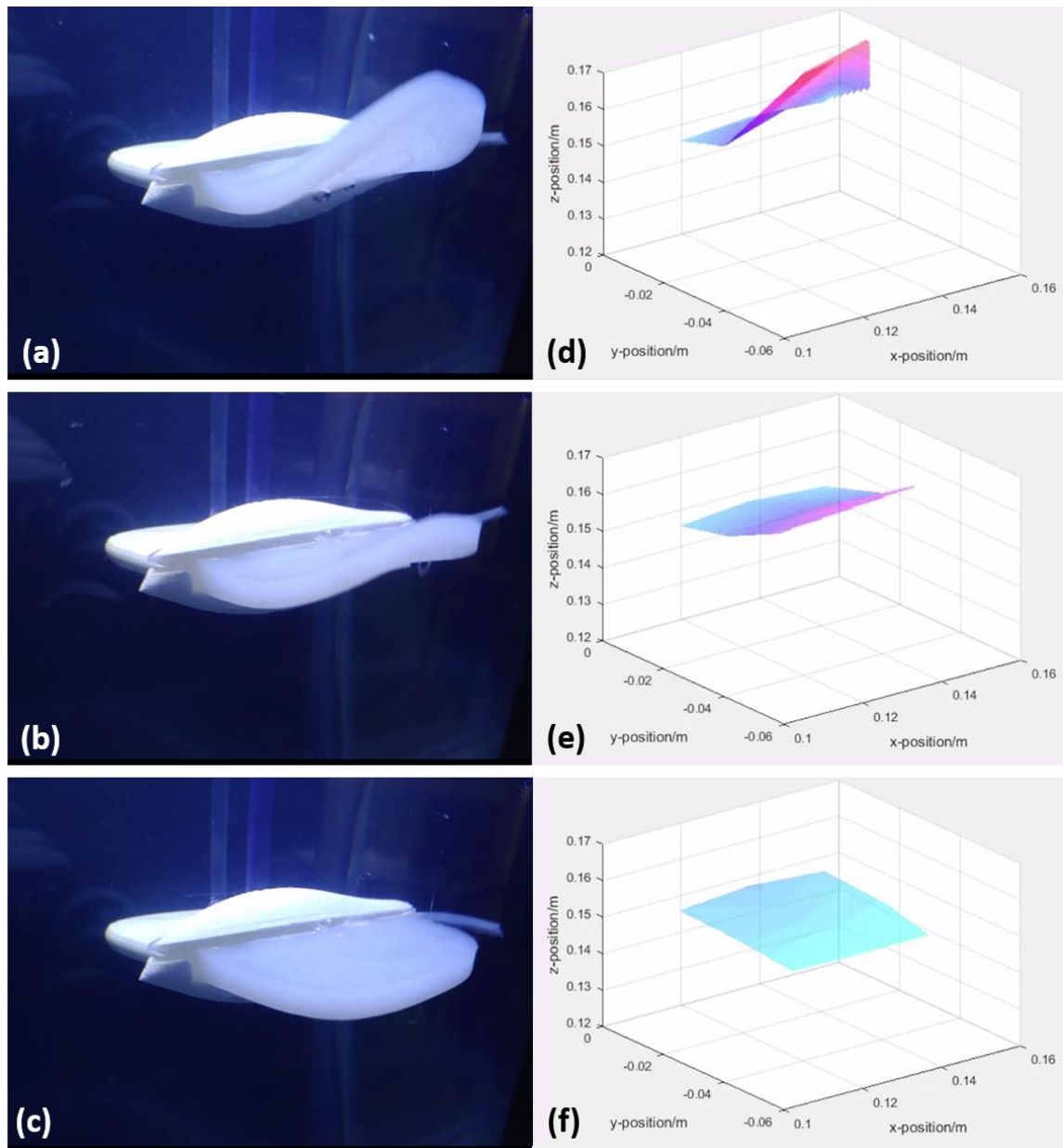
Figure 5.4.2 (a-c) Our shape sensor is embedded in a dummy stingray model. **(d-f)** The surface shape of the stingray is reconstructed under a stream of water current.

When the stingray model is under contact with other objects, i.e. experiencing external forces, it deforms and oscillates. A continuous measurement of wavelengths is shown in **Figure 5.4.3**. The vibration frequency is captured with each FBG's signal, up to the maximum update rate of the interrogator.
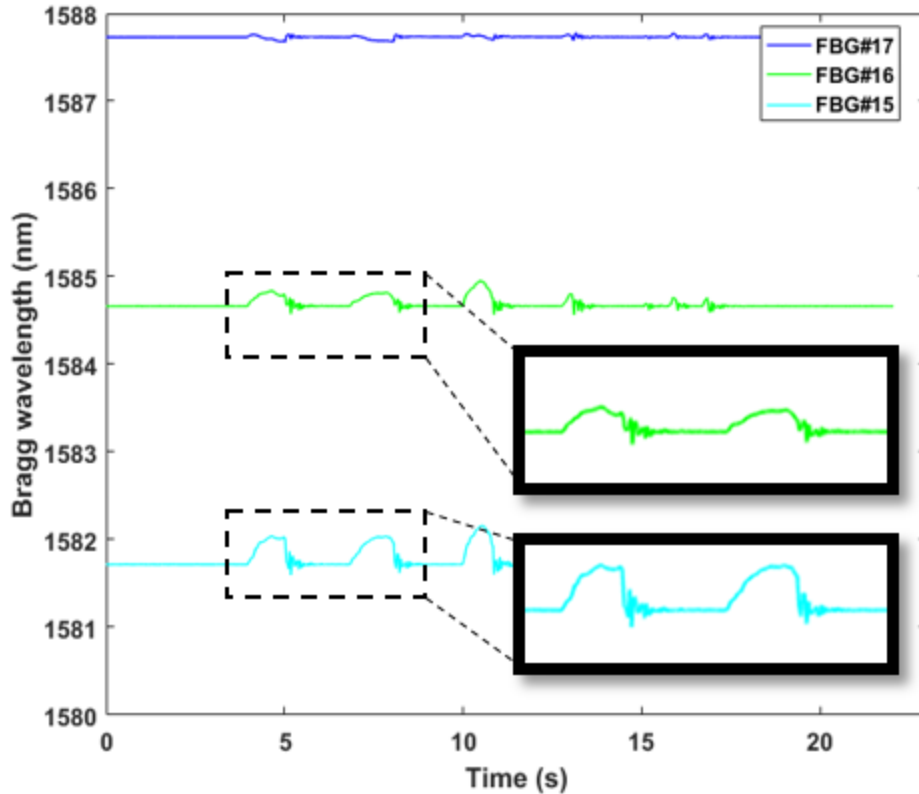
Figure 5.4.3 Vibration sensing example. An impulse force is applied on the free end of our sensor. Sensor vibrations are captured by the FBG signals.

With excellent FBG sensitivity, some external parameters (excitation frequency in this case) could be captured. However, FBG is also sensitive to pressure, thus in practice, our future development aims to combine this work with other sensors to achieving multi-modal sensing and widen the potential applications of our sensor.

One may also noticed that the current sensor has a relatively simple nominal geometry, which may limit complex types of deformation. In our future work, we aim to extend this shape sensing technology to more complicated scenarios with larger sensing coverage, such as measuring the shape of soft continuum robot or to monitor motion of a user's body as a wearable device. In **Figure 5.4.4**, an optical fiber (with sixteen FBGs embedded) is wrapped around a soft tentacle. The tentacle shape is well reconstructed based on the design framework described in this work, by mapping the FBG signals and the tentacle displacements. Since tube structure is widely used in soft and medical robotics, this example demonstrates another application of our work in practice.
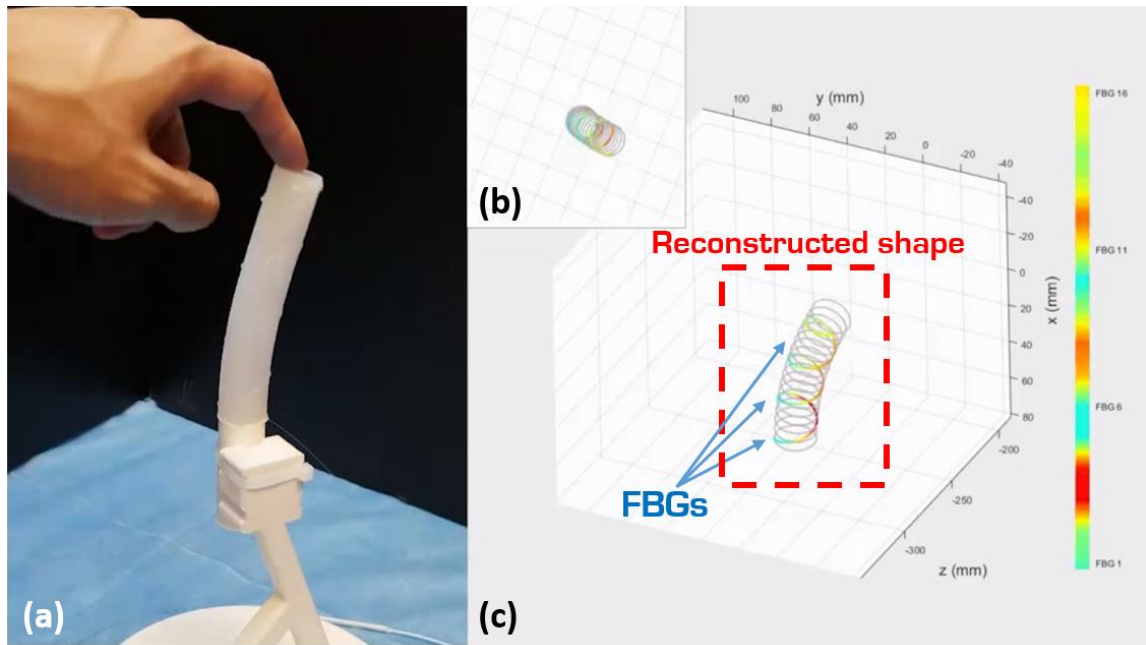
Figure 5.4.4 (a) Sixteen FBGs are embedded on a soft, silicone tentacle. A point load is applied on the top of the tentacle. **(b)** Top view of the reconstructed tentacle shape. **(c)** Reconstructed shape of the tentacle. Warm color indicates positive fiber strains while cold color indicates negative fiber strains.

6. Conclusion and Future Works

In this work, a surface shape sensor is presented with detailed design and analysis. Using fiber optics, Bragg wavelengths are measured by optical spectrum and mapped with surface information of the sensor. Finite element simulations are conducted to study, to analysis the sensor parameters and to predict the sensing responses and accuracy. A soft and flexible surface is accurately reconstructed in real-time and potential applications of the sensor are suggested. The proposed sensor has the capability to scale up to large-scale applications using multiple optical channels or phased FBG arrays with ease.

Based on the proposed sensor design framework, a sensor could be designed for usage on the surface of a soft robotic structure to detect localized deformations due to interaction with the environment. This could aid in advanced soft robotic control where discerning the location of contact on the robot body is a difficult task with current soft sensing modalities. Regarding cost, fiber-based shape sensors commonly make use of multiple-core fiber paired with OFDR-based measurement systems, which are substantially more expensive (>USD160K) and complex to implement, relative to the proposed WDM-based, single-core fiber system (<USD20K). A number of limitations still exist for the proposed sensor. Firstly, by making use of a learning-based modeling approach, inherent disadvantages arise relating to data acquisition time and reliance on accurate training data. Additionally, the proposed sensor design has a limited ability to reconstruct very complex shapes, due to the inherent effect of integrating a relatively rigid optical fiber, in combination with the small sensor size.

Further studies include an FEA-based optimization scheme to investigate optimized optical fiber layouts for complex deformations or customized shape structures. Fiber routings and configurations, sensor parameters (e.g. fiber size) and required sensor flexibly and stiffness will be considered. Combining with a larger overall sensor size, the use of polymer optical fiber may allow more complex and extreme deformation which can benefit its application as a wearable device. Also, reconstruction could be accelerated by exploring other plotting environments. Another direction would be multiple sensor integrations for multi-mode sensing and eventually enable the ability to distinguish external stimuli, at the same time, monitoring the surface shape or other desired information such as stress fields.

Bibliography

[1]   W. B. R. Baldur, "Inflatable Manipulator," *Society of Manufacturing Engineers,* 1985.

[2]   K. Suzumori, S. Iikura, and H. Tanaka, "Development of flexible microactuator and its applications to robotic mechanisms," pp. 1622-1627, 1991.

[3]   F. Connolly, P. Polygerinos, C. J. Walsh, and K. Bertoldi, "Mechanical Programming of Soft Actuators by Varying Fiber Angle," (in English), *Soft Robotics,* vol. 2, no. 1, pp. 26-32, Mar 2015.

[4]   K. Suzumori, T. Maeda, H. Watanabe, and T. Hisada, "Fiberless flexible microactuator designed by finite-element method," (in English), *Ieee-Asme Transactions on Mechatronics,* vol. 2, no. 4, pp. 281-286, Dec 1997.

[5]   J. Hiller and H. Lipson, "Automatic Design and Manufacture of Soft Robots," (in English), *Ieee Transactions on Robotics,* vol. 28, no. 2, pp. 457-466, Apr 2012.

[6]   F. Corucci, N. Cheney, H. Lipson, C. Laschi, and J. Bongard, "Material properties affect evolutions ability to exploit morphological computation in growing soft-bodied creatures," pp. 234-241, 2016.

[7]   Y. Bar-Cohen, "Electroactive Polymers as Artificial Muscles: Capabilities, Potentials and Challenges," pp. 188-196, 2000.

[8]   B. Trimmer, J. A. Lewis, R. F. Shepherd, and H. Lipson, "3D Printing Soft Materials: What Is Possible?," *Soft Robotics,* vol. 2, no. 1, pp. 3-6, 2015.

[9]   M. Heckele and W. K. Schomburg, "Review on micro molding of thermoplastic polymers," (in English), *Journal of Micromechanics and Microengineering,* vol. 14, no. 3, pp. R1-R14, Mar 2004.

[10]   D. Qin, Y. Xia, and G. M. Whitesides, "Soft lithography for micro- and nanoscale patterning," *Nat Protoc,* vol. 5, no. 3, pp. 491-502, Mar 2010.

[11]   B. Siciliano and O. Khatib, *Springer Handbook of Robotics*. Springer International Publishing, 2016.

[12]   S. Kim, C. Laschi, and B. Trimmer, "Soft robotics: a bioinspired evolution in robotics," *Trends Biotechnol,* vol. 31, no. 5, pp. 287-94, May 2013.

[13]   M. Piccigallo *et al.*, "Design of a Novel Bimanual Robotic System for Single-Port Laparoscopy," (in English), *Ieee-Asme Transactions on Mechatronics,* vol. 15, no. 6, pp. 871-878, Dec 2010.

[14]   G. Gerboni, T. Ranzani, A. Diodato, G. Ciuti, M. Cianchetti, and A. Menciassi, "Modular soft mechatronic manipulator for minimally invasive surgery (MIS): overall architecture and development of a fully integrated soft module," (in English), *Meccanica,* vol. 50, no. 11, pp. 2865-2878, Nov 2015.

[15]   J. Paek, I. Cho, and J. Kim, "Microrobotic tentacles with spiral bending capability based on shape-engineered elastomeric microtubes," *Sci Rep,* vol. 5, p. 10768, Jun 11 2015.

[16]   M. Follador, M. Cianchetti, and C. Laschi, "Development of the functional unit of a completely soft octopus-like robotic arm," (in English), *2012 4th Ieee Ras & Embs International Conference on Biomedical Robotics and Biomechatronics (Biorob),* pp. 640-645, 2012.

[17]   M. Wehner *et al.*, "An integrated design and fabrication strategy for entirely soft, autonomous robots," *Nature,* vol. 536, no. 7617, pp. 451-5, Aug 25 2016.

[18]   FESTO, "Bionic Handling Assistant," ed, 2012.

[19]   L. Hardesty, "Soft robotic fish moves like the real thing," ed: MIT News Office, 2014.

[20]   S. Seok, C. D. Onal, K. J. Cho, R. J. Wood, D. Rus, and S. Kim, "Meshworm: A Peristaltic Soft Robot With Antagonistic Nickel Titanium Coil Actuators," (in English), *Ieee-Asme Transactions on Mechatronics,* vol. 18, no. 5, pp. 1485-1497, Oct 2013.

[21]   J. Chu, "Soft autonomous robot inches along like an earthworm," ed: MIT News Office 2012.

[22]   G. Methenitis, D. Hennes, D. Izzo, and A. Visser, "Novelty Search for Soft Robotic Space Exploration," pp. 193-200, 2015.

[23]   R. W. Sproat, *Morphology and computation*. MIT press, 1992.

[24]   C. Paul, "Morphological computation - A basis for the analysis of morphology and control requirements," (in English), *Robotics and Autonomous Systems,* vol. 54, no. 8, pp. 619-630, Aug 31 2006.

[25]   C. Laschi, B. Mazzolai, and M. Cianchetti, "Soft robotics: Technologies and systems pushing the boundaries of robot abilities," *Science Robotics,* vol. 1, no. 1, p. eaah3690, 2016.

[26]   R. F. Shepherd *et al.*, "Multigait soft robot," *Proc Natl Acad Sci U S A,* vol. 108, no. 51, pp. 20400-3, Dec 20 2011.

[27]   M. T. Tolley *et al.*, "A Resilient, Untethered Soft Robot," (in English), *Soft Robotics,* vol. 1, no. 3, pp. 213-223, Sep 2014.

[28]   J. T. Muth *et al.*, "Embedded 3D Printing of Strain Sensors within Highly Stretchable Elastomers," (in English), *Advanced Materials,* vol. 26, no. 36, pp. 6307-6312, Sep 24 2014.

[29]   D. B. Camarillo, C. R. Carlson, and J. K. Salisbury, "Configuration Tracking for Continuum Manipulators With Coupled Tendon Drive," (in English), *Ieee Transactions on Robotics,* vol. 25, no. 4, pp. 798-808, Aug 2009.

[30]   F. Renda, M. Giorelli, M. Calisti, M. Cianchetti, and C. Laschi, "Dynamic Model of a Multibending Soft Robot Arm Driven by Cables," (in English), *Ieee Transactions on Robotics,* vol. 30, no. 5, pp. 1109-1122, Oct 2014.

[31]   J. Burgner-Kahrs, D. C. Rucker, and H. Choset, "Continuum Robots for Medical Applications: A Survey," (in English), *Ieee Transactions on Robotics,* vol. 31, no. 6, pp. 1261-1280, Dec 2015.

[32]   C. M. K. Puneet Kumar Singh "Continuum Arm Robotic Manipulator: A Review," *Universal Journal of Mechanical Engineering,* vol. 2, pp. 193 - 198, 2014.

[33] G. S. Chirikjian and J. W. Burdick, "A Modal Approach to Hyper-Redundant Manipulator Kinematics," (in English), *Ieee Transactions on Robotics and Automation,* vol. 10, no. 3, pp. 343-354, Jun 1994.

[34] F. Renda, M. Cianchetti, M. Giorelli, A. Arienti, and C. Laschi, "A 3D steady-state model of a tendon-driven continuum soft manipulator inspired by the octopus arm," *Bioinspir Biomim,* vol. 7, no. 2, p. 025006, Jun 2012.

[35] R. Pfeifer, M. Lungarella, and F. Iida, "The Challenges Ahead for Bio-Inspired 'Soft' Robotics," (in English), *Communications of the Acm,* vol. 55, no. 11, pp. 76-87, Nov 2012.

[36] F. Largilliere, V. Verona, E. Coevoet, M. Sanz-Lopez, J. Dequidt, and C. Duriez, "Real-time Control of Soft-Robots using Asynchronous Finite Element Modeling," (in English), *2015 Ieee International Conference on Robotics and Automation (Icra),* pp. 2550-2555, 2015.

[37] H. Shen, "The soft touch," in *Nature* vol. 530, ed: Macmillan Publishers Limited, 2016.

[38] L. P. Jentoft, Y. Tenzer, D. Vogt, J. Liu, R. J. Wood, and R. D. Howe, "Flexible, Stretchable Tactile Arrays From MEMS Barometers," (in English), *2013 16th International Conference on Advanced Robotics (Icar),* 2013.

[39] N. F. Lepora and B. Ward-Chewier, "Superresolution with an optical tactile sensor," (in English), *2015 Ieee/Rsj International Conference on Intelligent Robots and Systems (Iros),* pp. 2686-2691, 2015.

[40] C. Chorley, C. Melhuish, T. Pipe, and J. Rossiter, "Development of a Tactile Sensor Based on Biologically Inspired Edge Encoding," (in English), *Icar: 2009 14th International Conference on Advanced Robotics, Vols 1 and 2,* pp. 734-739, 2009.

[41] W. Felt, K. Y. Chin, and C. D. Remy, "Contraction Sensing With Smart Braid McKibben Muscles," (in English), *Ieee-Asme Transactions on Mechatronics,* vol. 21, no. 3, pp. 1201-1209, Jun 2016.

[42] Stretchsense. (2016). *Understanding stretch sensor sensitivity*. Available: https://stretchsense.com/articles-resources/case-studies/understanding-stretch-sensor-sensitivity/

[43] W. M. Kier and M. P. Stella, "The arrangement and function of octopus arm musculature and connective tissue," *J Morphol,* vol. 268, no. 10, pp. 831-43, Oct 2007.

[44] F. Iida and C. Laschi, "Soft Robotics: Challenges and Perspectives," *Procedia Computer Science,* vol. 7, pp. 99-102, 2011.

[45] C. Pang, C. Lee, and K.-Y. Suh, "Recent advances in flexible sensors for wearable and implantable devices," *Journal of Applied Polymer Science,* vol. 130, no. 3, pp. 1429-1441, 2013.

[46] D. H. Kim and J. A. Rogers, "Stretchable Electronics: Materials Strategies and Devices," (in English), *Advanced Materials,* vol. 20, no. 24, pp. 4887-4892, Dec 17 2008.

[47] J. Marsh, "The bionic skin that can feel a tumor," in *CNN*, ed, 2016.

[48] T. Yokota *et al.*, "Ultraflexible organic photonic skin," *Sci Adv,* vol. 2, no. 4, p. e1501856, Apr 2016.

[49]   S. Patel, H. Park, P. Bonato, L. Chan, and M. Rodgers, "A review of wearable sensors and systems with application in rehabilitation," *J Neuroeng Rehabil,* vol. 9, p. 21, Apr 20 2012.

[50]   R. Dias and J. M. da Silva, "A Flexible Wearable Sensor Network for Bio-signals and Human Activity Monitoring," (in English), *2014 11th International Conference on Wearable and Implantable Body Sensor Networks Workshops (Bsn Workshops),* pp. 17-22, 2014.

[51]   T. Someya and T. Sekitani, "Bionic skins using flexible organic devices," pp. 68-71, 2014.

[52]   L. Xu *et al.*, "3D multifunctional integumentary membranes for spatiotemporal cardiac measurements and stimulation across the entire epicardium," *Nat Commun,* vol. 5, p. 3329, Feb 25 2014.

[53]   T. P. Huynh and H. Haick, "Self-Healing, Fully Functional, and Multiparametric Flexible Sensing Platform," *Adv Mater,* vol. 28, no. 1, pp. 138-43, Jan 06 2016.

[54]   B. S. Homberg, R. K. Katzschmann, M. R. Dogar, and D. Rus, "Haptic identification of objects using a modular soft robotic gripper," pp. 1698-1705, 2015.

[55]   J. Hughes, U. Culha, F. Giardina, F. Guenther, A. Rosendo, and F. Iida, "Soft Manipulators and Grippers: A Review," (in English), *Frontiers in Robotics and AI,* vol. 3, Nov 16 2016.

[56]   J.-B. Chossat, Y.-L. Park, R. J. Wood, and V. Duchaine, "A Soft Strain Sensor Based on Ionic and Metal Liquids," *IEEE Sensors Journal,* vol. 13, no. 9, pp. 3405-3414, 2013.

[57]   P. Yong-Lae, C. Bor-Rong, and R. J. Wood, "Design and Fabrication of Soft Artificial Skin Using Embedded Microchannels and Liquid Conductors," *IEEE Sensors Journal,* vol. 12, no. 8, pp. 2711-2718, 2012.

[58]   D. M. Vogt, Y.-L. Park, and R. J. Wood, "Design and Characterization of a Soft Multi-Axis Force Sensor Using Embedded Microfluidic Channels," *IEEE Sensors Journal,* vol. 13, no. 10, pp. 4056-4064, 2013.

[59]   T. Someya, T. Sekitani, S. Iba, Y. Kato, H. Kawaguchi, and T. Sakurai, "A large-area, flexible pressure sensor matrix with organic field-effect transistors for artificial skin applications," *Proc Natl Acad Sci U S A,* vol. 101, no. 27, pp. 9966-70, Jul 6 2004.

[60]   S. C. Mannsfeld *et al.*, "Highly sensitive flexible pressure sensors with microstructured rubber dielectric layers," *Nat Mater,* vol. 9, no. 10, pp. 859-64, Oct 2010.

[61]   G. Schwartz *et al.*, "Flexible polymer transistors with high pressure sensitivity for application in electronic skin and health monitoring," *Nat Commun,* vol. 4, p. 1859, 2013.

[62]   Y. Noguchi, T. Sekitani, and T. Someya, "Organic-transistor-based flexible pressure sensors using ink-jet-printed electrodes and gate dielectric layers," *Applied Physics Letters,* vol. 89, no. 25, p. 253507, 2006.

[63]   D. J. Lipomi *et al.*, "Skin-like pressure and strain sensors based on transparent elastic films of carbon nanotubes," *Nat Nanotechnol,* vol. 6, no. 12, pp. 788-92, Oct 23 2011.

[64]   S. Park, M. Vosguerichian, and Z. Bao, "A review of fabrication and applications of carbon nanotube film-based flexible electronics," *Nanoscale,* vol. 5, no. 5, pp. 1727-52, Mar 07 2013.

[65]   J. Zhou *et al.*, "Flexible piezotronic strain sensor," *Nano Lett,* vol. 8, no. 9, pp. 3035-40, Sep 2008.

[66] Q. Liao, M. Mohr, X. Zhang, Z. Zhang, Y. Zhang, and H. J. Fecht, "Carbon fiber-ZnO nanowire hybrid structures for flexible and adaptable strain sensors," *Nanoscale,* vol. 5, no. 24, pp. 12350-5, Dec 21 2013.

[67] X. Liu, M. Mwangi, X. Li, M. O'Brien, and G. M. Whitesides, "Paper-based piezoresistive MEMS sensors," *Lab Chip,* vol. 11, no. 13, pp. 2189-96, Jul 07 2011.

[68] H. Gullapalli *et al.*, "Flexible piezoelectric ZnO-paper nanocomposite strain sensor," *Small,* vol. 6, no. 15, pp. 1641-6, Aug 02 2010.

[69] A. Frutiger *et al.*, "Sensors: Capacitive Soft Strain Sensors via Multicore-Shell Fiber Printing (Adv. Mater. 15/2015)," *Advanced Materials,* vol. 27, no. 15, pp. 2548-2548, 2015.

[70] L. Cai *et al.*, "Super-stretchable, transparent carbon nanotube-based capacitive strain sensors for human motion detection," *Sci Rep,* vol. 3, p. 3048, Oct 25 2013.

[71] G. T. Pham, Y.-B. Park, Z. Liang, C. Zhang, and B. Wang, "Processing and modeling of conductive thermoplastic/carbon nanotube films for strain sensing," *Composites Part B: Engineering,* vol. 39, no. 1, pp. 209-216, 2008.

[72] C. Mattmann, F. Clemens, and G. Troster, "Sensor for Measuring Strain in Textile," *Sensors (Basel),* vol. 8, no. 6, pp. 3719-3732, Jun 03 2008.

[73] W. Luheng, D. Tianhuai, and W. Peng, "Influence of carbon black concentration on piezoresistivity for carbon-black-filled silicone rubber composite," *Carbon,* vol. 47, no. 14, pp. 3151-3157, 2009.

[74] B. Winstone, G. Griffiths, T. Pipe, C. Melhuish, and J. Rossiter, "TACTIP - Tactile Fingertip Device, Texture Analysis through Optical Tracking of Skin Features," vol. 8064, pp. 323-334, 2013.

[75] P. Kang, M. C. Wang, P. M. Knapp, and S. Nam, "Crumpled Graphene Photodetector with Enhanced, Strain-Tunable, and Wavelength-Selective Photoresponsivity," *Adv Mater,* vol. 28, no. 23, pp. 4639-45, Jun 2016.

[76] S. C. Ryu and P. E. Dupont, "FBG-based Shape Sensing Tubes for Continuum Robots," (in English), *2014 Ieee International Conference on Robotics and Automation (Icra),* pp. 3531-3537, 2014.

[77] J. P. Moore and M. D. Rogge, "Shape sensing using multi-core fiber optic cable and parametric curve solutions," (in English), *Optics Express,* vol. 20, no. 3, pp. 2967-2973, Jan 30 2012.

[78] J. M. Croom, D. C. Rucker, J. M. Romano, and R. J. Webster, "Visual Sensing of Continuum Robot Shape Using Self-Organizing Maps," (in English), *2010 Ieee International Conference on Robotics and Automation (Icra),* pp. 4591-4596, 2010.

[79] C. Mattmann, O. Amft, H. Harms, G. Troster, and F. Clemens, "Recognizing Upper Body Postures using Textile Strain Sensors," pp. 1-8, 2007.

[80] C. Cochrane, V. Koncar, M. Lewandowski, and C. Dufour, "Design and development of a flexible strain sensor for textile structures based on a conductive polymer composite," (in English), *Sensors,* vol. 7, no. 4, pp. 473-492, Apr 2007.

[81] P. Calvert, D. Duggal, P. Patra, A. Agrawal, and A. Sawhney, "Conducting Polymer and Conducting Composite Strain Sensors on Textiles," *Molecular Crystals and Liquid Crystals,* vol. 484, no. 1, pp. 291/[657]-302/[668], 2010.

[82] T. Yamada *et al.*, "A stretchable carbon nanotube strain sensor for human-motion detection," *Nat Nanotechnol,* vol. 6, no. 5, pp. 296-301, May 2011.

[83] C. Dagdeviren *et al.*, "Recent progress in flexible and stretchable piezoelectric devices for mechanical energy harvesting, sensing and actuation," *Extreme Mechanics Letters,* vol. 9, pp. 269-281, 2016.

[84] S. M. Won *et al.*, "Piezoresistive Strain Sensors and Multiplexed Arrays Using Assemblies of Single-Crystalline Silicon Nanoribbons on Plastic Substrates," *IEEE Transactions on Electron Devices,* vol. 58, no. 11, pp. 4074-4078, 2011.

[85] U.-H. Shin, D.-W. Jeong, S.-M. Park, S.-H. Kim, H. W. Lee, and J.-M. Kim, "Highly stretchable conductors and piezocapacitive strain gauges based on simple contact-transfer patterning of carbon nanotube forests," *Carbon,* vol. 80, pp. 396-404, 2014.

[86] R. Zeiser, T. Fellner, and J. Wilde, "Capacitive strain gauges on flexible polymer substrates for wireless, intelligent systems," *Journal of Sensors and Sensor Systems,* vol. 3, no. 1, pp. 77-86, 2014.

[87] F. Xu and Y. Zhu, "Highly conductive and stretchable silver nanowire conductors," *Adv Mater,* vol. 24, no. 37, pp. 5117-22, Sep 25 2012.

[88] F. Jülich, L. Aulbach, A. Wilfert, P. Kratzer, R. Kuttler, and J. Roths, "Gauge factors of fibre Bragg grating strain sensors in different types of optical fibres," *Measurement Science and Technology,* vol. 24, no. 9, p. 094007, 2013.

[89] C. Davis, S. Tejedor, I. Grabovac, J. Kopczyk, and T. Nuyens, "High-strain Fiber Bragg Gratings for Structural Fatigue Testing of Military Aircraft," *Photonic Sensors,* vol. 2, no. 3, pp. 215-224, 2012.

[90] L. I. Incorporated. (2016). *3D Shape & Positioning Sensing*. Available: https://lunainc.com/growth-area/technology-development/optical-systems/

[91] Polytec. (2015). *Shape Sensing*. Available: http://www.polytec.com/fileadmin/user_uploads/Products/Faseroptische_Sensorik/documents/PH_TFT_APPNOTE_-_Shape_Sensing.pdf

[92] Fraunhofer. (2013). *3D fiber optical shape and motion sensing*. Available: https://www.hhi.fraunhofer.de/fileadmin/PDF/FS/FiberLab/15-06-01_3D-Shape-Sensing.pdf

[93] L. I. Incorporated, "Luna Works with Office of Naval Research in ''DADS'' Sensor Array Enhancement," ed, 2008.

[94] T. inno. (2013). *Innovative Cable-Like-Shape-Sensor* Available: http://www.tst-inno.de/en/SAC.html

[95] T. Rice, "NASA-Inspired Shape-Sensing Fibers Enable Minimally Invasive Surgery ", ed: Tech Briefs Media Group, 2008.

[96]   R. G. Duncan *et al.*, "Characterization of a fiber-optic shape and position sensor," *Proc. of SPIE Vol. 6167 616704, (2006),* vol. 6167, p. 616704, 2006.

[97]   K. K. Lee, A. Mariampillai, M. Haque, B. A. Standish, V. X. Yang, and P. R. Herman, "Temperature-compensated fiber-optic 3D shape sensor based on femtosecond laser direct-written Bragg grating waveguides," *Opt Express,* vol. 21, no. 20, pp. 24076-86, Oct 7 2013.

[98]   P. V. Y. Alvarado, S. Chin, W. Larson, A. Mazumdar, and K. Youcef-Toumi, "A Soft Body Under-actuated Approach to Multi Degree of Freedom Biomimetic Robots: A stingray example.," (in English), *2010 3rd Ieee Ras and Embs International Conference on Biomedical Robotics and Biomechatronics,* pp. 473-478, 2010.

[99]   P. Mittendorfer and G. Cheng, "3D Surface Reconstruction for Robotic Body Parts with Artificial Skins," (in English), *2012 Ieee/Rsj International Conference on Intelligent Robots and Systems (Iros),* pp. 4505-4510, 2012.

[100]   N. Sprynski, B. Lacolle, and L. Biard, "Motion Capture of an Animated Surface via Sensors' Ribbons," in *PECCS 2011 - 1st International Conference on Pervasive and Embedded Computing and Communication Systems*, Vilamoura, Algarve, Portugal, 2011, pp. 421-426: SciTePress.

[101]   N. Saguin-Sprynski, L. Jouanet, B. Lacolle, and L. Biard, "Surfaces Reconstruction Via Inertial Sensors for Monitoring," in *EWSHM - 7th European Workshop on Structural Health Monitoring*, Nantes, France, 2014, https://hal.inria.fr/hal-01020418/document,https://hal.inria.fr/hal-01020418/file/0119.pdf.

[102]   M. Huard, N. Sprynski, N. Szafran, and L. Biard, "Reconstruction of quasi developable surfaces from ribbon curves," (in English), *Numerical Algorithms,* vol. 63, no. 3, pp. 483-506, Jul 2013.

[103]   C. Rendl *et al.*, "FlexSense: a transparent self-sensing deformable surface," pp. 129-138, 2014.

[104]   A. Hermanis, R. Cacurs, and M. Greitans, "Acceleration and Magnetic Sensor Network for Shape Sensing," (in English), *Ieee Sensors Journal,* vol. 16, no. 5, pp. 1271-1280, Mar 1 2016.

[105]   S. Follmer, M. Johnson, E. Adelson, and H. Ishii, "deForm: An Interactive Malleable Surface For Capturing 2.5D Arbitrary Objects, Tools and Touch," p. 527, 2011.

[106]   S. Izadi *et al.*, "KinectFusion: Real-time 3D Reconstruction and Interaction Using a Moving Depth Camera," p. 559, 2011.

[107]   Y. Cui, S. Schuon, D. Chan, S. Thrun, and C. Theobalt, "3D Shape Scanning with a Time-of-Flight Camera," (in English), *2010 Ieee Conference on Computer Vision and Pattern Recognition (Cvpr),* pp. 1173-1180, 2010.

[108]   K. O. Hill, Y. Fujii, D. C. Johnson, and B. S. Kawasaki, "Photosensitivity in Optical Fiber Waveguides - Application to Reflection Filter Fabrication," (in English), *Applied Physics Letters,* vol. 32, no. 10, pp. 647-649, 1978.

[109]   "Fundamentals of FBG Optical Sensing (White paper)," National Instruments2011.

[110] M. M, R. C. S. B. Allil, B. A, and F. V. B. de Nazar, "A Guide to Fiber Bragg Grating Sensors," 2013.

[111] B. A. Childers *et al.*, "Use of 3000 Bragg grating strain sensors distributed on four 8-m optical fibers during static load tests of a composite structure," 2001, vol. 4332, pp. 133-142.

[112] C. H. Yeh, C. W. Chow, P. C. Wu, and F. G. Tseng, "A simple fiber Bragg grating-based sensor network architecture with self-protecting and monitoring functions," *Sensors (Basel),* vol. 11, no. 2, pp. 1375-82, 2011.

[113] J. Bos, J. Klein, M. Froggatt, E. Sanborn, and D. Gifford, "Fiber optic strain, temperature and shape sensing via OFDR for ground, air and space applications," (in English), *Nanophotonics and Macrophotonics for Space Environments Vii,* vol. 8876, 2013.

[114] M. A. Davis, A. D. Kersey, J. Sirkis, and E. J. Friebele, "Shape and vibration mode sensing using a fiber optic Bragg grating array," (in English), *Smart Materials & Structures,* vol. 5, no. 6, pp. 759-765, Dec 1996.

[115] (2008). *A Fiber Bragg Grating structure, with refractive index profile and spectral response*. Available: https://en.wikipedia.org/wiki/Fiber_Bragg_grating#/media/File:Fiber_Bragg_Grating-en.svg

[116] V. a. A. G. S. Dewra, "Fabrication and Applications of Fiber Bragg Grating-A Review," *Advanced Engineering Technology and Application,* 2015.

[117] A. Airoldi *et al.*, "Load Monitoring by Means of Optical Fibres and Strain Gages," pp. 433-469, 2016.

[118] P. Saccomandi *et al.*, "Feedforward Neural Network for Force Coding of an MRI-Compatible Tactile Sensor Array Based on Fiber Bragg Grating," (in English), *Journal of Sensors,* 2015.

[119] M. A. Kamisi, Cosetti, G. R. C., Muller, M., & Fabris, J. L., "Fiber Bragg grating sensors probed by artificial intelligence to detect and localize impacts on structures," *Journal of Microwaves, Optoelectronics and Electromagnetic Applications (JMOe) 14,* pp. 25-34, 2015.

[120] M. Y. E.-B. Taymour A. Hamdalla, Moaaz A. Moussa, "Fiber Bragg grating as temperature sensor using neural network modeling," *International Journal of Scientific and Engineering Research,* vol. Volume 3, no. Issue 12, 2012.

[121] A. A. Moghadas and M. Shadaram, "Fiber Bragg Grating sensor for fault detection in radial and network transmission lines," *Sensors (Basel),* vol. 10, no. 10, pp. 9407-23, 2010.

[122] P. Luo, D. S. Zhang, L. X. Wang, and D. S. Jiang, "Structural Damage Detection Based on a Fiber Bragg Grating Sensing Array and a Back Propagation Neural Network: An Experimental Study," (in English), *Structural Health Monitoring-an International Journal,* vol. 9, no. 1, pp. 5-11, Jan 2010.

[123] A. F. da Silva, A. F. Goncalves, P. M. Mendes, and J. H. Correia, "FBG Sensing Glove for Monitoring Hand Posture," *IEEE Sensors Journal,* vol. 11, no. 10, pp. 2442-2448, 2011.

[124] H. Garcia-Miquel, D. Barrera, R. Amat, G. V. Kurlyandskaya, and S. Sales, "Magnetic actuator based on giant magnetostrictive material Terfenol-D with strain and temperature monitoring using FBG optical sensor," (in English), *Measurement,* vol. 80, pp. 201-206, Feb 2016.

[125] A. Castro-Caicedo, P. Torres, and R. Lain, "Packaging and testing of fiber Bragg gratings for use as strain sensor in rock specimens," (in English), *8th Iberoamerican Optics Meeting and 11th Latin American Meeting on Optics, Lasers, and Applications,* vol. 8785, 2013.

[126] H. Y. Ling, K. T. Lau, L. Cheng, and W. Jin, "Viability of using an embedded FBG sensor in a composite structure for dynamic strain measurement," (in English), *Measurement,* vol. 39, no. 4, pp. 328-334, May 2006.

[127] A. A. Kazemi, E. A. Mendoza, C. S. Baldwin, C. Kempen, A. Panahi, and C. Lopatin, "Miniature fiber Bragg grating sensor interrogator (FBG-Transceiver) system for use in aerospace and automotive health monitoring systems," vol. 6758, p. 67580B, 2007.

[128] E. Mikołajewska, M. Macko, Ł. Ziarnecki, S. Stańczak, P. Kawalec, and D. Mikołajewski, "3D printing technologies in rehabilitation engineering," 2014.

[129] C. L. Ventola, "Medical applications for 3D printing: current and projected uses," *Pharmacy and Therapeutics,* vol. 39, no. 10, p. 704, 2014.

[130] K. Reda *et al.*, "Visualizing large, heterogeneous data in hybrid-reality environments," *IEEE Computer Graphics and Applications,* vol. 33, no. 4, pp. 38-48, 2013.

[131] X. Sang *et al.*, "Demonstration of a large-size real-time full-color three-dimensional display," *Optics letters,* vol. 34, no. 24, pp. 3803-3805, 2009.

[132] H. Park, H. Lee, H. Adeli, and I. Lee, "A new approach for health monitoring of structures: terrestrial laser scanning," *Computer-Aided Civil and Infrastructure Engineering,* vol. 22, no. 1, pp. 19-30, 2007.

[133] R. Li and E. H. Adelson, "Sensing and recognizing surface textures using a gelsight sensor," in *Computer Vision and Pattern Recognition (CVPR), 2013 IEEE Conference on*, 2013, pp. 1241-1247: IEEE.

[134] G. Foss, "Using modal test results to develop strain to displacement transformations," 1995.

[135] P. Bogert, E. Haugse, and R. Gehrki, "Structural shape identification from experimental strains using a modal transformation technique," in *44th AIAA/ASME/ASCE/AHS/ASC Structures, Structural Dynamics, and Materials Conference*, 2003, p. 1626.

[136] L. Piegl and W. Tiller, "The NURBS Book," 1995.

[137] H. Zhang, X. Zhu, Z. Gao, K. Liu, and F. Jiang, "Fiber Bragg grating plate structure shape reconstruction algorithm based on orthogonal curve net," *Journal of Intelligent Material Systems and Structures,* vol. 27, no. 17, pp. 2416-2425, 2016.

[138] A. Tessler and J. L. Spangler, "A variational principle for reconstruction of elastic deformations in shear deformable plates and shells," 2003.

[139] M. Gherlone, P. Cerracchio, M. Mattone, M. Di Sciuva, and A. Tessler, "Shape sensing of 3D frame structures using an inverse Finite Element Method," (in English), *International Journal of Solids and Structures,* vol. 49, no. 22, pp. 3100-3112, Nov 1 2012.

[140] J. S. A. Tessler, M.Gherlone, M. Mattone, and M. Di Sciuva, "Deformed Shape and Stress Reconstruction in Plate and Shell Structures Undergoing Large Displacements: Application of Inverse Finite Element Method using Fiber-Bragg-Grating Strains," 2012.

[141] NASA, "iFEM: Inverse Finite Element Method," 2013.

[142] A. Kefal, E. Oterkus, A. Tessler, and J. L. Spangler, "A quadrilateral inverse-shell element with drilling degrees of freedom for shape sensing and structural health monitoring," *Engineering Science and Technology, an International Journal,* vol. 19, no. 3, pp. 1299-1313, 2016.

[143] M. Gherlone, P. Cerracchio, M. Mattone, M. Di Sciuva, and A. Tessler, "An inverse finite element method for beam shape sensing: theoretical framework and experimental validation," *Smart Materials and Structures,* vol. 23, no. 4, p. 045027, 2014.

[144] A. Kefal and M. Yildiz, "Modeling of Sensor Placement Strategy for Shape Sensing and Structural Health Monitoring of a Wing-Shaped Sandwich Panel Using Inverse Finite Element Method," *Sensors (Basel),* vol. 17, no. 12, Nov 30 2017.

[145] C. Laschi, B. Mazzolai, V. Mattoli, M. Cianchetti, and P. Dario, "Design of a biomimetic robotic octopus arm," *Bioinspir Biomim,* vol. 4, no. 1, p. 015006, Mar 2009.

[146] C. Laschi, M. Cianchetti, B. Mazzolai, L. Margheri, M. Follador, and P. Dario, "Soft Robot Arm Inspired by the Octopus," *Advanced Robotics,* vol. 26, no. 7, pp. 709-727, 2012.

[147] Y. Yekutieli, R. Sagiv-Zohar, R. Aharonov, Y. Engel, B. Hochner, and T. Flash, "Dynamic model of the octopus arm. I. Biomechanics of the octopus reaching movement," *J Neurophysiol,* vol. 94, no. 2, pp. 1443-58, Aug 2005.

[148] G. J. Stephens, B. Johnson-Kerner, W. Bialek, and W. S. Ryu, "Dimensionality and dynamics in the behavior of C. elegans," *PLoS Comput Biol,* vol. 4, no. 4, p. e1000028, Apr 25 2008.

[149] R. Kashyap, *Fiber Bragg Gratings*. 2010.

[150] P. Moseley, J. M. Florez, H. A. Sonar, G. Agarwal, W. Curtin, and J. Paik, "Modeling, Design, and Development of Soft Pneumatic Actuators with Finite Element Method " *Advanced Engineering Materials,* vol. 18, no. 6, pp. 978-988, 2016.

[151] "Inverse Methods for Load Identification Augmented By Optimal Sensor Placement and Model Order Reduction."

[152] U. Culha, U. Wani, S. G. Nurzaman, F. Clemens, and F. Iida, "Motion Pattern Discrimination for Soft Robots with Morphologically Flexible Sensors," (in English), *2014 Ieee/Rsj International Conference on Intelligent Robots and Systems (Iros 2014),* pp. 567-572, 2014.

[153] M. Y. Cheng, C. M. Tsao, Y. Z. Lai, and Y. J. Yang, "The development of a highly twistable tactile sensing array with stretchable helical electrodes," (in English), *Sensors and Actuators a-Physical,* vol. 166, no. 2, pp. 226-233, Apr 2011.

[154] Kenry, J. C. Yeo, and C. T. Lim, "Emerging flexible and wearable physical sensing platforms for healthcare and biomedical applications," (in English), *Microsystems & Nanoengineering,* vol. 2, Sep 26 2016.

[155] N. Mitsugi, H. Nagata, M. Shiroishi, N. Miyamoto, and R. Kaizu, "Optical Fiber Breaks Due to Buckling: Problems in Device Packaging," *Optical Fiber Technology,* vol. 1, no. 3, pp. 278-282, 1995.

[156] H. Hocheng and C. M. Chen, "Design, fabrication and failure analysis of stretchable electrical routings," *Sensors (Basel),* vol. 14, no. 7, pp. 11855-77, Jul 4 2014.

[157] M. Kreuzer, "Strain measurement with fiber Bragg grating sensors," *HBM, Darmstadt, S2338-1.0 e,* 2006.